PROTON INDUCED FRAGMENTATION OF GOLD NUCLEI AT INCIDENT ENERGY OF 2.5 GeV

Im Fachbereich Naturwissenschaften-Physik
der Bergischen Universität Wuppertal
genehmigte Dissertation
zur Erlangung des akademischen Grades Dr. rer. nat.

vorgelegt von

Virginie Bollini

aus Porto-Vecchio

- November 2004 -

1. Gutachter: PD. Dr. F. Goldenbaum
2. Gutachter: Prof. Dr. K.H. Kampert
Tag der mündlichen Prüfung: 17. Feb. 2005

Abstract

Abstract

This thesis is concerning the presentation of the PISA experiment which the subject is the proton induced reaction on gold at proton energy 2.5 GeV. Energy spectra have been measured at 3 different angles: 35, 50 and 100^{o} for Light Charged Particles (LCP, Z=2) and Intermediate Mass Fragments (IMFs, $3 \leq Z \leq 8$) produced in the mentioned reaction. The PISA experimental setup and the particle identification method using silicon detectors are described. Emphasis has been put on measuring a broad kinetic energy range of emitted particles as well as on isotope separation. Different theoretical approaches (INCL4.2+GEM model, moving source fit and Fisher's droplet model) are used and are shown in order to try to describe the reaction mechanism responsible for the emission of spallation products. At the end, a discussion of the results shows that production cross sections are a great importance for models and code improvement. As for example it has been shown that generally the emission from equilibrium processes can be well described by the INCL4.2+GEM model. However currently there are no models on the market which are capable of describing the high energy tails of kinetic energy distributions associated in particular with pre-equilibrium processes. Therefore a reliable and comprehensive experimental data base for p-induced reactions should be extended by further experimental investigations in the future in order to allow benchmarking of newly developed models.

Contents

1 Introduction **1**

2 Overview of p+Au investigations **5**

3 Theoretical models of fragmentation **17**
3.1 Intranuclear Cascade Model 18
3.2 Generalized Evaporation Model 21
3.3 Fisher's droplet model of fragmentation 24
3.4 Moving source model 27

4 Experiment **29**
4.1 Properties of the internal beam experiment 29
4.2 Scattering chamber and detectors 32
4.2.1 Choice and properties of the target 35
4.2.2 Silicon detector telescopes 37
4.2.3 Cooled silicon telescopes 42
4.2.4 Bragg Curve Detector 43
4.2.5 Multichannel-plate detectors 45
4.3 Construction of detectors 47
4.4 Data Acquisition 47

5 Analysis of experimental data **53**
5.1 Calibration of the ΔE-E spectra 53
5.2 Solid angle of detectors 55
5.3 Particle Identification Method 56

6 Experimental results **59**

7 Model analysis **67**
7.1 Comparison between model predictions and experiment 67
7.2 Moving source fits 72
7.3 Fisher's droplet model 93

8 Summary and discussion **99**

A Interaction of particles with matter and methods of particle identification **103**
A.1 Bethe-Bloch formula 103
A.2 ΔE-E techniques for charged particle identification 104

Chapter 1

Introduction

The interaction of high energy protons with atomic nuclei has been studied since over fifty years. Such a continuous interest in this subject is caused by many reasons. First of all, proton induced nuclear reactions are very interesting themselves because they involve both fundamental problems, i.e. nucleon - nucleon interaction and properties of the nuclei in various conditions of excitation. Furthermore, modification of the proton energy and/or target nucleus leads to a very rich spectrum of phenomena which have to be understood and described theoretically. Emission of light particles (with atomic number $Z \leq 2$) dominates usually the yield of reaction products for light target nuclei, while for heavy targets also spallation and fission residua give significant contribution. The intermediate mass fragments (***IMF's***), i.e. particles heavier than helium isotopes but lighter than fission residua, appear as reaction products for all target nuclei.

The next argument for investigation of proton – nucleus collisions is belief that the understanding of the mechanism of proton – nucleus collisions is condition *sine qua non* for understanding of much more complicated mechanism of heavy ions collisions. It is expected, that the proton collisions with atomic nuclei do not cause significant compression or deformation of nuclei therefore description of proton induced reactions should be less complex than reactions induced by heavy ion collisions.

Furthermore, the study of proton – nucleus collisions is a source of experimental data which are extremely important for scientific and technological applications. There are multiple questions addressed in the context of e.g., design of accelerator driven systems of energy amplification and nuclear waste utilization, radiological safety of the nuclear plants, planning and design of neutron spallation sources, medical applications, astrophysical studies, etc. which cannot be answered without knowledge of the cross sections for proton – nucleus collisions. Moreover, these data must cover practically full list of the atomic nuclei studied in very broad range of proton energies – from MeV to tens of GeV. It is, of course, almost impossible to measure all necessary data thus one must rely on the theoretical models or parametrizations which are able to interpolate and extrapolate the experimental information to the targets or energies not available experimentally. To validate and to test theoretical models for various ranges of target mass and proton beam energy the set of reliable data consisted of inclusive and exclusive observables should be available.

The present situation, both experimentally as well as theoretically is rather puzzling. In spite of long history of investigations of proton – nucleus reactions neither the predictive power of available theoretical models reached demanded accuracy nor the experimental data basis is rich enough to serve as the benchmarks which can put very restrictive demands and constraints to the theoretical description. The theoretical models are not able to reproduce the full amount of the observed phenomena and frequently they allow only for ambiguous interpretation of the observed facts. To avoid such a situation it is necessary to use the set of experimental data which cover not

only the inclusive data as total production cross sections for various ejectiles but also exclusive data as differential cross sections for different proton beam energies, covering angular and energy dependence of these data as well as mass and charge distributions of the reaction products. These data should be available at least for several target nuclei representing the light nuclei, medium mass nuclei as well as the heavy nuclei. The gold target representing the latter nuclei is the one which is most frequently studied experimentally. Thus it is a good chance to complete the existing data by some additional which are still necessary to obtain a consistent set of benchmark data for the representative of heavy nuclei. In the next chapter an overview of the investigations performed up to now for proton – Au nucleus collisions is made and arguments for choosing the 2.5 GeV energy of the proton beam are presented.

The reactions observed for proton – nucleus collisions may be divided into three classes: **(i)** ***fragmentation*** which consists in emission of several light particles ($Z \leq 2$) and IMF's, **(ii)** ***fission*** – proceeding via such strongly deformed configuration that a neck between two fragments of the compound nucleus is formed and the binary decay of the nucleus appears (accompanied normally by emission of several nucleons), and **(iii)** ***spallation*** process in which only one large remnant remains after emission of several light particles. Of course this classification has schematic character because only for very light nuclei it is possible to observe several light particles and one or two intermediate mass fragments without heavy reaction residues, i.e. the typical fragmentation. If heavy nucleus emits similar number of light and intermediate mass particles as mentioned above light nucleus, then necessarily one heavy reaction residue remains. Such a reaction is called ***deep spallation*** process. It is worthy to point out that in the inclusive experiment, in which only IMF's are detected, it may be difficult to distinguish deep spallation from fragmentation. Therefore, fragmentation is frequently used as more general term which is avoided only in the case when the single heavy remnant of the deep spallation is detected. The disassembly of nuclei may proceed also into *several* IMF's (without one, distinctly larger fragment) and then it is called ***multifragmentation***. The above distinction of various classes of reactions may be done unambiguously for heavy nuclei in exclusive experiments. However, in the case of very light target nuclei it is difficult to decide whether the process has character of fragmentation or spallation.

This classification takes into consideration the observed characteristics of the ejectiles but, of course, it is closely related to the reaction mechanism of proton – nucleus collisions. It is generally assumed that at high proton energies the reaction proceeds in two stages: (i) The incoming fast proton collides with single nucleon or with several nucleons transferring momentum and energy to the nucleus and leaves the nucleus – accompanied by several light or intermediate mass particles. (ii) The residual nucleus achieves (at least partly) the statistical equilibrium in which energy is shared among all nucleons and due to unavoidable fluctuations of the energy distribution some nucleons or their groups are emitted from the excited nucleus. This picture can, in principle, be adequate to all observed processes, i.e. fragmentation, spallation, and fission. For example, the fast light particles and intermediate mass fragments observed in the fragmentation process may appear from the first stage of the reaction, whereas slower particles can be evaporated from equilibrated residual nucleus. Similar scheme corresponds to spallation process with only one difference, i.e. deexcitation of the residual nucleus of the first step of reaction should proceed in such a way as to leave one big (comparable with target nucleus) residuum. The same can be true for fission process which starts from the compound nucleus of the first reaction stage excited sufficiently high to cause large deformation and to pass the fission barrier resulting in emission of two comparable large fragments.

There appear, however, many questions concerning details of the mechanism of the both reaction stages. Let us discuss some of them concerning the first step of the reaction. The velocity of the high energy incident proton is large compared to velocity of the Fermi motion of nucleons in

the nucleus. Thus the first step of the proton-nucleus reaction can be regarded in terms of collisions of the proton and individual nucleons of the nucleus with "frozen" spatial distribution. This stage of reaction is usually treated as so called ***intranuclear cascade (INC)*** of proton - nucleon collisions. The spectra and angular distributions of nucleons are usually well reproduced by this model, however, it is not clear ***what is the mechanism of emission of fast IMF's***. If the intranuclear cascade describes adequately mechanism of nucleon emission then the logical extension should be application of ***Quantum Molecular Dynamics (QMD)*** model which do not use the mean field approximation to describe the interaction among nucleons and therefore treats more exactly fluctuations of the nucleon density in the struck nucleus, thus it should be able to describe emission of clusters of nucleons. There are indications [1] that indeed, QMD model better describes dynamics of the first, violent stage of the collision. It is, however, possible to look for some other models of fast IMF's emission, as e.g. ***coalescence*** of nucleons [2], ***shattering*** of the cold target spectator matter [3], ***percolation*** model of the emission [4, 5].

The set of nucleon-nucleon collisions initiated by the incoming proton results in deposition of energy in the nucleus. This is because the nucleons which participate in the collision with incident proton can later collide with other nucleons in the nucleus and thus energy will be distributed over all nucleons of the nucleus. Such an excited nucleus can emit nucleons or complex particles before achieving statistical equilibrium (***pre-equilibrium reactions***) and can also reach statistical equilibrium. The next question, which can have many answers is ***how quickly the struck nucleus achieves equilibrium*** and whether this is the full equilibrium, in which all degrees of freedom are equilibrated, or only partial equilibrium of some degrees of freedom. Due to statistical fluctuations of the energy distribution among the nucleons - excited nucleus can "evaporate": single nucleons or composite particles (***compound nucleus processes***). Again the question arises whether multiple emission of fragments observed in multifragmentation has ***sequential or simultaneous mechanism*** and thus whether it may be treated as evaporation or as indication of ***liquid-gas phase transition***.

To answer these questions it is necessary to compare the model predictions with the experimental data which are expected to be sensitive to various reaction mechanisms. In the next chapter the investigations of proton – Au nucleus collisions, published up to now in the scientific literature, will be discussed. It follows from this literature overview, that strong increase of the emission of intermediate mass fragments (IMFs) can be anticipated in the region of 1 – 3 GeV proton beam energy. Since measurements of IMFs with $Z \geq 3$ for p + Au system at these energies are practically lacking in the literature and the existing data concern mainly inclusive observables (creation cross sections for various ejectiles) the task was undertaken to perform in the present work more exclusive experiment for measuring the double differential cross sections $d\sigma/d\Omega dE$ for the gold target at 2.5 GeV proton beam energy with identification of mass and charge of the ejectiles. Light and intermediate mass fragments were measured which should allow for investigation of charge, mass, energy and (to some extent) angular distributions of the fragments.

The third chapter is devoted to a short overview of theoretical models with the emphasis put on four models which we like to apply for the analysis, namely; ***intranuclear cascade model (INCL)*** describing the first, fast step of the reaction, ***the generalized evaporation model (GEM)*** which deals with the second stage of the reaction treated as the evaporation from equilibrated nucleus, and ***Fisher's droplet model*** which allows for compact and analytical description of some aspects of multifragmentation and especially gives prediction of observables for the nuclear liquid – gas phase transition. We discuss also the phenomenological model of two moving sources which emit the observed particles.

In the fourth chapter the idea of the experimental procedure and the apparatus are presented, whereas the analysis of experimental data and experimental results are shown in the fifth and sixth

chapter respectively. Model calculations and their comparison with the present experimental data are discussed in the seventh chapter while conclusions and discussion of results are collected in the last, eighth chapter of the work.

Chapter 2

Overview of p+Au investigations

In the present chapter an overview of investigations of proton – Au collisions performed in the past is discussed. The publications which deal with the above subject are listed in the table 2.1 with short comments extracted from these papers. The experimental results and their interpretation proposed by authors of the studies is presented. Since various experimental methods and theoretical models were used in these investigations and, moreover, the detailed subjects of the studies differ from reference to reference a task was undertaken to systematize the information contained in these publications.

The following picture of phenomena observed up to now for proton – Au nucleus collisions comes into view. Three mechanisms, distinctly separated by various ranges of mass of emitted ejectiles manifest themselves; *fragmentation* results in emission of intermediate mass fragments (with $4 < A <\sim A_{Au}/3$), *spallation* dominates for residues with mass in the neighborhood of the Au target mass whereas the *fission* sets in the region of intermediate masses. These facts are well illustrated by Fig. 2.1 which was taken from publication of S. G. Mashnik et al. [6], where results of various theoretical models (lines) are compared with existing experimental data at 0.8 GeV proton beam energy (dots). It seems that the main contribution to the reaction cross section comes from the spallation process. Fragmentation has a smaller share and fission is responsible for 5 – 10 % of the total reaction cross section. This proportion is almost constant for proton energies higher than 10 – 20 GeV but it varies at smaller energies as can be seen in Fig 2.2. It is clearly visible in Fig.2.1 that spallation (for products with $A > 130$, $Z > 58$) gives the largest contribution, fission yield ($40 < A < 130$, $20 < Z < 58$) is of an order of magnitude smaller and no data for fragmentation ($A < 40$, $Z < 20$) are available at this energy. The lack of the fragmentation data is not accidental, because for the Au target only few experiments exist in which IMF's were detected (conf. table 2.1). This is also shown in the figure 2.5 where only radioactive ejectiles represent products of the fragmentation reaction. This is because the total production cross sections were measured almost only for radioactive IMFs (besides experiments performed with thin targets in which differential cross sections for IMFs were determined).

It is interesting to compare the constraints which are put to the theoretical models by mass and charge distributions of the ejectiles originating from spallation, fission and fragmentation. It seems from inspection of Fig. 2.1 that the spallation is the least restrictive for selecting the proper model of the reaction, fission clearly discriminates the models represented by dashed lines,

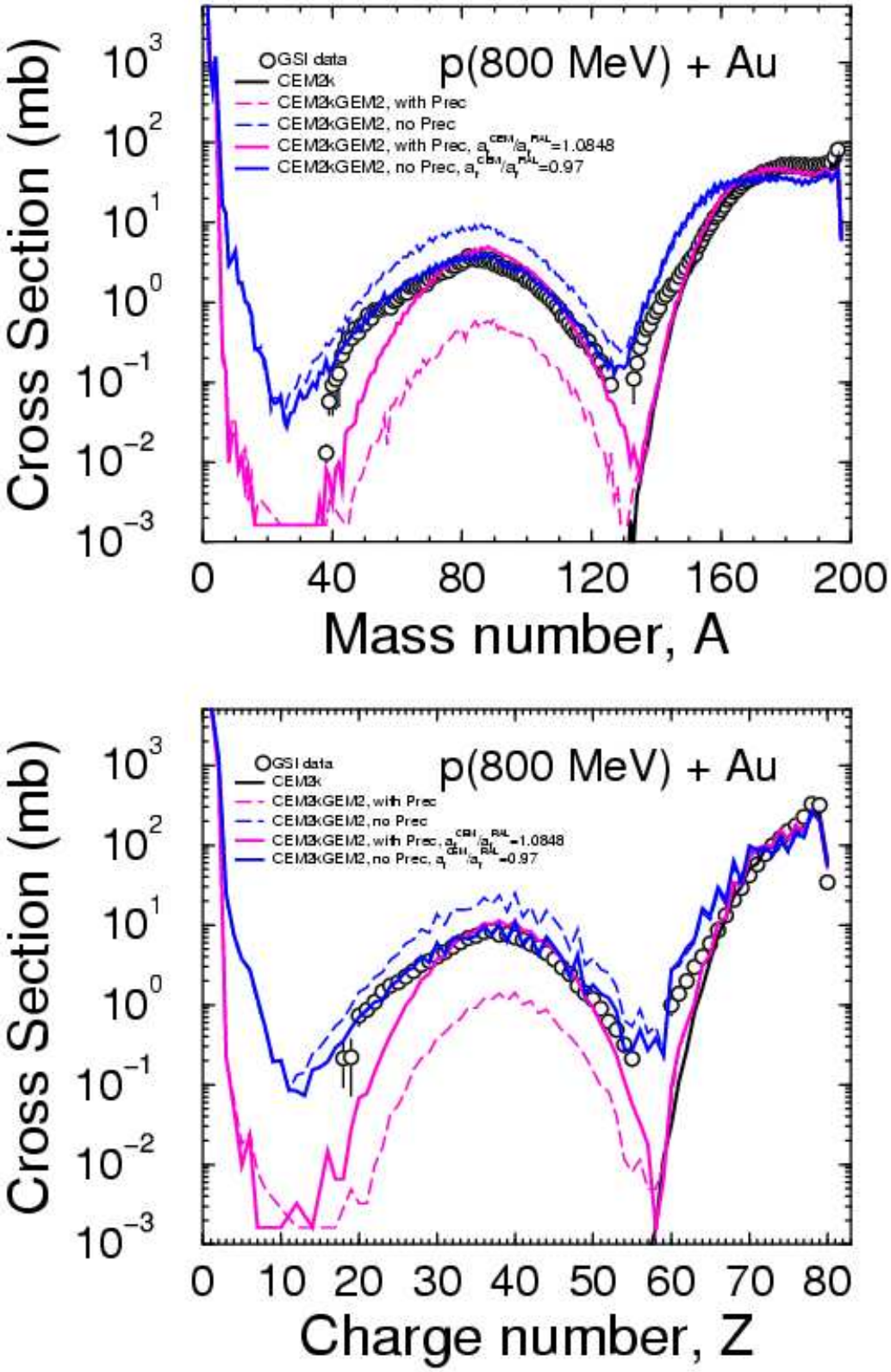

Figure 2.1: The dots represent mass yield distribution (upper part of the figure) and charge yield distribution (lower part of the figure) of ejectiles from p+Au collisions at 0.8 GeV proton beam energy. The lines show results of theoretical calculations performed in the frame of several different models. The figure is taken from [6].

whereas the fragmentation can serve as the ultimate test which selects one of the models represented by solid lines, which are almost of equal quality for description of fission and spallation reactions. Thus it is obvious that the knowledge of cross sections for IMF's production is crucial for testing the theoretical models of the reaction mechanism.

It should be emphasized, that observation of the heavy, target-like residuum unambiguously indicates the spallation mechanism of the process, however, observation of IMFs does not necessarily proofs the presence of the fragmentation mechanism. For example, deep spallation may be accompanied not only by emission of nucleons and light charged particles (with $Z \leq 2$) but the emission of IMFs is also not excluded.

In figure 2.2 the experimental mass yield distributions are shown for several proton beam energies from) 0.329 GeV up to 2.6 GeV. The figure adapted from Michel et al. [7] again shows a distinct difference between range of the highest masses of ejectiles produced in the spallation process and ejectiles within range of masses around $A \sim 100$, which appear due to fission. At higher energies the peaks in the mass distribution corresponding to the both processes become broader and the fission peak is less pronounced for higher proton beam energy. Therefore at the highest energy it is not possible to find a clear boarder between masses of fission fragments and the deep spallation residues. It is worthy to point out again that ***only a few IMF's with masses smaller than $A \sim 40 - 50$ are represented in these experimental data***.

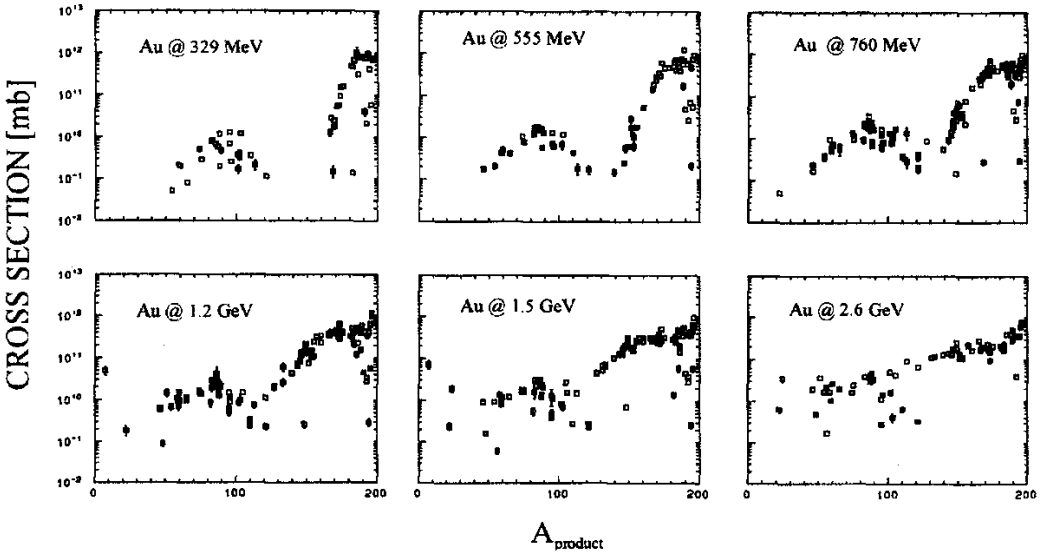

Figure 2.2: The dots represent experimental mass yield distributions up to several GeV proton beam energy. The figure is taken from R. Michel at al. [7].

Production cross sections of *spallation* processes rise rapidly above an energetic threshold (cf. Fig. 2.3), go through a maximum and then decrease again, finally approaching a constant cross section at the highest energies [8], [7]. It is very well visible in the Fig. 2.3, that the energy at which the rapid increase of the spallation cross section appears, shifts towards higher values when the mass of the spallation residuum decreases. This explains why the distribution of mass yields for spallation products shown in the Fig. 2.2 broadens with the beam energy.

The cross section of *fission* reactions varies not more than ~ 30 % in the energy region 0.6 – 29 GeV [9]. The highest values appear at 2 and 3 GeV. Fission cross section remains nearly

constant as the incident energy increases further up to 300 GeV [10]. It seems, that excitation function for fission resembles to large extent the excitation function of spallation reactions.

The excitation functions of light nuclides ($A \leq 40$), produced by *fragmentation* of the bombarded Au nucleus exhibit different behaviour. They increase monotonically (cf. Fig.2.5) to the constant limit at asymptotically high energies, thus they do not display such a peak as the spallation excitation curves. The levelling of all excitation curves for p+Au collisions appears at $\sim$ 10 GeV and the cross section remains constant within $\sim$ 20 % up to 300 GeV [11, 12]. This is consistent with a saturation in the energy deposition [13, 14].

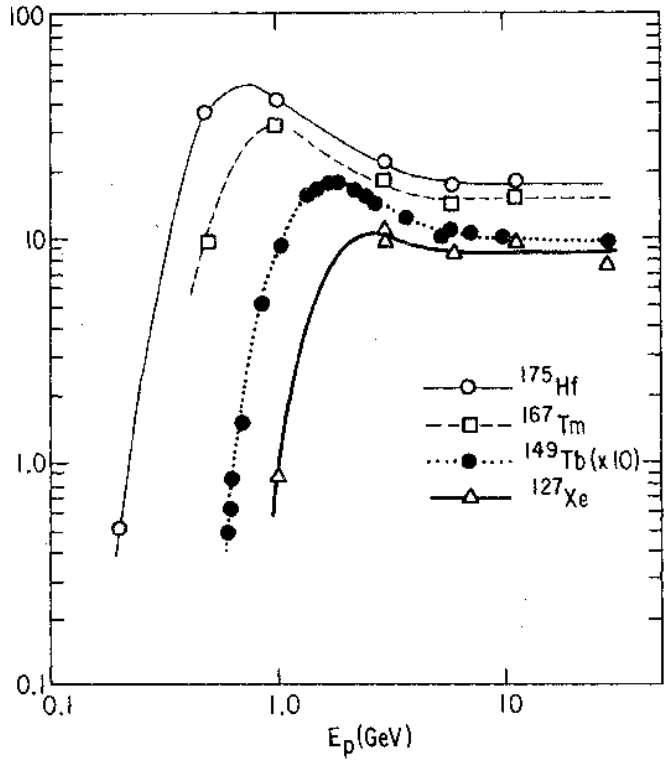

Figure 2.3: Examples of excitation curves for spallation in p+Au collisions. Dots represent experimental data whereas the lines are drawn to guide the eye. It should be noted that the energy range shown in the figure is smaller than that discussed in the text. The figure is adapted from ref. [8].

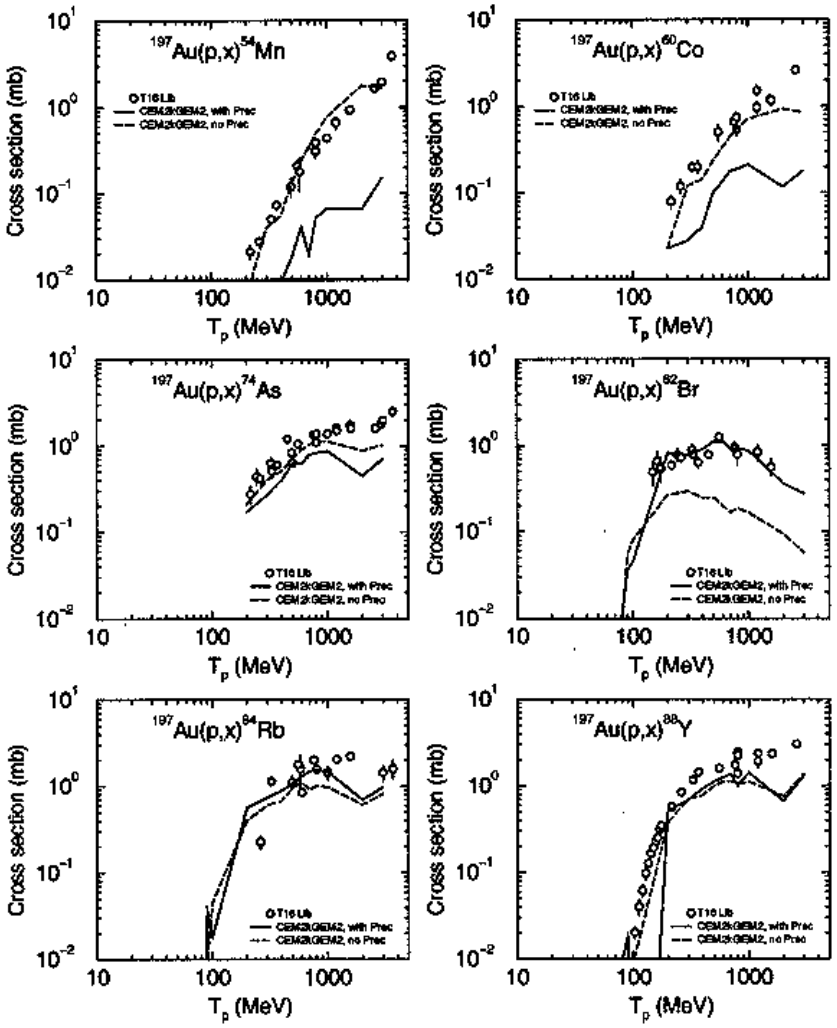

Figure 2.4: Examples of excitation curves for fission in p+Au collisions. Dots represent experimental data whereas the lines show results of calculations performed in the frames of different theoretical models discussed in the ref. [6]. It should be noted that the energy range shown in the figure is smaller than that discussed in the text. The figure is adapted from the paper of Mashnik et al. [6].

Whereas almost ”frozen” situation exists at very high energy, there is observed strong variation of the cross sections for all discussed reaction mechanisms in the region of 1 – 10 GeV of the proton energy. The increase of the cross sections is observed (at least for lowest energies in the mentioned region) and the contributions of different mechanisms vary. ***Thus it may be***

anticipated that the most interesting phenomena take place just in this energy region.

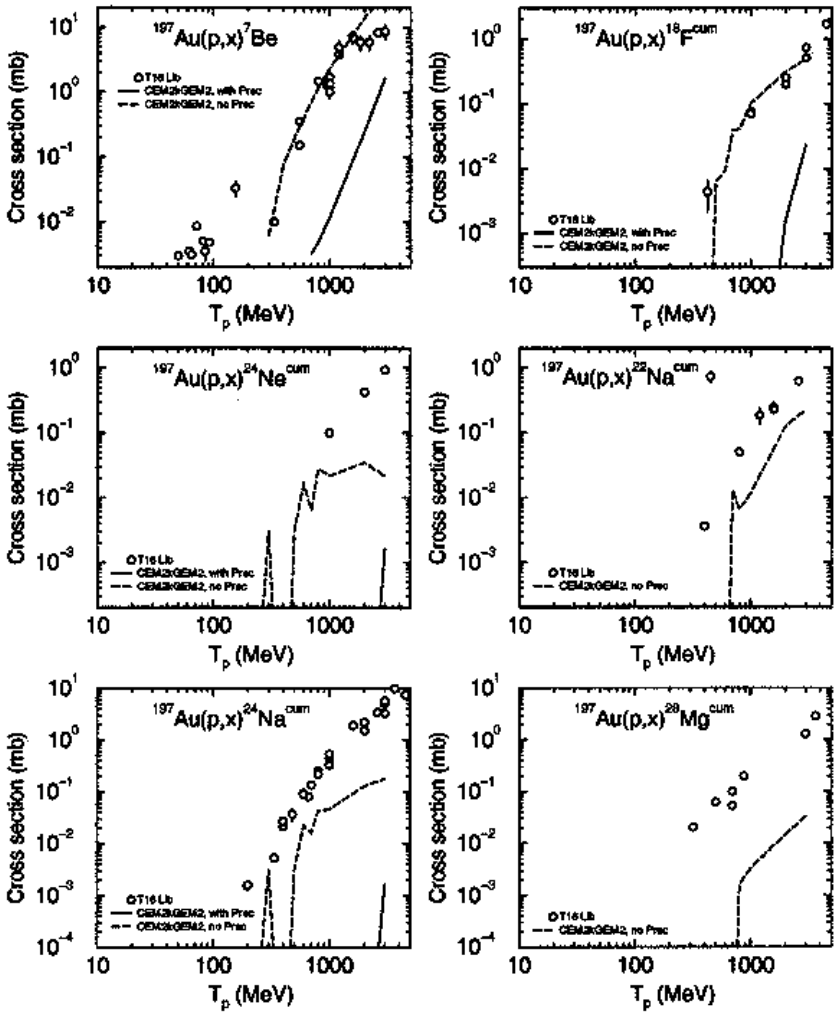

Figure 2.5: Examples of excitation curves for fragmentation in p+Au collisions. Dots represent experimental data whereas the lines show results of calculations performed in the frames of different theoretical models discussed in the ref. [6]. It should be noted that the energy range shown in the figure is smaller than that discussed in the text. The figure is adapted from the paper of Mashnik et al. [6].

In contrast to the non-monotonic behaviour of spallation and fission cross sections, the fragmentation process exhibits fast increase of the cross section – cf. Fig. 2.5.

The shape of angular distributions varies in this energy range, e.g. the forward to backward ratio of fragments emission has a maximum near 3 GeV decreasing again at higher energies [15]. The nonisotropic emission is observed also at higher energies, especially the sideward flow of intermediate mass fragments toward 70^o was observed at 12 GeV [16] as well as at 28 GeV [17] and was interpreted as indication of some exotic phenomena, e.g. toroidal shape of the excited

nucleus [16] or presence of the shock waves [17].

The specific behaviour of the fragmentation process observed in the discussed energy region of 1.0 – 10.0 GeV may lead to the hypothesis of the nuclear liquid - gas phase transition [18]. At normal nuclear density ρ_0, it means 0.17 nucleons/fm^3, the nucleus is regarded as liquid. The liquid-gas phase transition starts when the normal nuclear density decreases significantly below the nucleus ground state density. Then internucleon distances are large and a nucleonic gas is formed whereas at an intermediate density some nucleons are joined together to form clusters and then the liquid-gas mixed phase appears. This may be achieved by violent collision of the nucleus with a heavy ion which leads to compression of the nucleus followed in turn by its decompression. If the decompression is vigorous enough the excited nucleus can reach density significantly smaller than the ground state density. Fig. 2.6 shows two scenarios, when the velocity of initial expansion of the nucleus is large enough to achieve in response sufficiently low densities of the nucleus. The nucleus may take during its decompression and cooling a path shown by the first arrow. This path leads to the phase transition. However, if the initial expansion velocity of the nucleus is too small to induce large enough response then the system reaches a turning point and shrinks back to its initial density (second arrow in the figure).

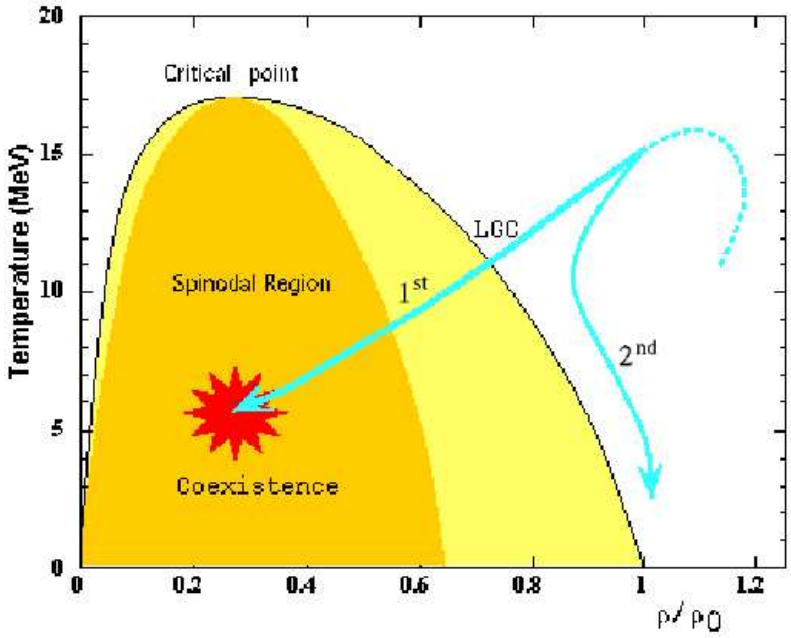

Figure 2.6: Phase diagram and critical region of the liquid-gas phase transition. The liquid-gas coexistence curve is defined as LGC (figure adapted from [19]).

The above figure can be also used to discuss possibility of the nuclear liquid – gas phase transition in the proton – nucleus collisions. One can expect that a proton impinging on the nucleus is not able to induce compression of the nuclear matter. However, the collision with proton may excite the nucleus, what would be illustrated by vertical shift on the phase diagram, out of the point $\rho/\rho_0 = 1, T = 0$ representing the ground state. It turns out that the nucleus excited by collision with a proton can reach the same path in the phase diagram (first arrow) as the nucleus compressed and excited by heavy ion collision.

Table 2.1: Au+p experiments

Proton energy [GeV]	Ejectiles	Reference	Comments
0.56–0.91	$Z > 43$	[20] [12]	production cross sections, limiting fragmentation accurate to 20–30 %
0.8	fission fragments	[21]	isotopic identification
0.8	fission fragments	[22]	fission dynamics
0.8	60< Z <80	[23]	two-step model of spallation
1.0	He,Li,Be,B	[24]	temperature $T_0 \sim 4$ MeV from double isotopic ratios
1.0	$3 < Z < 19$	[25]	mean slope parameter of the energy spectra $d\sigma/dEd\Omega$, integral cross sections
1.2, 1.8	n,H,He	[26]	E*, preequillibrium emission
0.48, 2.2	multiplicity of Z=1, $Z > 3$ fission fragments	[27]	ejectiles gated by neutron multiplicities
2.2	^{8}Li	[28]	some other process besides evaporation must also play an important role
2.5	Z=1–3	[29]	$d\sigma/dEd\Omega$ model calculations
≤ 2.6	many products	[7]	10000 production cross sections
1.0, 3.0	^{7}Be	[30]	cross section increases with energy, production probably by evaporation
1.0 – 3.0	^{24}Ne,^{24}Na	[31]	ratios of cross sections are energy independent but cross sections rise with energy
0.9 – 4.0	50< Z <81	[14]	study of the total cross section with increasing energy to limiting fragmentation
2.1, 4.9	He up to Ar for heavier targets	[32]	$d\sigma/dEd\Omega$ at several angles moving source fit of spectra
0.2 – 6.0	number of radioactive products	[8]	mass yields and excitation curves
8.1	Z=3 – 11	[34]	multifragmentation as nuclear liquid gas phase transition with T_c=20± 3 MeV
9.3	Li – O, fission fragments	[35]	strong evidence for a continuous phase transition, $\tau = 2.35 \pm 0.05$ $\sigma = 0.5 \pm 0.1,\ T_c = 8.3 \pm 0.2 MeV$
10.6	Sn – Hg	[36]	total and partial charge-changing cross sections higher than for $T_p < 1$ GeV
11.5	five nuclides A$\sim$ 131	[37]	charge dispersion
12	$40 \leq A \leq 130$	[38]	mass-yield and charge-dispersion curves
12	IMF's $Z \geq 7$	[16]	$d\sigma/dEd\Omega$ at 7 angles sideward flow of IMF's toward 70^{o} unusually shaped excited nucleus

Table 2.2: continuation of the table 2.1

5.2–13.8	H,He,Li–O	[13]	consistent with limiting fragmentation and saturation of energy deposit
28	$6< Z <12$	[17]	$d\sigma/dEd\Omega$ at several angles broad peaks at $\sim 70^{o}$ – shock waves ?
0.6 – 29	fission fragments	[9]	$\sigma(f)$ varies little, 59 - 76 mb maximal values at 2 and 3 GeV ternary f. starts at 2 GeV ($\sim 0.2\%$)
2.0 – 29	Rare-gas isotopes	[39]	Ne and Ar yields do not formed by fission or spallation
1.0, 158	$Z \geq 7$	[40]	Transverse momentum for spallation, fission and fragmentation
0.6 – 300	fission fragments	[10]	no substantial change in ternary to binary fission ratio, forward momentum transfer peaks at $\sim$2 GeV and decreases at higher beam energies
2.0 – 300	^{24}Na,^{28}Mg	[15]	forward-to-backward ratio exhibits a maximum near 3 GeV decreasing from a value of about 2.0 at 3 GeV to 1.3 at 300 GeV
1.0 – 300	$46< A <103$	[41]	forward-to-backward ratio =1.0 at 300 GeV fission contributes appreciably at 1 GeV other mechanisms at and above 11.5 GeV
11.5 – 300	^{22}Na – ^{196}Au	[11]	$\sigma(300)/\sigma(11) = 1.0 \pm 0.2$ charge dispersion and mass yield curves
200, 300	fission fragments	[42]	binary and ternary fission

A lot of theoretical and experimental work [43–45] has been done in order to clarify the fundamental question of how a highly excited, low density nuclear system disassembles. The continuing search for the signature of liquid-phase transition remains a central part of the experimental programs with nuclear collisions. In the case of p+Au system there were performed studies at 8.1 [33] and 9.3 GeV [35] proton beam energy which authors claim that strong evidence for a phase transition was found. Both the papers report the derived "critical temperature" values T_c= 20$\pm$3 MeV (90 % confidence level) [33] and T_c=8.3$\pm$0.2 MeV [35]. It seems that these values completely do not agree but it should be emphasized that "critical temperature" has different meaning depending on the model which were used for its extraction. This is discussed in [33] where overview of the studies of the nuclear liquid–gas transition for Au–nucleus fragmentation by various projectiles is presented.

It is interesting to note that the temperature parameter extracted at 1.0 GeV energy from the double isotopic ratios by M. Andronenko et al. [24] is almost identical for various target nuclei from Al up to U. Since the excitation energy per nucleon is smaller for heavier targets at the same beam energy, the equality of temperatures for different targets may, perhaps, indicate that temperature of nuclei does not change in spite of variation of the excitation energy per nucleon. Such behaviour is typical for the phase transition in which increase of the stored energy does not increase the temperature. Furthermore temperature found in [24] for 1.0 GeV proton beam

energy is smaller (T $\sim$ 4 MeV) than those found by Karnaukhov et al. [33] (T $\sim$ 20 MeV) and by M. Kleine-Berkenbusch et al. [35] (T $\sim$ 8 MeV) for 8.1 GeV and 9.3 GeV proton energy, respectively. Thus, it seems that at higher beam energies the temperature again increases as it happens after phase transition . If this interpretation is correct, then the nuclear liquid-gas phase transition should start even at 1 GeV energy and manifest itself for the energies from 1 to 10 GeV, where cross sections for emission of IMF's strongly increase.

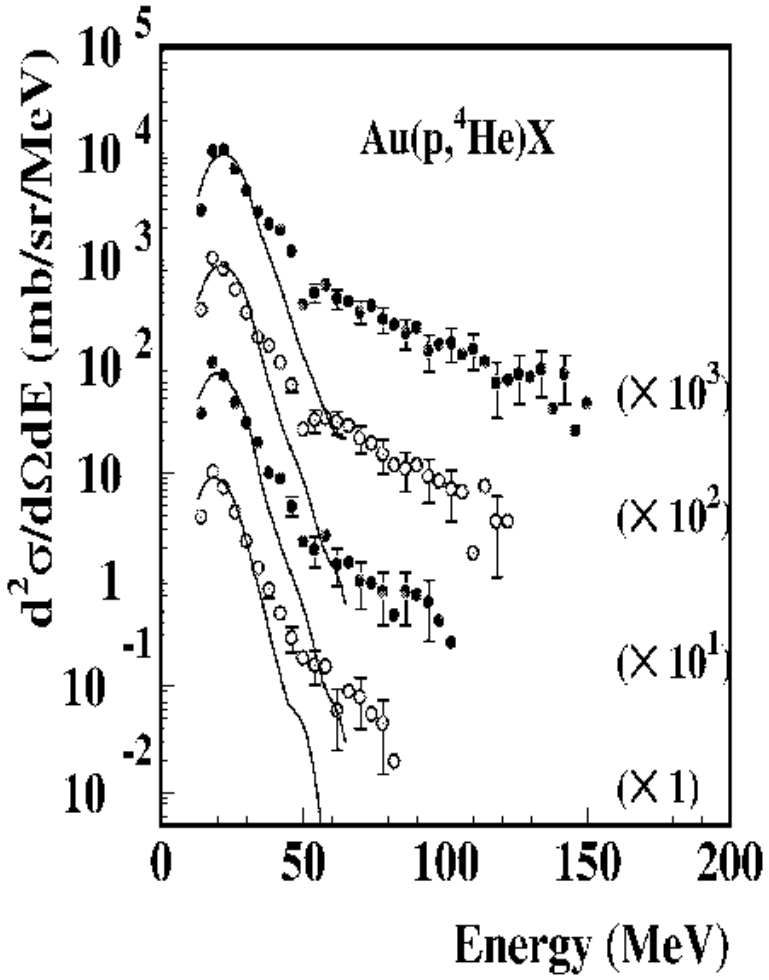

Figure 2.7: The dots represent experimental spectra for Au(p,^{4}He) reaction at T_p=2.5 GeV proton beam energy. The lines show results of an evaporation model. The figure is taken from A. Letourneau at al. [29].

It is obvious from this overview of the experimental investigations performed for the p+Au system that the inclusive experiments at which only total production cross sections are measured do not allow for unambiguous interpretation of the experimental data. In the last years several experiments have been done to study exclusive reactions, devoted especially to measurements of double differential cross sections $d\sigma/dEd\Omega$ [27,29]. A typical result of such a study is presented in the Fig. 2.7. The energy spectra of the α - particles are shown measured at several scattering angles. Two distinct contributions are visible in the spectra. The low energy part can be described well by

evaporation model whereas the high energy tail of the energy spectrum has no model explanation so far. Several different possibilities of such contribution are possible, what enables investigators to judge on the details of the reaction mechanism, and to exclude some of the reaction models. For example, the authors of the ref. [29] showed that the coalescence model is able to improve description of the high energy spectra for d,t and ^{3}He and to some extent also for ^{4}He, however, this can be done only when significant deterioration of the description of the nucleon spectra is introduced.

Unfortunately the most of the papers at which differential cross sections are presented, as e.g. the ref. [29], contain information only on the light particles ($Z \leq 3$), what prohibits the complex analysis which should involve also the IMFs besides other possible experimental information. In this thesis, the experimental study is presented of the proton induced reactions on the gold target at the proton beam energy of 2.5 GeV. At this energy a significant onset of multifragmentation process is expected and influence of the postulated nuclear liquid-gas transition should be visible. The new data which consist of double differential cross sections $d\sigma/dEd\Omega$ for elementally and isotopically identified light particles and intermediate mass fragments should allow to obtain additional information as e.g. to extract temperature parameter, the power law exponent τ of the mass distribution (yield of fragments versus fragment mass) as well as the isotopic yields.

Chapter 3

Theoretical models of fragmentation

The present thesis deals, as it was discussed in the previous two chapters, with the proton - Au collisions at proton beam energy of 2.5 GeV. Large values of the nuclear thermal excitation energy (>l000 MeV) and temperature (>10 MeV) may be achieved for short periods of time in such high energy proton – nucleus reactions. Besides the well known and understood "standard evaporation" and conventional fission (of heavy nuclei) the highly excited nuclei can decay by the emission of several IMFs, i.e. multifragmentation occurs. The multifragmentation can be the result of sequential binary processes, "statistical" decay into many fragments (described by passage through a transition state or the establishment of statistical equilibrium among fragments in a critical volume), or a dynamical process in which the system evolves into regions of volume and surface instabilities leading to multifragment production. Each of these scenarios may be the background for a specific theoretical model.

The present chapter is devoted to discussion of theoretical models elaborated for the description of multifragmentation. From among them the selected three models will be described in more detail: the ***intranuclear cascade model***, the ***generalized evaporation model (GEM)***, and the ***Fisher's droplet model***. We discuss also the phenomenological model of two moving isotropically emitting sources which enables one to extract quantitative information on the reaction.

According to the most commonly accepted hypothesis, the high energy proton – nucleus reaction proceeds in two stages. The first step of the reaction can be regarded in terms of collisions between the incident particle and the individual nucleons in the nucleus. This is because the wave packet representing the proton impinging on the nucleus has small dimensions, i.e. the length of the de Broglie wave is small in comparison to dimensions of the nucleus and, furthermore, the velocity of the projectile is much larger than the velocity of the Fermi motion of nucleons in the nucleus, thus the spatial distribution of nucleons is almost "frozen" during the collisions. These collisions can result in emission of several fast nucleons or groups of nucleons and in "heating" of the remnant nucleus.

The first stage of the reaction is usually described as intranuclear cascade and the models used for this purpose differ mainly in the treatment of details of the mechanism and the computational solutions. In the next section the ***intranuclear cascade model (INC)*** will be presented and compared with other models as e.g. Boltzmann - Uehling - Uhlenbeck (***BUU***) model or Quantum Molecular Dynamics (***QMD***) model.

The excited nucleus can achieve thermodynamic equilibrium and remain in it, depending on the excitation energy, by quite a long time ($\sim 10^{-18}$ s) in comparison to the time of the first collision stage ($\sim 10^{-22}$ s). Deexcitation of such a compound nucleus may proceed by "evaporation" of light particles (with $Z \leq 2$) and IMFs or by fission (especially for heavy and fissile target nuclei). The statistical models are used to describe this process. Sequential (e.g. ***GEMINI*** model [46],

Generalized Evaporation Model – ***GEM*** [47]), or simultaneous (e.g. Statistical Multifragmentation Model – ***SMM*** [48] or Microcanonical Metropolis Monte Carlo Model – ***MMMC*** [49]) emission of fragments is taken into consideration. The data obtained in the present work were analyzed using the Generalized Evaporation Model of Furihata and thus this model will be discussed below in more detailed manner.

The excited nucleus may evolve to the state of instability for decay into multiple fragments and such multifragmentation can be described by above mentioned statistical models. However, it is appealing to analyze the data also in the frame of the Fisher's droplet model which predictions can be formulated in a simple, analytical way and can be in the straightforward manner compared to the experimental data [50]. This model will be discussed in the third section of the present chapter. The last section is devoted to the description of the phenomenological model in which it is assumed that the observed particles are emitted from two moving sources.

3.1 Intranuclear Cascade Model

The intranuclear cascade model (INC) was first proposed by Serber in 1947 [51]. The successful realization of this model by means of the the Monte Carlo simulations has been presented by Goldberger which made first calculations by hand in 1948 [52]. First computer simulations were done by Metropolis et al. in 1958 [53] whereas standard methods of INC implementations were formed in publication of Guthrie, Alsmiller and Bertini [54]. In the present chapter we discuss the intranuclear cascade model in the standard Liège version INCL4.2 [55].

The Intranuclear Cascade (INC) Model simulates – by the Monte Carlo method – sequence of the nucleon - nucleon collisions proceeding inside the nucleus. This is equivalent to solving the transport Boltzmann equation for the time dependent distribution of the nucleons in the nucleus, treating explicitly collisions between the nucleons. As it was mentioned above, such a picture of the reaction is justified in the case when the energy of the projectile is high enough. The INC is stopped when signatures are fulfilled, which indicate the equilibration of the decaying nucleus. In the INCL4.2 code the equilibration time τ is determined by reaching a constant emission rate of cascade particles during the INC process. Typically τ is of the order of 10^{-22}s or 30 fm/c. The longer this somewhat "artificially" chosen time the smaller E^* being left for the evaporation process. In the Bertini like INC codes (not used in the current work) the switching is performed when the most energetic scattered nucleon in the nucleus has decreased below a given cutoff energy of 7 MeV above the Fermi energy.

The description of each cascade involves three different stages: (i) initialization of the properties of the spatial and momentum distribution of nucleons in the nucleus, (ii) propagation of nucleons inside the nucleus, and (iii) collisions of the nucleons.

(i) The nucleus is treated as a cloud of the Fermi gas of nucleons. The nucleons are kept together by a static (time independent) mean field with the radius compatible with the dimensions of the nucleus. This seems to be reasonable approximation for proton induced reactions because in these collisions the nuclear density is not significantly modified, on the contrary to the heavy ion reactions, where strong compression and deformation of the nucleus may happen. Target nucleons are positioned randomly in the spherical nucleus and their momenta are also randomly distributed in the Fermi sphere. Radius of this sphere (Fermi momentum) is constant for the constant density of the nucleus whereas it is evaluated in a local density approximation for density of nucleons varying on the surface of the nucleus. At the beginning of the proton – nucleus collision, i.e. for time t=0, the impact parameter of the proton

on the target nucleus is chosen with the uniform distribution of the impact points over the area of the cross section of the nucleus.

(ii) The nucleons move along the trajectories governed by the classical equations of motion. In the simplest version (with the constant mean potential) it is the straight line trajectory. When the nucleon hits (from inside) the surface of the nucleus, it is reflected if its energy (kinetic plus potential energy) is smaller than the threshold value. In other case the nucleon leaves the nucleus with the probability determined by the penetration factor. Relativistic kinematics is applied throughout the cascade and the conformity with the energy conservation law is checked. The momentum is conserved only in some approximate manner because reflections from the edge of the potential are equivalent to scattering on the infinitely heavy wall.

(iii) If trajectories of two nucleons during their motion reach the minimal relative distance of approach smaller than $\sqrt{\sigma_{total}/\pi}$, where σ_{total} is the total nucleon-nucleon cross section, then the collision between nucleons is assumed. In the old versions of intranuclear cascade model the free nucleon-nucleon cross section was used, whereas at present versions the in medium cross section is applied. Since the nucleons obey the Fermi statistics, not all final states of the virtual collision are allowed. The Pauli exclusion principle forbids the collision when the presumed nucleon final state is already occupied. Elastic and inelastic scattering (with creation of pions and the Δ resonances) are taken into account. The direction and energy of the flight of the nucleon escaping from the collision are sampled according to experimental angular distributions.

The standard Liège intranuclear cascade model INCL2.0 is able to reproduce well neutron double-differential cross sections and the residue mass spectrum [56] as representatively shown for proton induced reactions on Pb target in Fig. 3.1.
The quality of reproduction of the data is the best for the highest energy and for larger angles where quasielastic peaks are not visible. The simplicity of the model and speed of calculations makes the INCL model very attractive. Of course the model cannot efficiently describe evaporation of the particles from the compound nucleus formed in the first stage of the reaction because of two reasons: (a) the evaporation is very sensitive to the density of states of the nuclei participating in the reaction, whereas the single particle density of states implicitly present in the INCL calculations is not exact enough, and (b) the calculations of the cascade to such long times as those characteristic for the compound nucleus emission is not stable numerically and very inefficient. The other very serious drawback of the INCL model is absence of correlations between nucleons, which could lead to emission of complex fragments. This is because the INCL is the single particle model with the mean field treated in oversimplified manner. The mean field of the INCL is assumed to be constant in full volume of the nucleus or modified at the surface of the nucleus, but always it is a static field.

The dynamic modification of the mean field is more exactly taken into consideration in the Boltzmann-Uehling-Uhlenbeck (BUU) model (see eg. [57]), where each nucleon is represented in the Monte Carlo simulation by a number (~ 100) test particles which after averaging simulate the time dependent density distribution of nucleons, which in turn is unambiguously defining the time dependent mean field. This, of course is connected with increasing the complexity of the program and the time of calculations. Even in the case of BUU model the correlation between nucleons is to small for proper prediction of complex fragment emission.

In the Quantum Molecular Dynamics (QMD) model (see e.g. [59] the correlation between nucleons is sufficiently strong to produce fluctuations of the density big enough to result in emission of clusters of the nucleons. In this model the actual distribution of nucleons represents the

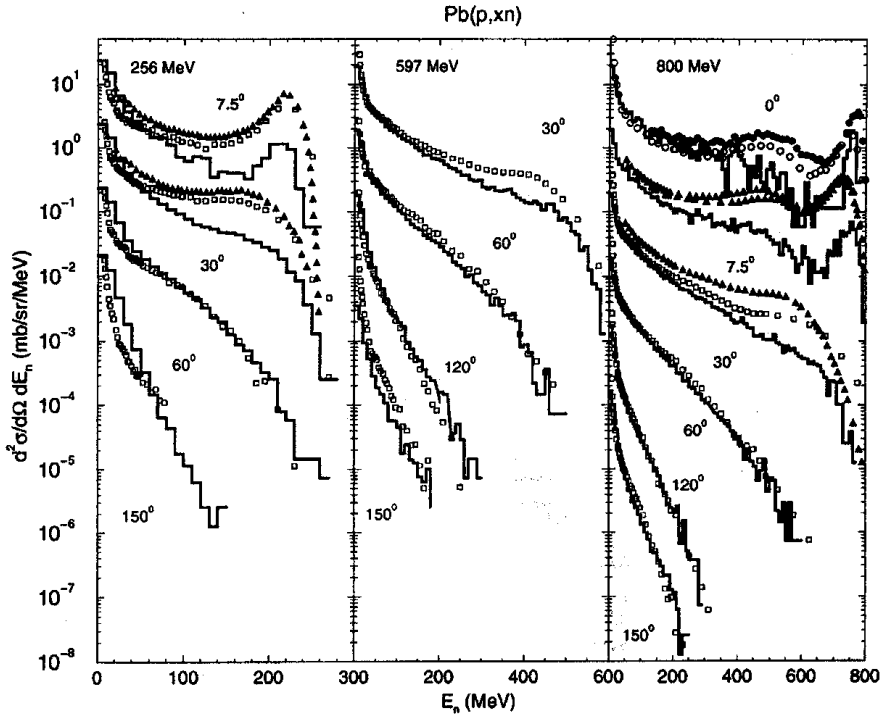

Figure 3.1: The symbols show the experimental double differential cross sections presented as energy spectra for several scattering angles at three proton beam energies. The histograms depict results of calculations by means of the Liège INC model. The figure is taken from J. Cugnon at al. [56].

time dependent density of the nucleus. Thus the model preserves all correlations which are present initially or are built up in the course of the reaction. It replaces the mean field of the BUU approach, by sum of two nucleon interactions. The improvement introduced by such treatment of the mean field is accompanied by still higher complexity of the computer programs and increase of the time of calculation to over three order of magnitude larger values than those characteristic for INCL calculations. However, this model may give the most realistic description of the dynamics of the high energy fragment emission in the first stage of the proton – nucleus collisions. In Fig. 3.2 experimental energy spectra of ^{6}He and ^{6}Li fragments from p + Au collisions, studied at 2.5 GeV proton beam energy are compared with preliminary (low statistics) QMD calculations [58]. For comparison the spectra have been normalized to our experimental cross sections for ^{6}He. When taking this normalization factor into account, for all three angles under consideration the QMD calculations have the tendency to underestimate the evaporation peak for ^{6}He. Also at the same time the cross sections for the heavier elements are generally underestimated as representatively shown in the right panel of Fig. 3.2 for ^{6}Li. The QMD calculations are extremely time consuming. Therefore, although the high energy tails of the distributions calculated come close to the experimental measurement, we postponed such an analysis for the present thesis and we decided to perform two-step analysis consisted of INCL calculations for determination of the properties of the excited remnants of the fast stage of the reaction and the Generalized Evaporation Model (GEM) for description of the second stage of the reaction. Then comparison of the experimental data with the theoretical predictions can give a hint whether the fast IMFs are produced in the pre-equilibrium stage of the reaction or they appear from the emission from an equilibrated excited

nucleus (or both).

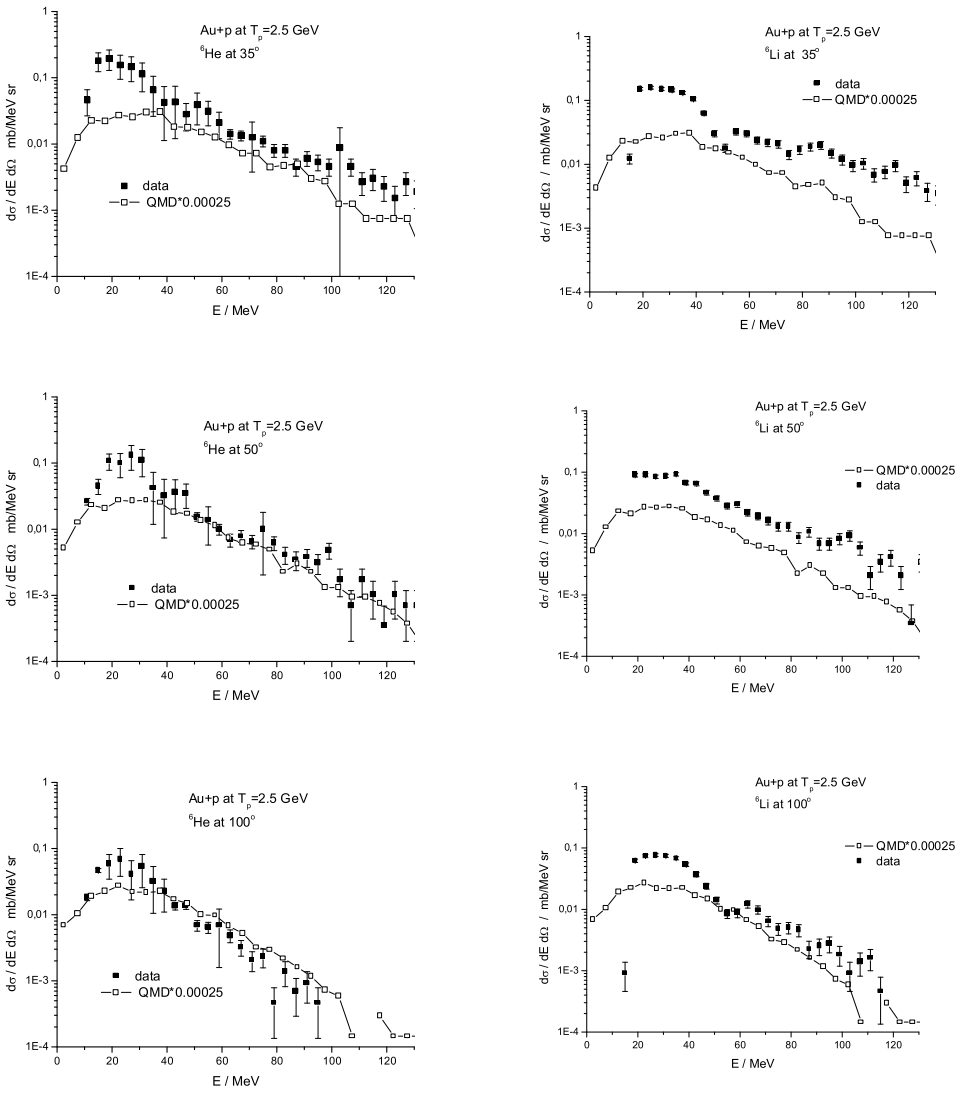

Figure 3.2: The experimental double differential cross sections (in arbitrary units) for Au+p → ^{6}He + X (left panel) and ^{6}Li + X (right panel) reactions at T_p=2.5 GeV and θ_{lab} = 35, 50 and 100 ^{o} (closed squares) and the preliminary calculations [5] within relativistic QMD (open squares) normalized to our experimental data.

3.2 Generalized Evaporation Model

It is said that the system is in the ***thermodynamic equilibrium*** if the following types of the equilibrium are simultaneously achieved: (i) the ***mechanical equilibrium*** (balance of all acting forces), (ii) the ***chemical equilibrium*** (the system does not experience internal structure changes of its

constituents), and (iii) the ***thermal equilibrium*** (the relevant degrees of freedom which characterize the system share equally its macroscopic energy). One can then define a common ***temperature*** which characterizes the energy attributed to each degree of freedom. Temperature together with the other time independent thermodynamic coordinates like density and pressure describes the state of the system through equation of state which links together all mentioned quantities.

The statistical model is able to describe well the systems which achieved the thermodynamic equilibrium, however, it is not necessarily the case for the systems which are out of the thermodynamic equilibrium. The setting up of thermodynamic equilibrium over the whole or part of the interacting system of particles is therefore a central but open question. In particular, it is not clear to which extent the excited remnant of the first stage of the proton – nucleus collision achieves the equilibrium. Thus, application of the statistical model for description of the emission of particles from the second stage of the reaction is performed with the tacitly made assumption that the thermodynamic equilibrium may be taken for granted.

In practice the model of the intranuclear cascade (or equivalent) is applied for description of the first stage of the nuclear collision and as already mentioned earlier the calculations are stopped in such a moment of time , when achieving of the equilibrium may be conjectured. In the present thesis the INCL4.2 computer code was applied for this purpose. Discussion concerning criteria of the termination intranuclear cascade is presented by J. Cugnon et al. in the ref. [56]. Description of the second stage of the reaction, starting with the equilibrated excited nuclei was done by means of the generalized evaporation model described below.

The generalized evaporation model (GEM) of S. Furihata is based on the classical Weisskopf – Ewing approach [60, 61]. According to this, the probability of evaporation of the particle j from a parent compound nucleus i with the total kinetic energy in the center-of-mass system between ε and ε+dε is defined as:

$$P_j(\varepsilon)d\varepsilon = g_j\sigma_{inv}(\varepsilon)\frac{\rho_d(E-Q-\varepsilon)}{\rho_i(E)}\varepsilon d\varepsilon, \tag{3.1}$$

where E is the excitation energy of the parent nucleus i, d denotes a daughter nucleus produced after the emission of ejectile j, and ρ_i, ρ_d are the level densities for the parent and daughter nucleus, respectively. The Q – value is calculated using the excess mass $M(A,Z)$ as $Q = M(A_j,Z_j) + M(A_d,Z_d) - M(A_i,Z_i)$. The statistical and normalization factor g_j is defined as $g_j = (2S_j+1)m_j/\pi^2\hbar^2$, where S_j and m_j are the spin and the mass of the emitted particle j, respectively. The cross section σ_{inv} for the inverse reaction is evaluated according to prescription proposed by Dostrovsky [62] as:

$$\sigma_{inv}(\varepsilon) = \sigma_g\alpha(1+\frac{\beta}{\varepsilon}) \tag{3.2}$$

where α and β are parameters and σ_g is the geometrical cross section. However, in contradistinction to the Dostrovsky model [62], the GEM considers also fragments heavier than helium nuclei. There are the 66 ejectiles listed in the table 3.1. Thus the parameters α and β of the formula 3.2 were taken from the publication of Dostrovsky et al. [62] for light particles (n, p, d, t, ^{3}He and ^{4}He) whereas for IMFs they were adopted from the work of Matsuse et al. [63].

The total decay width Γ_j is calculated by integrating eq. 3.1 with use of eq. 3.2 and is expressed as:

$$\Gamma_j = \frac{g_j\sigma_g\alpha}{\rho_i(E)}\int_V^{E-Q}\varepsilon(1+\beta/\varepsilon)\rho_d(E-Q-\varepsilon)d\varepsilon.$$

Table 3.1: The ejectiles taken into consideration in the GEM

Z_j	Ejectiles						
0	n						
1	p	d	t				
2	^{3}He	^{4}He	^{6}He	^{8}He			
3	^{6}Li	^{7}Li	^{8}Li	^{9}Li			
4	^{7}Be	^{9}Be	^{10}Be	^{11}Be	^{12}Be		
5	^{8}B	^{10}B	^{11}B	^{12}B	^{13}B		
6	^{10}C	^{11}C	^{12}C	^{13}C	^{14}C	^{15}C	^{16}C
7	^{12}N	^{13}N	^{14}N	^{15}N	^{16}N	^{17}N	
8	^{14}O	^{15}O	^{16}O	^{17}O	^{18}O	^{19}O	^{20}O
9	^{17}F	^{18}F	^{19}F	^{20}F	^{21}F		
10	^{18}Ne	^{19}Ne	^{20}Ne	^{21}Ne	^{22}Ne	^{23}Ne	^{24}Ne
11	^{21}Na	^{22}Na	^{23}Na	^{24}Na	^{25}Na		
12	^{22}Mg	^{23}Mg	^{24}Mg	^{25}Mg	^{26}Mg	^{27}Mg	^{28}Mg

where V is the Coulomb barrier.

Based on the Fermi gas model, the total level density is expressed as

$$\begin{aligned} \rho(E) &= \frac{\pi}{12}\frac{e^{2\sqrt{a(E-\delta)}}}{a^{1/4}(E-\delta)^{5/4}} \quad \text{for } E \geq E_x \\ &= \frac{\pi}{12}\frac{1}{T}e^{(E-E_o)/T} \quad \text{for } E \leq E_x \end{aligned}$$

where $a = A_d/8$ (MeV^{-1}) is the level density parameter, δ is the pairing energy of the residuum, T is the nuclear temperature given by $1/T = \sqrt{a/U_x} - 1.5/U_x$ where U_x is defined as $U_x = 2.5 + 150/A_d$. The excitation energy E_x for which the formula for level density changes the form is evaluated as E_x=U_x+δ. To get smooth connection of both formulae the E_0 parameter is determined as follows:

$$E_0 = E_x - T \cdot (logT - 0.25loga - 1.25logU_x + 2\sqrt{aU_x}).$$

The contribution of the emission of IMFs in their long living excited states is taken into account besides those which are sent in the ground state. The condition which was put to the life time of excited nuclides considered in GEM is as follows: $T_{1/2}/ln2 > \hbar/\Gamma_j^*$. Value of the Γ_j^* is defined as the emission width of the decaying ejectile and is calculated in the same way as for the ground state, i.e. by the formula 3.2. The total emission width of an ejectile is summed over its ground state and all its excited states.

A Monte Carlo simulation is done and an ejectile j is selected according to the probability expressed in eq. 3.1. Type and kinetic energy of an emitted particle are randomly selected according to the probability distribution. A simulation continues as far as evaporation is energetically possible.

The quality of the theoretical model predictions of GEM model used together with intranuclear cascade calculations for the fast step of the proton - nucleus collisions is illustrated by the

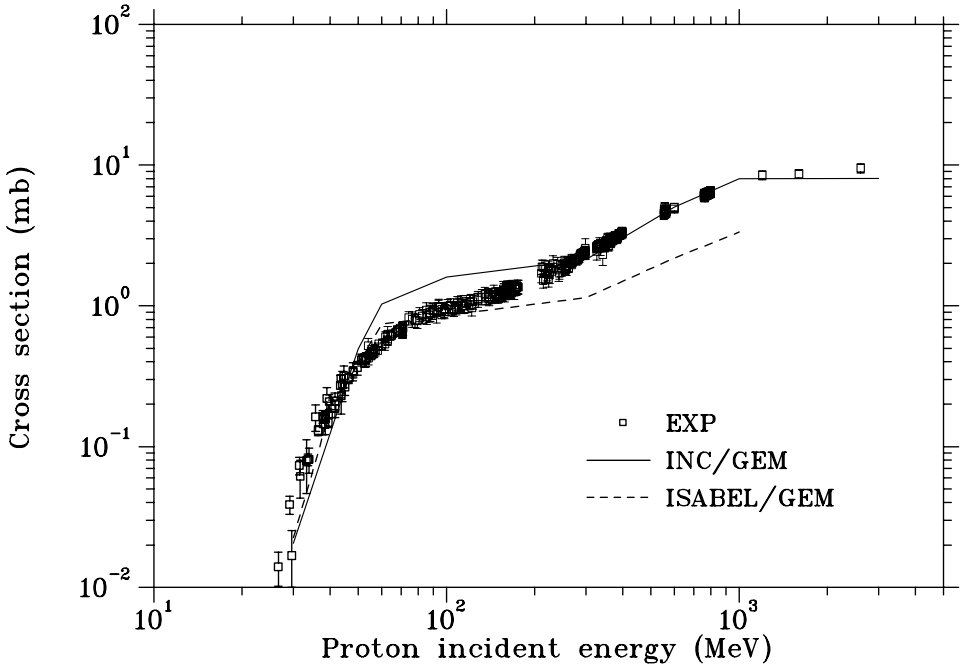

Figure 3.3: The symbols show the experimental production cross sections of the ^{7}Be ejectiles in p+^{27}Al collisions. The dashed line represents calculations performed with combination of ISABEL code for the first stage of reaction and GEM for the second stage whereas the full line shows results of such calculations performed with combination of INC model and GEM. The figure is taken from S. Furihata [47].

Fig. 3.3 where excitation function for the ^{27}Al+p $\rightarrow$^{7}Be + X reaction is shown. Very good overall agreement is visible in full studied energy range, i.e. from the energy threshold of the reaction up to 3 GeV proton beam energy.

It is conjectured, that comparison of the experimental data obtained in the present work with the calculations of INC model plus GEM will shed more light on the mechanism of the reaction. Good reproduction of data of these reactions which fulfill the assumptions of the above models should allow to claim that the assumptions are not fulfilled when the agreement of the calculations with the data is poor.

3.3 Fisher's droplet model of fragmentation

Fisher's condensation theory [50] predicts that the transition from a liquid to a gas proceeds via the formation of droplets whose size distribution follows a power law at the critical transition point. The atomic nucleus, which is treated as a liquid when it is in the ground state, may emit – during heating – light particles and IMFs which behave like a gas or, more exactly, as a mixture of the gas and the liquid – a fog. Following the droplet model, the increase in excitation energy

would generate instabilities in nuclear matter and would lead, at some critical temperature T_c , to the disassembly of the system, into smaller pieces of all sizes which can be experimentally detected.

According to the Fisher's model the yield of the fragments built of A_f nucleons, emitted from the nucleus at the temperature T is described by the formula:

$$Y(A_f) \sim A_f^{-\tau} f(A_f, T) \tag{3.3}$$

where the factor f(A_f,T) is independent of A_f at the critical temperature T_c. The power law dependence Y(A_f) $\sim A_f^{-\tau}$ is then an exact description of the mass yield. The mass yields at temperatures close to the critical point have the shape similar to the power law, therefore it is possible to parametrize them by this simple formula. However, the ***apparent*** power exponent fitted to the data will be dependent on the temperature: $\tau = \tau(T)$ to compensate the hidden variation of f(A_f,T) versus A_f.

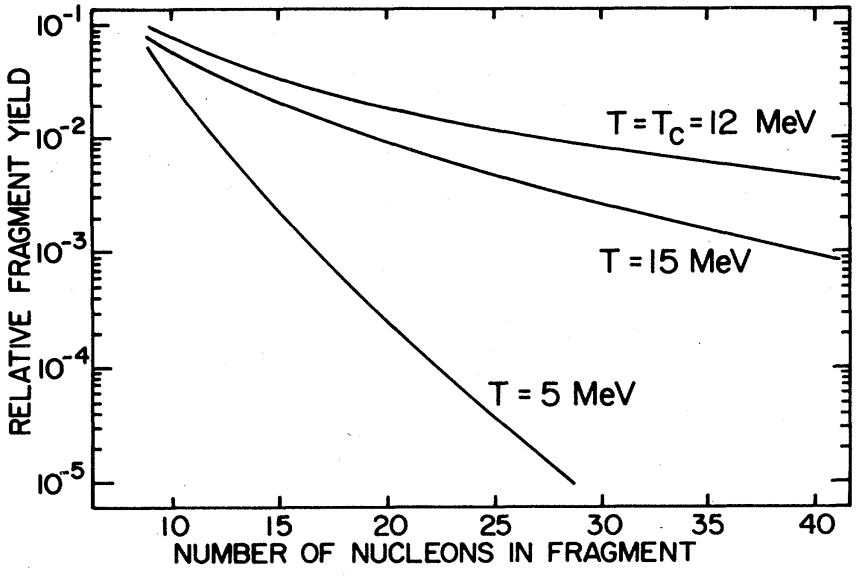

Figure 3.4: Variation of the shape of the mass yields dependence in the vicinity of critical temperature T_c. The figure is taken from paper of Panagiotou et al. [64] .

The power exponent obtained from the fit of the simple power law formula Y(A_f) $\sim A_f^{-\tau}$ to the experimental mass yield has the smallest value at the critical temperature and increases when temperature deviates from this value. The mass yields distributions are most flat at critical temperature whereas their fall off is steeper for temperatures different from the critical one. This is illustrated by Fig. 3.4 taken from Panagiotou et al. [64].

The above behaviour of the mass yield of the IMFs emitted from nuclear reactions can be derived from description of a gas of noninteracting clusters in thermal equilibrium, which has been given by Fisher in his droplet model [50]. The number of clusters per unit volume containing A_f constituents depends on the Helmholtz free energy of the cluster, f_{A_f}, the chemical potential per

particle, μ, and the temperature, T, as

$$\rho_{A_f} = \rho_o * A_f^{-\tau} exp[-(f_{A_f} - \mu * A_f)\beta], \tag{3.4}$$

where $\beta = 1/k_B T$. The free energy contains contributions from both the volume and surface free energy of the droplets. Separating the bulk (volume) and surface terms, we can write (3.4) as

$$\rho_{A_f} = \rho_o * A_f^{-\tau} X^{A_f^{\sigma}} Y^{A_f} \tag{3.5}$$

where X arises from the surface free energy of the droplet:

$$X = exp[-a_s(T)/T], \tag{3.6}$$

and where Y contains the volume free energy and the chemical potential:

$$Y = exp\{-[a_v(T) - \mu(T)]/T\} \tag{3.7}$$

with (3.5) and (3.6,3.7), we obtain the following three forms:

$$\rho_{A_f} = \rho_o \cdot A_f^{-\tau} \cdot X^{A_f^{\sigma}} \quad for \ T < T_c \tag{3.8}$$

$$\rho_{A_f} = \rho_o \cdot A_f^{-\tau} \qquad for \ T = T_c \tag{3.9}$$

$$\rho_{A_f} = \rho_o \cdot A_f^{-\tau} \cdot Y^{A_f} \quad for \ T > T_c \tag{3.10}$$

The critical point, $T = T_c$, $\rho = \rho_c$, occurs when X=Y=1. Below the critical point, $X < 1$ and $Y > 0$. The liquid-gas coexistence curve corresponds to Y=1; when $Y > 1$ the vapor is supersatured. The temperature dependence in eq. (3.5) is contained in X and Y. The parameter ρ_o gives an overall normalization; τ and σ are critical exponents.

The described at beginning of this section behaviour of the distribution of masses in vicinity of the critical point is more quantitatively determined by the (3.8) – (3.10) equations. It should be noticed that apparent exponent τ from eq. (3.3) effectively simulates temperature (energy) dependence contained explicitly in terms X and Y, thus it is different from the parameter τ present in the last equations.

In the papers [44] and [65] a generalization of the formulae discussed above is done for two types of particles forming "gas", i.e. the protons and the neutrons. This two component generalization allows to find yield of emitted fragments as function of their atomic number Z and mass number A. Thus it gives prescription for evaluation of isotopic yields.

The generalization consists in replacing the term containing the chemical potential of nucleons by chemical potentials of neutrons and protons and the term responsible for entropy of mixing:

$$\mu\beta A_f \rightarrow (\mu_N N_f + \mu_Z Z_F)\beta + \left\{ N_f ln\frac{N_f}{A_f} + Z_f ln\frac{Z_f}{A_f} \right\} \tag{3.11}$$

and replacing the Helmholtz free energy f_{A_f} by Weizsäcker - like formula but with modified values of the coefficients which takes into account both the binding energy and the entropy of the cluster of Z_f protons and N_f neutrons:

$$f_{A_f} \rightarrow f(Z_f, A_f) = a_v A_f - a_s A_f^{2/3} - a_c Z_f^2 / A_f^{1/3} - a_a (A_f - 2Z_f)^2 / A_f - \delta \tag{3.12}$$

The a_v, a_s, a_c, a_a, *and* δ are the parameters responsible for the volume, surface, Coulomb, symmetry, and pairing contributions to the free energy.

Resulting formula, listed below reproduces for p+Kr and p+Xe reactions very well yields of about 60 isotopes for each target with single set of parameters [65] :

$$Y(Z_f,A_f) = const \cdot A_f^{-\tau} exp\left\{ [f(A_f,Z_f) + \mu_N N_f + \mu_Z Z_F]\beta + N_f ln\frac{N_f}{A_f} + Z_f ln\frac{Z_f}{A_f} \right\}. \quad (3.13)$$

The discussed extension of the Fisher's droplet model leads to the conclusion that above and below the critical temperature the isotopic yield $Y(Z_f,A_f)$ would be exponentially damped relative to the yield observed at critical temperature T_c.

3.4 Moving source model

A significant number of authors [32, 66, 67] uses a phenomenological model called moving source model in order to fit the energy spectra of fragments emitted in the reaction p+A by high energy of protons. This phenomenological model applies the Maxwell-Boltzmann distribution to describe energy dependence of the cross section and assumes the isotropic emission of the particles in the frame connected with the emitting source. As shown by Westfall et al. [32], the single Maxwell-Boltzmann distribution cannot describe the totality of the energy spectra because frequently two components are observed: a low velocity, low temperature component and a high velocity, high temperature component. Therefore, the energy spectra are usually fitted by the sum of two Maxwell- Boltzmann distributions, however, in ref. [68], Fields suggested that the emission of IMF's is a much more complicated process involving a continuum of "sources" ranging from the quasielastic regime to the compound nucleus. In our case the moving sources model is restricted to two sources which is enough to describe the shape of the energy spectra of fragments as will be shown in the chapter 7.

The energy distribution of fragments emitted at the angle θ_{lab} from the moving source is described by the following parameterization [32, 67]:

$$\frac{d\sigma}{dEd\Omega}(E,\theta_{lab}) = \sqrt{\frac{E}{E'}}\frac{\nu\sigma}{2(\pi\tau)^{3/2}}(\nu E' - kB)^{1/2} e^{\frac{-(\nu E'-kB)}{\tau}}, \quad (3.14)$$

where E and E' denote fragment energy in the laboratory frame and in the frame of the moving source – respectively, B is the nominal Coulomb barrier between the emitted fragment and the rest of the emitting source (Coulomb energy of two charged touching spheres of radii $R_i = 1.44A_i^{1/3}, i = 1,2$), σ is the energy and angle integrated cross section of the fragment emission, and τ is the temperature of the source. The ν and k are correction factors responsible for recoil of the emitting source and deviation of the Coulomb barrier from its nominal height. The E and E' energies are connected by the formula

$$E' = E + \frac{1}{2}m\beta^2 - \beta(2mE)^{1/2} cos\ \theta_{lab} \quad (3.15)$$

in which velocity β of the source in respect to the laboratory frame and emission angle of the fragment θ_{lab} appear as well as the fragment mass m.

The equation (3.14) represents contribution of one moving source to the observed yield of the fragments. It allows to describe energy and angular distribution of emitted fragments and, furthermore, to extract physical information on the reaction from values of the parameters: σ - cross section for emission of the observed fragments, β - velocity of the emitting source, τ - temperature of the source, and k - fraction of the nominal Coulomb barrier. This last parameter

appears due to the fact that the smearing of the Coulomb barrier may be expected because of the variety of charge and mass values of the emitting sources created during proton - nucleus collision whereas the nominal Coulomb barrier is calculated for selected source, e.g. that predicted by the model of the intranuclear cascade for the first stage of the collision.

It should be emphasized that the equation (3.14) has been derived under several assumptions which not necessarily have to be fulfilled. There are: (i) isotropic emission of the fragments which corresponds to the loss of the memory of the emitting source on the mechanism of its creation, (ii) the Maxwell-Boltzmann shape of the energy spectra - typical for equilibrated system with parameter τ characterizing the temperature of the source, (iii) two-body kinematics of the break up of the source used for recoil correction $\nu = \frac{A_{eff}}{A_{eff}-A}$ where A_{eff} and A are the mass numbers of the source and the emitted fragment, respectively. Thus, achieving good reproduction of the observed spectra may be treated as implicit confirmation of validity of the made assumptions. Furthermore, agreement of the parameterized spectra with the double differential cross sections measured at several scattering angles allows to extract the total (angle and energy integrated) cross section σ without explicit integration over angles and energies. This is quite important because most of the experiments devoted to measurement of the double differential cross sections $d\sigma/d\Omega dE$ is not performed in the 4π - geometry.

Chapter 4

Experiment

The PISA experiment is an internal beam experiment for studies of fragmentation of atomic nuclei by proton beam at the COSY (COoler SYnchrotron) ring (see Fig. 4.1). The goal of this experiment is to measure double differential production cross sections for light charged particles (hydrogen isotopes and helium isotopes) and for Intermediate Mass Fragments (IMF, $2<Z<20$) produced in proton induced reactions with thin targets of different materials (see chapter 4.2.1).

Production cross sections are of great importance for many purposes. In particular, low mass ejectiles and residual nuclei (as hydrogen, helium, lithium isotopes, etc.) are crucial for estimation of damages of target and structure materials used in construction of scientific and technological devices, radiation shieldings, etc. For example, helium produced abundantly can destroy steel or concrete construction by embrittlement, production of other elements can lead to chemical corrosion or radiative damages. Besides technological applications the production cross sections are necessary for testing and validation various models of the reaction mechanism what is condition *sine qua non* understanding of the reaction mechanism.

The efficient application of the nuclear reactions in technological, medical and scientific processes demands that the relevant data for each particle type have to be known from reactions thresholds up to the highest energies involved. Due to large range of relevant targets and the vast amount of product nuclides it will not be possible to measure all the cross sections needed. Thus, one has to rely widely on models and computer codes to calculate the required cross-sections. The demand for good theoretical predictions of production cross sections is not satisfied by the models and codes which are actually available. In this context it is essential that reliable and comprehensive experimental data exist which can serve as benchmarks for code development and validation.

In order to measure cross sections and double differential cross sections it is important to identify particles (A and Z identification) produced in proton induced reaction. This identification is possible using different kinds of detectors and different methods as discussed in section A.2.

4.1 Properties of the internal beam experiment

The scattering chamber and the detection system of the PISA experiment is installed on the internal beam of the cooler synchrotron COSY Juelich, which can deliver proton or deuteron beam (Fig. 4.1). Using of the internal beam gives serious advantages but also put restrictive constraints to the conditions of the experiment:

- The targets used in the internal beam experiment must be very thin (of order of 100 - 500 μg/cm^2) because otherwise the internal beam would be immediately used up. This condition

is also favorable for our purposes, i.e. for studying emission of intermediate mass fragments, because the IMFs are strongly absorbed in the target material. Therefore for the thick target they would be not able to escape from the target and counter experiments would be not possible. Then only activation and/or chemical methods could be applied for determination of the cross sections. However, these techniques do not allow to measure angular and energy dependence of the differential cross sections which are of great interest.

- The constraint of the thin target does not limit possibility to get high luminosity of the experiment because the beam protons can pass through the target many times (up to 10^4 – 10^5 times) before they are absorbed or scattered off the beam. This is in contrast to the external beam facilities, where the proton is lost in the beam dump when no interaction with the target took place. The luminosity of the internal experiment can be, thus, as large as for the external experiment with thick target and very intensive external beam. Combination of the thin target and the internal beam is very fortunate for purposes of the PISA experiment. There are, however, further features of the internal beam experiment which are not so comfortable.

- It is necessary to put detectors in close contact with ultra-high vacuum of the COSY-ring (which has the pressure of order of $\sim 10^{-9}$ mbar). This demands that detectors which can spoil the vacuum of the ring are separated from the scattering chamber with foils which are able to resist the atmospheric pressure. Furthermore, these parts of the detecting system should be separated from the COSY vacuum by the valves which can be automatically closed when the leak of gas is detected. This is, e.g. the case for Bragg curve detectors, which are operating under the pressure of $\sim$ 200 mbar, separated only by thin foil from the COSY vacuum. Of course, this part of the detecting system, which is placed between the entrance foil of the Bragg detector and the foil separating the detector system from the scattering chamber, has to be pumped to the intermediate pressure of order 10^{-5} – 10^{-6} mbar. The high vacuum conditions must be also fulfilled by each part of the detecting system which is in contact with the ultra high vacuum of the COSY ring. For example housings of the silicon detectors or cables used inside the scattering chamber must fulfill very restrictive demands.

- The last but not least constraint, characteristic for the internal beam experiments, is very restricted access time of the investigators to the scattering chamber and the detection system because during performation of other experiments the scattering chamber is a part of the accelerator ring and thus cannot be opened or modified.

The COSY synchrotron ring delivers the circulating proton beam of intensity of about 10^{10} – 10^{11} protons. The available ion sources are a H_2^-, H^-, D^- and H^- polarized ion source. The particles extracted from the ion source and accelerated by the injector cyclotron (JULIC) to energy 45 MeV, pass a thin carbon foil losing their 2 electrons by so called stripping. The H^- and D^- become respectively protons H^+ and D^+ which are then injected into COSY [69]. They circulate in a racetrack consisting of 2 semicircles each 52 m in length, which are connected by 2 straight sections 40 m in length. 260 vacuum pumps ensure that the proton race is only very rarely disturbed by a gas molecule with a vacuum better than 10^{-9} mbar [70, 71].
The accelerated beam circulating in the ring passes the scattering chamber $\sim$ 5*10^5 times per second but it does not interact with the target because its position is vertically lower than position of the target. The beam may be slowly shifted by steerers from below the target on to the target in such a way, that each proton can pass through the target up to 10^5 times having each time a chance to initiate nuclear reaction. Thus the cycle of accelerating and interacting with the target may

take from several seconds to several (or more) minutes depending on the velocity of the vertical shift. This velocity is controlled by COSY team due to back feading of the number of observed reaction events by the monitor detector. Thus, the optimal velocity can be achieved to allow for most efficient data acquisition. In the PISA experiment this cycle lasts typically several minutes.

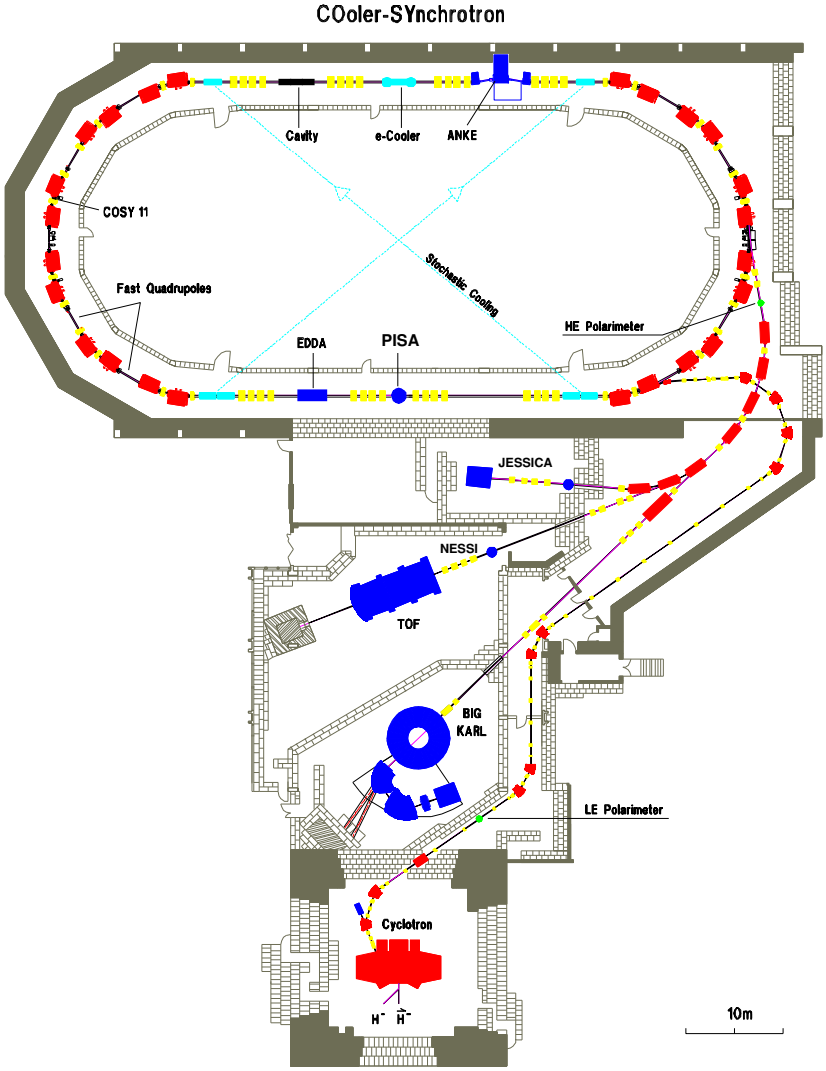

Figure 4.1: View of COSY (COoler SYnchrotron)

4.2 Scattering chamber and detectors

The PISA experimental setup (see Fig. 4.2) is composed of a scattering chamber with 8 detector arms at detection angles 15°, 20°, 35°, 50°, 65°, 80°, 100° and 120°. This setup was used to perform the investigation of reactions induced by protons on thin carbon (20 $\mu g/cm^2$), nickel (400 $\mu g/cm^2$), and gold targets (636 and 260 $\mu g/cm^2$)). The experiment was performed at proton beam energy of 1.9 and 2.5 GeV with the idea to measure the double differential cross-section of produced light and intermediate mass fragments.

In the current thesis, we concentrate on the reaction p(2.5 GeV)+^{197}Au and particles detected by cooled silicon detectors.

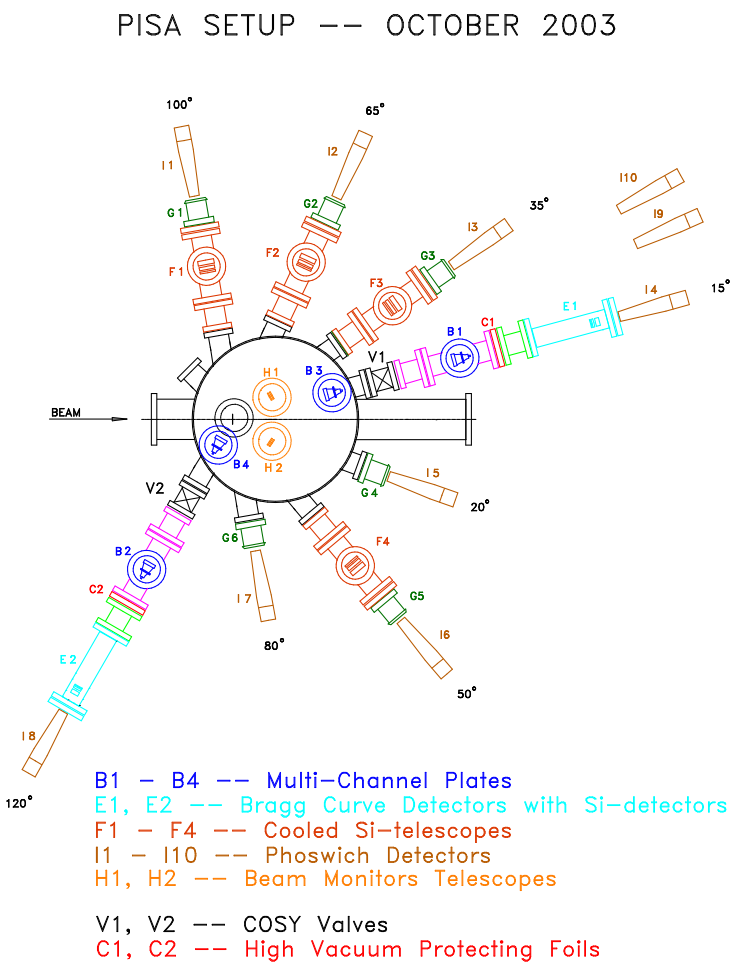

Figure 4.2: Schematic view of PISA setup.

The scattering chamber has a diameter of 65 cm with the target holder shifted 15 cm from

the center of the chamber upstream to the beam direction. This was done to obtain comparable counting rates at different scattering angles.

There are three types of the detector arms: complete arm, cooled silicon telescope arm and phoswich arm. Each kind of detector arm is able to identify charge and mass of emitted particles in various ranges of the particle's energy.

The complete detector arm is composed of:

- two Multi Channel Plates detectors (MCP) serving as the START and the STOP detectors for time-of-flight measurement,
- the Bragg curve detector (BCD) which identifies the charge of IMFs and allows to measure energy of them with very low threshold ($\sim$ 0.5 MeV/nucleon),
- the telescope of three silicon detectors, which identifies charge and the mass (for the lightest particles) of the ejectiles by the ΔE – E method, and
- the phoswich, i.e. the telescope of two scintillator detectors, which also identifies the particles by the ΔE – E method but in the range of higher energies – due to larger thickness of the scintillators than that of the semiconductor detectors.

The cooled silicon telescope consists of:

- three or four silicon detectors cooled to -25^{o} C to improve energy resolution of detectors,
- the phoswich detector as for the complete arm.

The phoswich arm contains only the phoswich detector.

The complete arms are mounted at the most forward detection angle (15^{o}) (see Fig. 4.3) and at the most backward detection angle (120^{o}). The Bragg curve detector provides a possibility to measure low energy part of the spectra of intermediate mass fragments with Z identification up to Z $\sim$ 20. Both Bragg detectors should give almost the same spectra, after correction for the solid angle, since the compound nucleus reactions with approximately isotropic angular distributions dominate at the energies of particles measured by these detectors. The telescopes of semiconductor detectors and scintillators (phoswich), which are placed behind the Bragg detector, observe mainly light charged particles (with Z $\leq$ 2) or high energy tail of the lithium spectra because slow and/or heavy fragments are stopped in the Bragg detector. Combination of the information from time - of - flight telescope of two MCPs and the energy of ejectile from the Bragg detector enables us to identify mass of IMF's with Z in the range of $2 \leq Z \leq 7$ besides their charge.

The Bragg curve detector medium is composed of isobutane gas at pressure of 200 mbar. The active length of the BCD is 20 cm. The minimal energy needed for each kind of particle to cross the complete arm at forward (15^{o}) and at backward (120^{o}) detection angle is shown in table 4.1. The minimal energy for the particle needed to pass through the Bragg detector and enter in the first silicon detector is shown in the second column as E_{Bg}. The energies shown in the four next columns (E_{S1}, E_{S2}, and E_{S3}) are the minimal energies of the particle necessary to cross the first silicon detector and enter in the second (E_{S1}), to cross the second and enter in the third (E_{S2}), and to cross the third and enter in the phoswich detector (E_{S3}), respectively.
The numbers given in table 4.1 are based on calculations performed with SPAR [73] and SRIM [74]. The thickness of isobutane medium of BCD, of all foils (2 mylar foils with thickness: 1.5 μm and 3.5 μm respectively) and the thickness of the silicon detectors have been taken into account in the calculation.

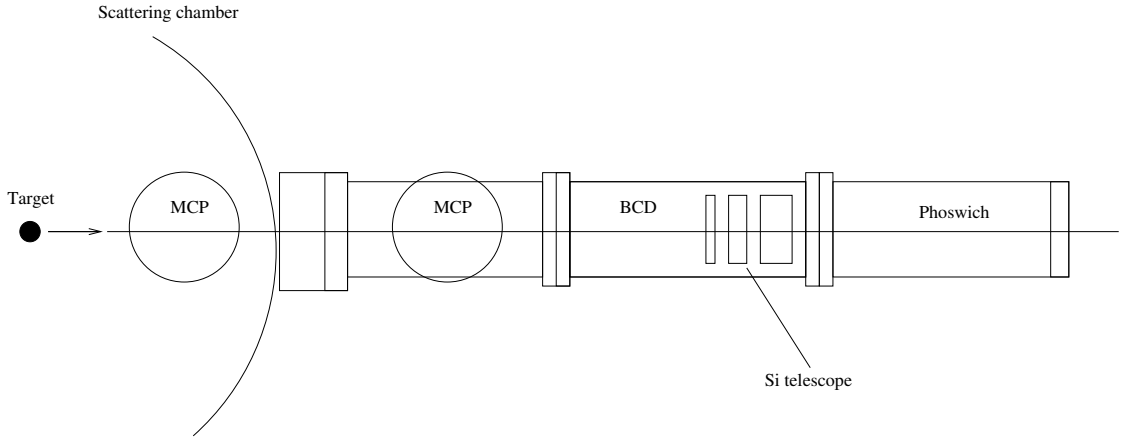

Figure 4.3: Schematic view of one complete arm.

Particle Type	E_{Bg} [MeV]	E_{S1} [MeV]	E_{S2} [MeV]	E_{S3}(4150 μm) [MeV]	E_{S3}(5150 μm) [MeV]
^{1}H	2.6	5.1	9.9	27.3	30.7
^{3}He	10.3	18.2	35.5	96.5	108.7
^{4}He	11.7	20.5	40.0	109.3	123.2
^{6}He	13.8	24.2	47.7	130.3	147.0
^{6}Li	21.9	38.7	75.5	205.8	232.1
^{7}Li	23.3	41.2	80.5	220.2	248.2
^{7}Be	31.6	57.2	111.6	304.3	342.9
^{9}Be	34.9	63.3	124.5	339.6	382.7
^{10}Be	36.4	66.0	129.8	355.4	400.7
^{10}B	41.5	82.0	165.9	456.0	514.3
^{11}B	43.0	85.0	172.7	475.3	536.1
^{12}C	54.1	107.8	220.1	606.0	683.4

Table 4.1: Minimal energy required for particles to cross the Bragg detector, the first, second and the third silicon detector, respectively. For more detailed information see text.

The second kind of detector arm (see Fig. 4.4) was mounted at four detection angles 35^{o}, 50^{o}, 65^{o}, and 100^{o}. The silicon telescope was cooled to a temperature of -25^{o}C. This low temperature reduces the thermal noise component of the detector output signal and in this way improves the energy resolution of the detector. All telescopes consisted of three silicon detectors, with exception of the telescope at 100^{o} which was composed of four detectors.

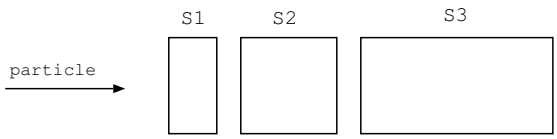

Figure 4.4: Schematic view of a cooled silicon detector telescope.

Telescope name	Detection angle	Thickness [μm]
T1	15^o	150, 500, 4500
T3	35^o	50, 400, 6000
T4	50^o	50, 400, 6000
T5	65^o	50, 400, 5000
T7	100^o	50, 400, 1000, 2000
T8	120^o	150, 500, 3500

Figure 4.5: Characteristic of silicon detectors used in the experiment.

Two monitors were mounted inside the scattering chamber to measure the luminosity. The luminosity L is given by:

$$L = \rho d \frac{\Delta N}{\Delta t} \tag{4.1}$$

where d is the effective length of the beam path within the target, ΔN is the number of beam particles hitting the target, Δt is the considered time interval and ρ is the number of target particles per unit volume defined as:

$$\rho = \frac{N_a \rho_t}{m} \tag{4.2}$$

where N_a is the Avogadro constant, ρ_t the target density and m the atomic mass of the target. Generally the luminosity value is given in $\mathrm{cm}^{-2}\mathrm{s}^{-1}$.

The luminosity was measured by comparison of the measured number of scattered protons on the protons to the known proton-proton elastic scattering cross section. The cross section of the proton-proton elastic scattering was measured for different energies and scattering angles by the EDDA [75] experiment. In the PISA experiment we heave used a polyethylene target in order to observe proton-proton elastic scattering reaction because polyethylene is composed of carbon atoms and hydrogen atoms. Then additionally scattering on the carbon target was necessary and continuous monitoring of relative intensity of the emitted particles (protons or δ-electrons).

The relation between the luminosity and the cross section is defined as:

$$\frac{\Delta N_{scat}}{\Delta t} = L \cdot \sigma \tag{4.3}$$

where L is defined in equation (4.1) and ΔN_{scat} is the number of protons scattered in the time interval Δt. With the help of monitor detectors mounted inside the scattering chamber the number of scattered protons is registered and analyzed.

4.2.1 Choice and properties of the target

Generally proton induced reaction experiments use two types of target: thin target (less than $1\mathrm{mg/cm}^2$) [26] used for example to measure proton induced fission and spallation products and thick target [76] used to measure neutron production and total or inelastic cross sections.
The targets used in the PISA experiment are thin targets. Such thin targets allow fission and spallation products to recoil out of the target with minimal energy loss and minimal scattering.
Some calculations were done to define a reasonable target thickness but nevertheless very thin targets can not be manufactured due to the limitation in the production technique.
The choice of gold target was taken because it is a remarkable metal with the advantageous combination of chemical and physical properties. These properties include:

- resistance to corrosion: Gold is the most non-reactive of all metals. Gold is uneffected by air, water, alkalis and acids, with the exception of “aqua regia”, HNO3/HCl. It will not rust or tarnish.
- ductility and malleability: Gold is the most ductile of all metals, allowing it to be drawn out into tiny wires or threads without breaking. It can be shaped or extended into extraordinarily thin sheets due to its malleability.

In the PISA beam time three different target materials and two different geometries were used, targets for beam adjustment and target for measurement (see Fig. 4.6). The target characteristics are given in Table 4.2. The target thicknesses were measured by energy-loss measurement of α particles from ^{252}Cf source but also by weighting.

The strip target material was produced by evaporation method in the Institut f*ü*r Strahlen- und Kernphysik in the University of Bonn. The evaporation of the material takes place in a vacuum chamber. The source material placed inside the vacuum chamber is heated to the point where it starts to boil and evaporate. The vacuum is required to allow the molecules to evaporate freely in the chamber, and they subsequently condense on all surfaces. There are two evaporation technologies, which are electron beam evaporation and resistive evaporation. In electron beam evaporation, an electron beam is aimed at the source material causing local heating and evaporation. In resistive evaporation, used in Bonn, the source material is heated electrically with a high current to make the material evaporate.

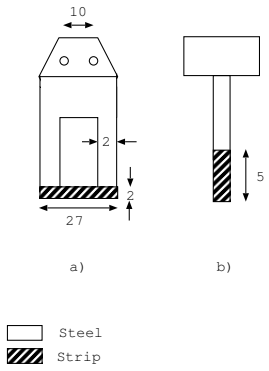

Figure 4.6: Schematical drawing of target used during the experiment: a) target for measurement, b) target for beam adjustment.

The PISA targets are not standard. For example a new technique was developed by the Bonn University to produce Nickel foils.
Nickel foils were produced by evaporation with a sandwich structure nickel on copper.
The target is manufactured in three step. First, a part of the material (nickel on copper) is cut with dimension 2x30 mm. This piece is placed on the surface of a solution called Richard solution. This solution contains trichloroacetic solution 20% and ammoniac solution 25%. The blue color appearing in the Richard solution is a signature of the copper being dissolved. In the second step, the piece of material contains only nickel which is carefully taken out using a piece of glass and is carefully placed on the surface of the next solution containing water and isopropanol. The last manipulation is the most difficult. This manipulation consists of taking the nickel piece on the

target frame. This piece must be parallel to the frame and the piece surface must be uniform. If the strip is rolled up then the thickness is not known and the target stability is not sure. The strip is stuck in two points and on these two points a silver conductive glue is deposited in order to obtain an electric contact between the nickel strip and the target frame. This conductive glue is needed because the target must be not charged.

Target material	Width $[mm]$	Length $[mm]$	Thickness $[\mu g/cm^2]$
Ni	2	27	398 ± 20
C	3	27	20 ± 1
Au	2	27	636 ± 32
Au	3	27	260 ± 13

Table 4.2: Target characteristic parameters.

For the first adjustment of the beam at the target, we use a carbon strip with the dimension 5x2 mm^2. In this thesis, we focus on the Au targets except for normalization and luminosity measurement needed.

4.2.2 Silicon detector telescopes

In the recent setup three kind of detectors were used: gaseous detectors (BCD), semiconductor detectors (Si), multichannel plates and plastic scintillators (phoswich).
The semiconductor detectors used in the experiment are surface-barrier silicon detectors and lithium-drifted silicon detectors (Si(Li)).
Surface-barrier silicon detectors are made of crystal of silicon (N-type) and gold layer has been deposited on (as an electrical contact). Generally surface-barrier detectors are made from different group semiconductor compounds. The properties of crystal of silicon are shown in the table 4.3.

	Si
Atomic number	14
Atomic weight	28.09
Density (g cm^{-3})	2.33
Crystal structure	Diamond type
Dielectric constant	12
Forbidden energy gap (300^oK in eV)	1.115
Forbidden energy gap (0^oK in eV)	1.165
Intrinsic carrier density (300^oK in cm^{-3})	$1.5*10^{10}$
Intrinsic resistivity (300^oK in Ω cm)	$2.3*10^{10}$
Electron mobility (300^oK in $cm^2V^{-1}s^{-1}$)	1350
Hole mobility (300^oK in $cm^2V^{-1}s^{-1}$)	480
Electron mobility (77^oK in $cm^2V^{-1}s^{-1}$)	$2.1*10^4$
Hole mobility (77^oK in $cm^2V^{-1}s^{-1}$)	$1.1*10^4$
Energy per hole-electron pair (300^oK in eV)	3.62
Energy per hole-electron pair (77^oK in eV)	3.76

Table 4.3: Basic properties of silicon crystal.

Assuming that the crystal is perfect, when the charged particle passes through the crystal, the

formation of electron-hole pairs occurs. The electrons from the top of the valence band are excited to the bottom of the conduction band (see Fig. 4.7), leaving behind a hole in the valence band. This behavior is only valid by equal equilibrium concentrations of free electrons and holes where:

$$n_i = T^{3/2} exp(-E_g/2kT) \tag{4.4}$$

is the formula of the number of electrons in the conduction band, where T is the temperature, k the Boltzmann constant and E_g the forbidden energy gap.
Perfect crystals do not exist and each crystal contains imperfections which can influence the electrical properties of the semiconductor. These imperfections can be the chemical impurities and structural defects. If chemical impurities are localized in the crystal lattice, two kind of levels exist: donor levels and acceptor levels (see Fig. 4.7).
Donor levels are characterized by a level near the conduction band and by giving an electron to the conduction band and acceptor levels are characterized by a level near the valence band and by generating a hole in the valence band. These levels are localized in the forbidden energy gap and semiconductor which contain such levels are called extrinsic.
The only way to obtain an equal equilibrium concentration of electrons and holes is when donors and acceptors are introduced in a crystal lattice and particularly in the case of a large energy gap or at low temperature.

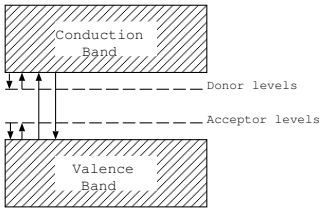

Figure 4.7: Energy band diagram.

A crystal with an excess of electrons is called N-type material or respectively with an excess of holes is called P-type material.
When a metal and a semiconductor N-type are brought into contact, a contact appears between the two materials. This contact is equal $V_o = (E_{F2} - E_{F1})/q$ where E_{F1} and E_{F2} are the Fermi levels and depend on the energy required to liberate electrons in the two materials. Therefore, a depletion layer without free carriers is formed in the semiconductor.
Similarly for the p-n junction, where the silicon crystal is a N-type material and generation of a P-type layer by etching the surface by a material layer (gold), between the two types of material a double layer of charges is formed. The electrons from the N-type material migrate into the P-type material and holes from the P-type material migrate into the N-type material. When this diffusion process is done in the same time, the electrons formed donor impurities, and the holes leave acceptor impurities. The effect of this migration is a surplus of positive space charge in the N-type material and of negative space charge in the P-type material. An equilibrium is reached when the Fermi level E_F, is constant throughout the material. At equilibrium, an electric field pushes back free electrons into the N-type zone and holes into the P-type zone, such that the layer over this charge equilibrium try to be acquired is depleted of free charge carriers and this layer is called depletion layer. The diffusion current is then compensated by the current of the minority carriers.
When a negative potential U is applied to the P-type side (called reverse bias voltage), the current from the minority carriers is very small and changes very slightly with the applied voltage and

under these conditions are operate silicon detectors. Since the resistivity of the depletion layer is much higher than the one of the remaining parts of the junction material, virtually all the reverse bias voltage is present across the depletion layer, thus increasing greatly the electric field there. This field can be calculated in order to see if it is sufficient to separate a large part of electrons and holes produced when a incident radiation appears and to collect the electrons on the anode before they recombine with the holes. This field E is defined as :

$$E = \sqrt{\frac{2eN_aU}{\varepsilon_o\varepsilon}} = \frac{2U}{d} \tag{4.5}$$

where eN_a is the charge density of acceptor impurities and d the total depth of depletion layer. The collection time is also important because it must be faster than the recombination time of electrons and holes and is given by:

$$t_c = \frac{d}{\mu E} \tag{4.6}$$

For p-n junction detector and surface barrier detectors the thickness d of the depletion layer increases with the reverse bias voltage U, but the thickness is limited to less than 2 mm. If thicker depletion layers are required then it is better to use lithium-drifted detectors.

A thicker depletion layers is achieved by producing in the semiconductor crystal a layer with impurities almost completely compensated by ions of the other electron affinity. In the case of lithium-drifted silicon detectors, crystal lithium ions (donor impurities) are diffused into the silicon crystal, thus forming a N-type layer. The lithium ions move slowly into the P-type zone and are able to compensate completely the remaining impurities there. With this compensation method, it is possible to obtain a very high resistivity, for example $3*10^5\,\Omega$ cm for silicon.

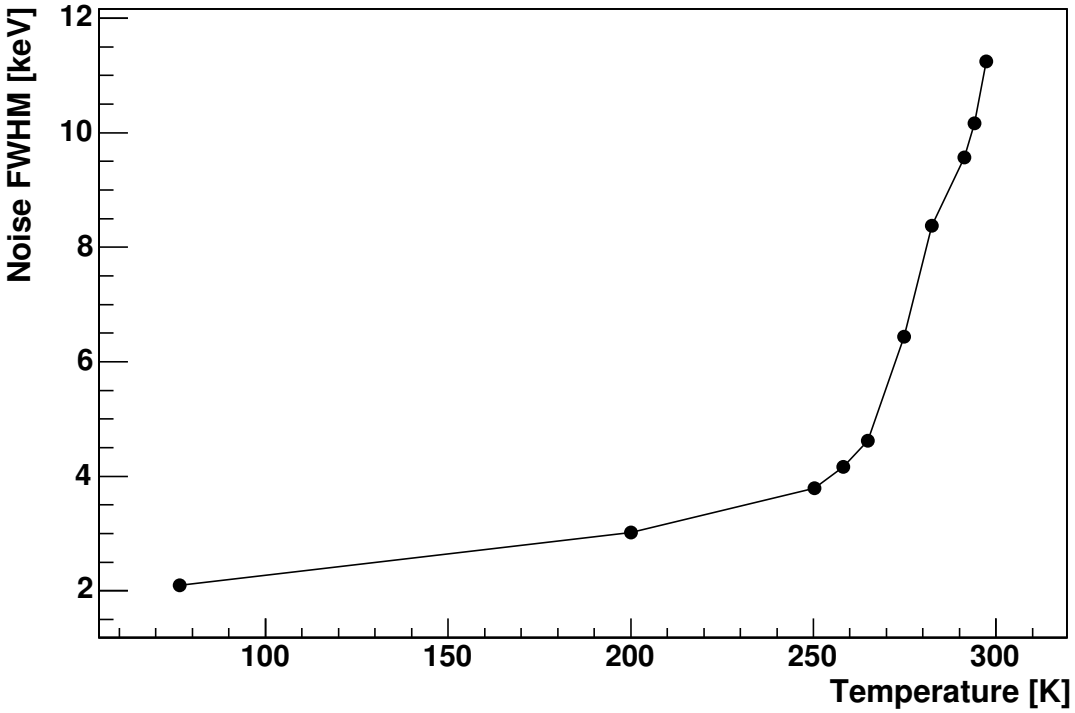

Figure 4.8: Noise contribution versus temperature of a silicon surface-barrier detector where FWHM is the Full Width of Half Maximum (after Walter et al. [78]).

Lithium-drifted detectors are characterized by a high detection efficiency and a linear energy response even for very deeply penetrating particles. However, for detection of low energy heavy particles it is more advantageous to use surface barrier detectors which have generally a smaller noise [77]. Factors like incomplete charge collection and electronic noise deteriorate the detection efficiency and can be minimized by cooling the detectors (see Fig. 4.8). For surface barrier detectors it is only necessary to cool to -25^{o} because this temperature is sufficiently low to reduce the noise considerably.

In the two complete arms mounted at 15 and 120^{o} (see Fig. 4.3) the BCD is followed by three silicon detectors (see Fig. 4.9) of 150, 500 and 4500/3500 μm thickness for particle identification using ΔE-E techniques. These three silicon detectors are mounted in the gas volume (isobutane at 200 mbar) inside the BCD housing. The choice of ΔE and E detector thicknesses is dictated by the ranges of the ions to be measured. Due to the fact that BCD stopped the most of the intermediate mass fragments only light charged particles and a few light fragments are observed.

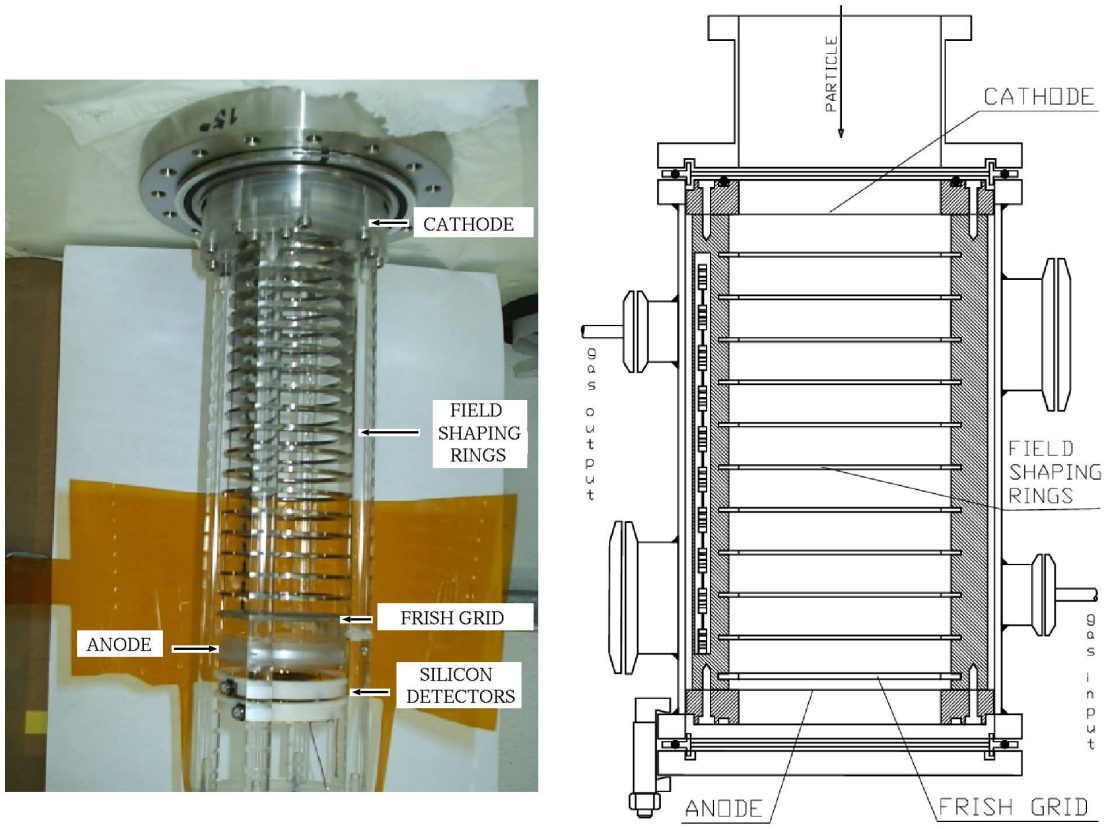

Figure 4.9: Photo of Bragg Curve Detector followed by silicon detectors (left picture) and its schematic view (right picture).

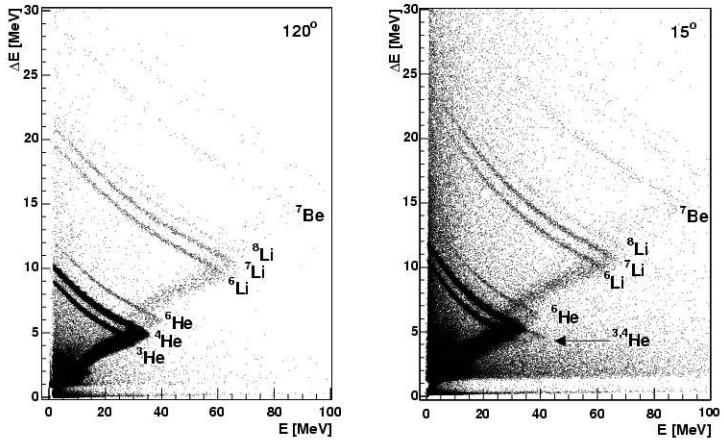

Figure 4.10: Mass identification spectrum of the first pairs of silicon detectors at 120° and 15° (with thickness 150 μm for the first silicon detector and 500 μm for the second one) in the respect to the proton beam direction in the reaction p(2.5 GeV)+^{197}Au.

Nevertheless, the spectrum obtained from these silicon detectors via the ΔE-E technique (section A.2) shows a mass identification of all fragments from helium to beryllium as shown in Fig. 4.10

for reaction p+^{197}Au at 2.5 GeV at 120^o and 15^o in the respect to the proton beam direction. As can be seen in Fig. 4.10, more particles are produced at 15^o than at 120^o, especially heavier particles like ^{6}Li, ^{7}Li and ^{7}Be.

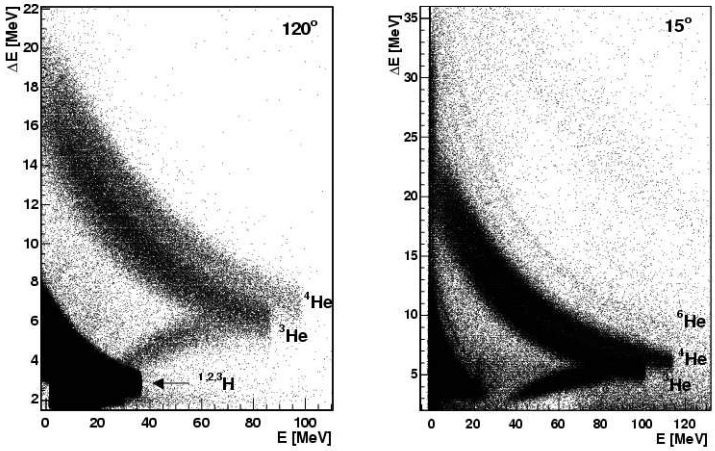

Figure 4.11: Mass identification spectrum of the second pairs of silicon detectors at 120^o and 15^o (with thickness 500μm for the first silicon detector and 3500 (120^o) and 4500 μm (15^o) for the second one) in the respect to the proton beam in the reaction p(2.5 GeV)+^{197}Au.

4.2.3 Cooled silicon telescopes

Silicon detector telescopes are mounted in the arm at 35^o, 50^o, 65^o and 100^o. Each telescope contains 3 silicons detectors (see table 4.4) operating in ultra-high vacuum.

Si Name	Angle [deg]	Thickness [μm]	Type
S103		50	surface barrier
S203	35	400	surface barrier
S303		6000	lithium drifted silicon
S104		50	surface barrier
S204	50	400	surface barrier
S304		6000	lithium drifted silicon
S105		50	surface barrier
S205	65	400	surface barrier
S305		5000	lithium drifted silicon
S107		50	surface barrier
S207	100	400	surface barrier
S307		1000	lithium drifted silicon
S407		2000	lithium drifted silicon

Table 4.4: Description of cooled silicon telescopes used in the experiment in May 2004.

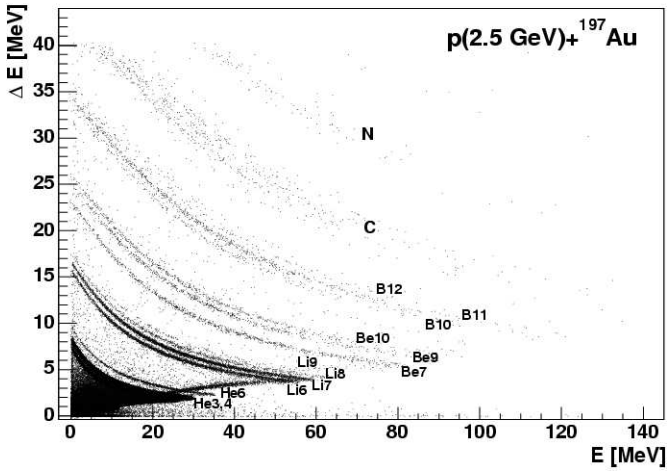

Figure 4.12: Mass identification spectrum of ejectiles emitted in the reaction p(2.5 GeV)+^{197}Au at 35^{o} in respect to the proton beam direction. Energy loss in the first silicon detector (50 μm) is plotted vs energy loss in the second silicon detector (400 μm) of the cooled silicon telescope.

These two telescopes were cooled down to -25^{o} C and used for isotope identification.

Excellent mass identification for all measured fragments up to N was obtained from the cooled silicon detector telescope at 35^{o} for the first pair of detectors (see Fig. 4.12).

The separation of Be isotopes and B isotopes is clearly visible. Cooled telescopes provide a better isotope separation than in the case of silicons detectors telescopes operated at room temperature.

The energy resolution is 0.5 % in the case where the detectors are cooled. At room temperature the energy resolution is 0.8 %.

When silicon detectors are cooled effects like ”pulse-height defect” and ”plasma delay” are minimized [79].

4.2.4 Bragg Curve Detector

The Bragg Curve Detector (BCD) is a gaseous detector used to identify particles by ionization [72, 80, 81] also called Bragg Curve Spectroscopy.

Two BCDs are installed in the arm at 15^{o} and 120^{o} detection angle, these two detectors are filled by isobutane gas at a pressure of 200 mbar. There are able to identify elements from Z=2 to Z=14 whereas the isotopes can be separated up to A$\leq$ 20, when the time of flight given by one pair of multichannel-plate detectors is also taken into account.

The Fig. 4.13 shows an identification spectrum of the products of the reaction p+^{58}Ni at proton energy E$_p$=1.9 GeV.

The particle detection energy threshold obtained from BCD is very low and is equal to 0.5 MeV/nucleon which is the particular advantage of the BCD in comparison to the Si-detectors where this threshold can not be so low due to the limited detector minimal thickness.

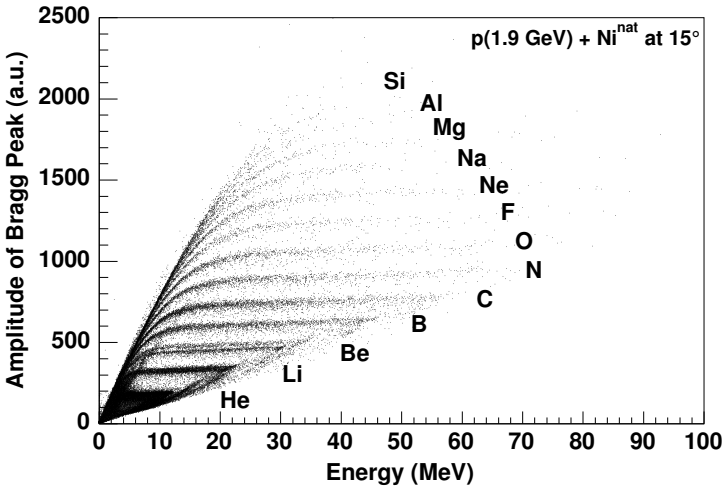

Figure 4.13: Typical identification spectrum of emitted fragments in forward direction (15°) from reaction p(1.9 GeV)+^{58}Ni. The scatter plot of the maximum of the BP versus energy deposited in the Bragg Curve Detector (from [82]).

The detector (cf. Fig. 4.9) is constructed as a cylinder limited by a cathode at the entrance and by an anode spaced from the cathode by 22 cm. The Frisch Grid is placed at a distance of 20 cm from the cathode. The voltage between the Frisch Grid and the cathode is distributed by means of voltage dividers made of high precision 1 MΩ resistors, which is connected to 19 field-shaping rings in order to maintain a homogeneous electric field over the active detector volume.

The particles crossing the region between the cathode and the Frisch Grid creates an ionization track, which reflects the energy loss function (dE/dx) of the particle in the medium, called Bragg Curve (see Fig. 4.14). We can see two different parts: the part from the small energy loss per single collision and the part when the energy remaining is small we observe a peak so called Bragg Peak (BP).

This energy loss is given by the approximated Bethe-Bloch formula :

$$-dE/dx \sim cZ^2/E, \tag{4.7}$$

where Z, E are the atomic number and kinetic energy of the particles crossing the BCD, c is a constant.

The electrons drift through the grid and create a current signal at the anode.

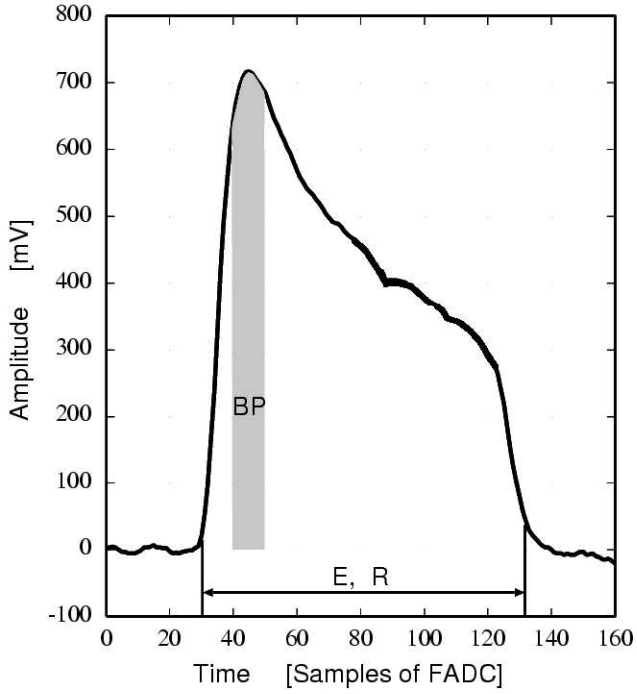

Figure 4.14: A typical output signal from BCD representing the so called Bragg Curve. More description in the text.

The integration of the surface under the Bragg Curve (Fig. 4.14) give the kinetic energy of the particle (E). The maximum of the the Bragg Peak (BP) is proportional to the atomic number Z of the particle. The main parameters of the BCD used in this experiment are given in Table 4.5.

Active length	200 mm
Frisch grid to anode gap	19 mm
Cathode voltage	0 V (grounded)
Frisch grid voltage	+2400 V
Anode voltage	+2900 V
Number of guard rings	19
Cathode(mylar foil thickness)	3.5 μm
Anode(mylar foil thickness)	1.5 μm
Gas	Isobutane
Pressure	100-300 mbar

Table 4.5: Main parameters of the Bragg curve detector.

4.2.5 Multichannel-plate detectors

Multichannel plates are special plates with several million channels used to amplify electron signal. Each channel works as independent electron multiplier. In MCP the electron multiplication takes place inside of the glass wall of channels. The advantages of the MCP in comparison with conventional PMT are better time resolutions and ability to run in magnetic fields.

In PISA experiment, each multichannel-plate (MCP) detector contains 2 multichannel-plates in so called Chevron configuration.

The telescope composed of two MCP detectors, one for the signal ”start” and the second for the signal ”stop”, are mounted at the front of the BCD (at 15^o and 120^o) and are able to measure the time of flight (TOF) of particle.

The ”start” MCP is placed in the scattering chamber in the front of detection arm and the ”stop” MCP is installed inside the arm.

The MCP are manufactured by Galileo Corporation.

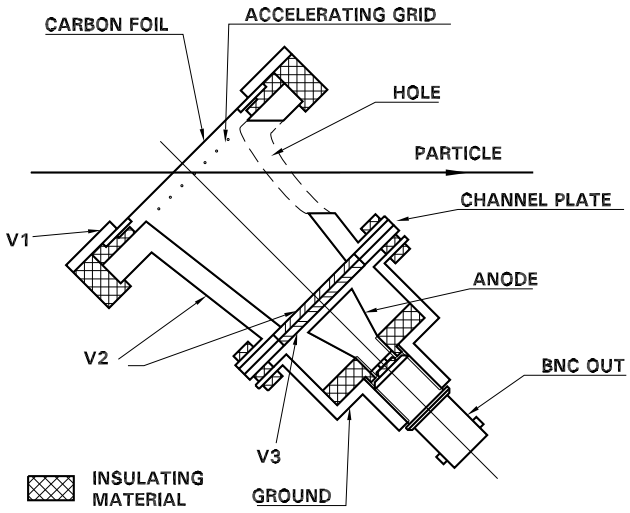

Figure 4.15: Design of one multichannel-plate in the Chevron configuration.

As is shown in the Fig. 4.15, a detected particle passing through the thin carbon foil (20 $\mu g/cm^2$) knock out few δ electrons. Through the hole in the detector housing the particle flies to the next detector. The released electrons enter the channel (holes in a lead glass plate). At the entrance they are accelerated by longitudinal electric field in the direction to the second channel plate by means of the accelerating grid. These electrons can produce secondary electrons by hitting the wall of the channel and these secondary electrons can produce further secondary electrons by next subsequent collisions with channels walls. The coating of the channel wall therefore acts as a continuous dynode.

The multiplication factor is limited by the total space charge per pulse at the exit of the channel. The particular voltages to accelerate the electrons are chosen to obtain the highest multiplication factor in the channel plates (10^7) and to obtain the best ratio signal/noise.

In the Table 4.6 the specific voltages applied in the different parts of the MCP are shown.

A timing resolution of the PISA MCP-telescope is equal to 300 ps. With the combination of the information from the BCD and MCP detectors, the Z identification and time of flight (TOF), the mass identification of the particles and their energy measurement are possible.

Part	Voltage $[V]$
Carbon foil	-3000
Accelerating Grid	-2700
Second Channel plate	-300

Table 4.6: Characteristic voltage for Multichannel-plate detector.

4.3 Construction of detectors

The silicon detectors telescopes used in the arm at 35°, 50°, 65° and 100° contained silicons surface barrier detectors and lithium drifted silicon detectors manufactured by Ortec.
Since detectors have to be installed directly in the ultra high vacuum of the COSY accelerator vacuum system, the special housings for them have been designed. The housing is composed of components proper for ultra high vacuum. The cooling fluid is supplied through the UHV liquid feedthroughs (see Fig. 4.16).

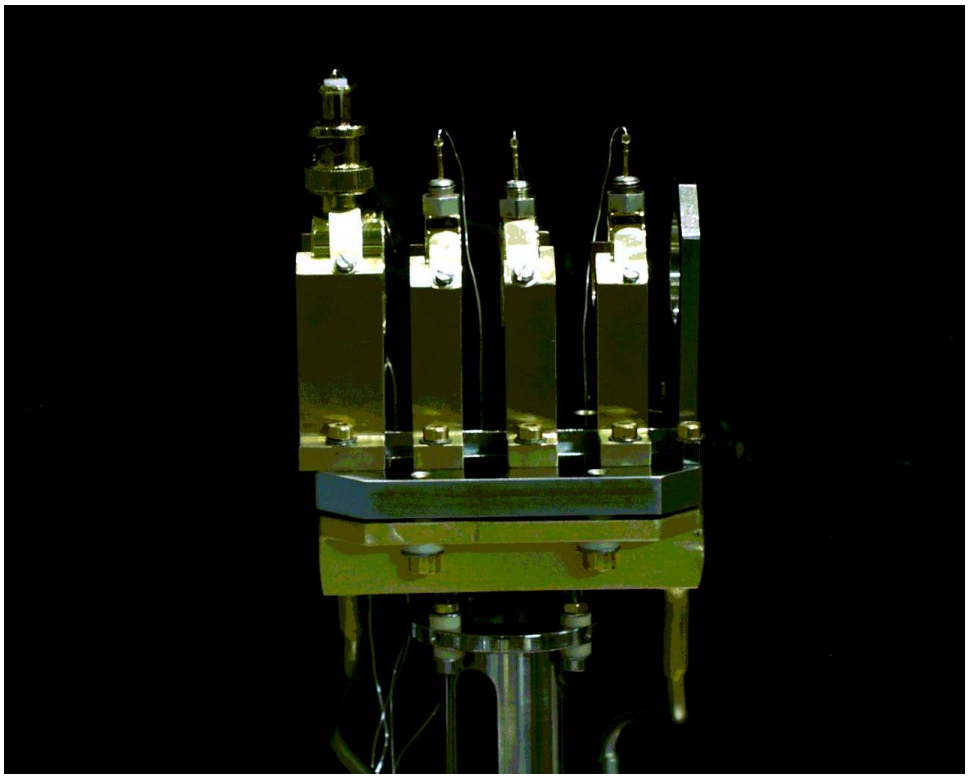

Figure 4.16: Photo of cooled silicon telescope at 100°

4.4 Data Acquisition

The PISA data acquisition system is based on NIM and CAMAC electronic used for signal forming, trigger for signal condition and VME system for signal digitalization.

A schematic view of signal extraction from silicon detector in the PISA DAQ system is shown in the Fig. 4.19. The analog signals from the silicon are preamplified and divided in two parts with different amplification via two amplifiers.A fast logic and analog signal from both ways are produced. The fast signal is connected to discriminator used for logic information (SA,SB). In contrast, the analog signal (SL, SH) responsible for the analog information is connected with a peak sensitive ADC.

The following description of the logic signal is explained for one silicon detector arm. In the same way the signals are treated for all silicon detectors arms.

The first part of an analog signal is high amplified and is concerning only hydrogen and helium isotopes ("SL"- signal light). The second part of an analog signal from the same detector is low amplified for the visualization of all particles from hydrogen up to the oxygen isotopes ("SH"- signal heavy). Two kinds of spectra (see Fig. 4.17) can been produced, one S1H versus S2H which shows all particles detected by the silicon detectors and the second plot S1L versus S2L as a zoom of the plot S1H versus S2H which shows only light charged particles (H isotopes and He isotopes). This last plot gives a better resolution for light particles.

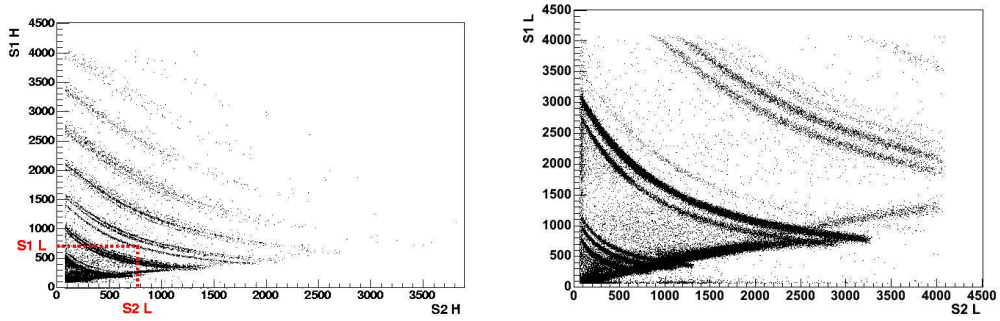

Figure 4.17: The figure shows two kinds of spectra produced during the experiment: S1H versus S2H plot which shows all particles detected by the silicon detectors and S1L versus S2L as a zoom of the plot S1H versus S2H which shows H isotopes and He isotopes with better resolution.

From these 2 fast signals two discriminations levels are established: low level SA and high level SB. The low discrimination level SA is used to cut the noise and the high discrimination level SB is needed to take into account only particles with $Z \geq 3$. The indication if it was a low or a high threshold and from which silicon detectors the signal came was stored by a TDC module. In summary, these thresholds (see Fig. 4.18) are chosen in order to minimalize the electronic noise but also to reduce the number of light charged particles ($Z \leq 2$) by prescaling in comparison to the number of intermediate mass fragments ($Z \geq 3$).

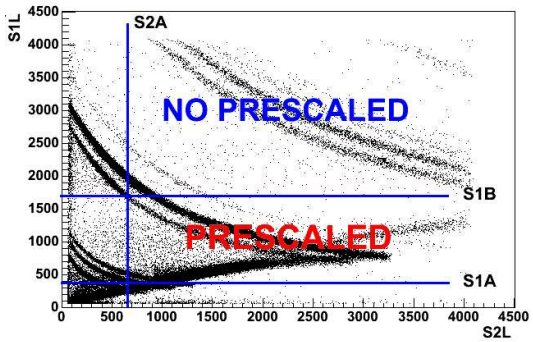

Figure 4.18: Position of the threshold level S1A, S1B and S2A in a ΔE-E spectra. More details in the text.

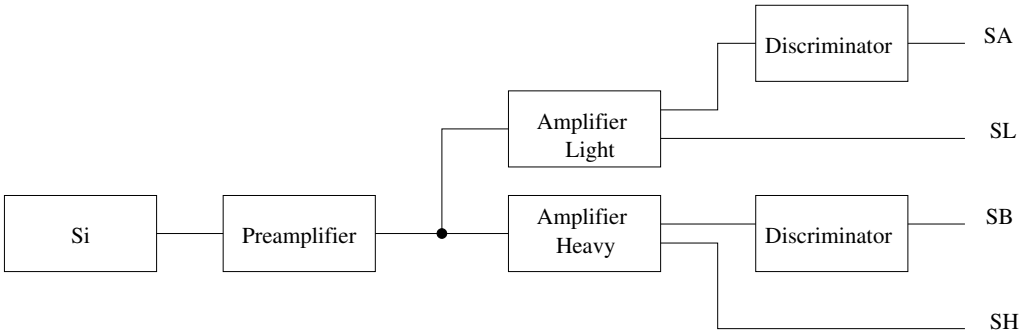

Figure 4.19: Electronic scheme of a silicon detector.

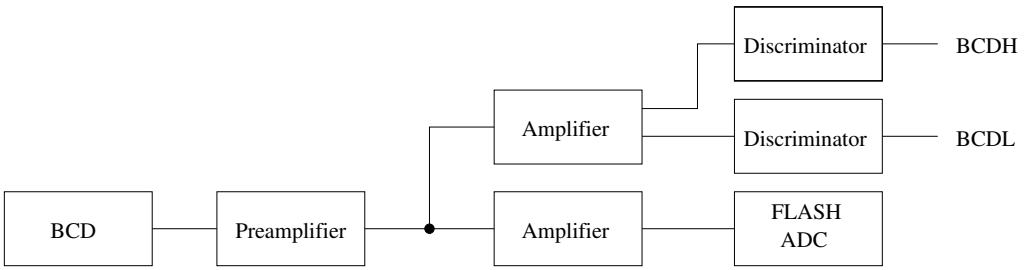

Figure 4.20: Electronic scheme of a Bragg curve detector.

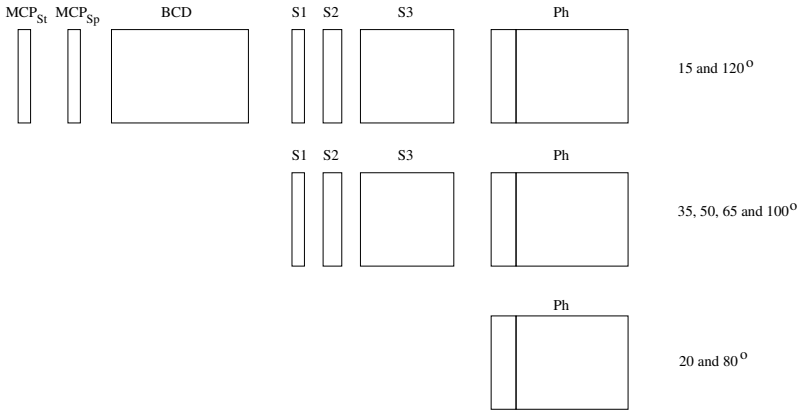

Figure 4.21: Schematic drawing of 3 different detectors arms.

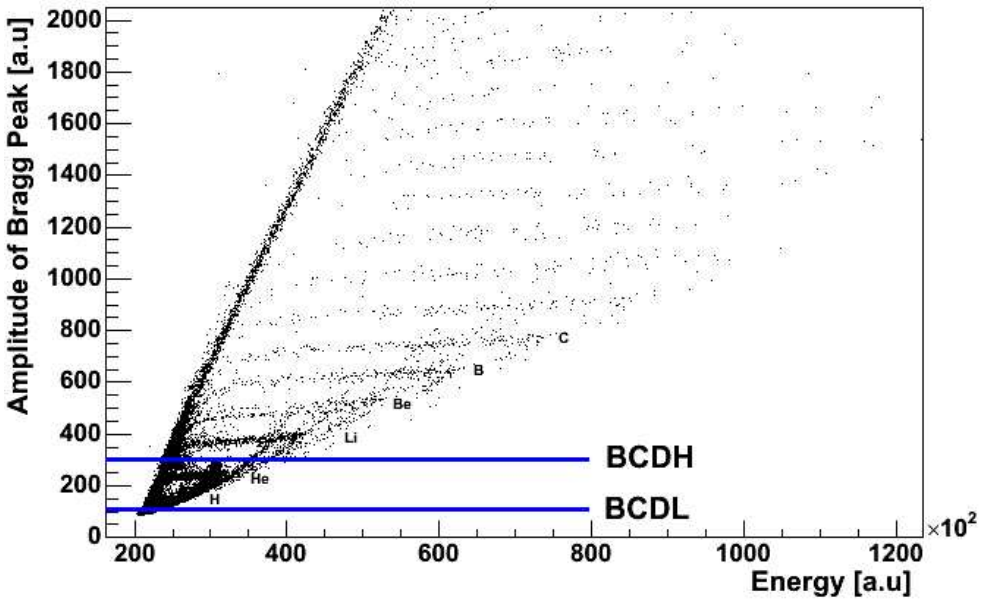

Figure 4.22: Position of the threshold level BCDL and BCDH.

In the PISA experiment 4 triggers were used (see table 4.7). The trigger 1 concerns arms with Bragg Curve detector (placed at 15^{o} and 120^{o} detection angle see Fig. 4.21). This trigger is validated if the multi-channel plates detectors "start" (MCP_{st}) and "stop" (MCP_{sp}) detected a signal in coincidence or a coincidence between adjacent silicon detectors ($S1 \wedge S2$ or $S2 \wedge S3$) existed or coincidence between the third silicon detectors (Si3) and the phoswich (Ph) is present. The trigger logic for trigger 2 is the same as the trigger 1 for silicon detectors telescope and the phoswich detectors mounted at 35^{o}, 50^{o}, 65^{o} and 100^{o} but concerns also the two Bragg curve detectors at 15^{o} ($BCDL_{15^{o}}$ and $BCDH_{15^{o}}$ see Fig. 4.22) and 120^{o} ($BCDL_{120^{o}}$ and $BCDH_{120^{o}}$) detection angle and the coincidence between all available arms (*CoincArm*). A coincidence between two arms means that for example that a coincidence between two MCP in the arm at 15^{o} and a coincidence between two adjacent silicon detectors in the arm at 35^{o} are recorded. A part of this trigger is used in the cooled silicon detectors telescope analysis and will be discuss in details below. Two triggers

(trigger 1 and 2) are necessary to treat the signal recorded in the complete arm mounted at 15^{o} and 120^{o} because the BCD signal is not precisely define in time, up to few μs dependent of particles and the energy. The trigger 3 concerns the coincidence between the second and the third cooled silicon detectors mounted at 35^{o} used as monitor $Si2_{mon35}$ and $Si3_{mon35}$ and are high amplified in order to detect electrons. The trigger 4 is dedicated for scalers readout (1 per second).

TRIGGER 1	$\left(MCP_{st} \wedge MCP_{sp}\right)_{15^{o},120^{o}} \vee \left((S1A \wedge S2A) \vee (S2A \wedge S3A) \vee (S3B \wedge Ph)\right)^{presc}_{15^{o},120^{o}} \vee \left((S1B \wedge S2A) \vee (S2B \wedge S3A)\right)_{15^{o},120^{o}}$
TRIGGER 2	$\left((S1A \wedge S2A) \vee (S2A \wedge S3A) \vee (S3B \wedge Ph)\right)^{presc}_{cooled} \vee \left((S1B \wedge S2A) \vee (S2B \wedge S3A)\right)_{cooled} \vee (BCDL^{presc}_{15^{o}} \vee BCDL^{presc}_{120^{o}} \vee BCDH_{15^{o}} \vee BCDH_{120^{o}}) \vee CoincArm$
TRIGGER 3	$(Si2_{mon35^{o}} \wedge Si3_{mon35^{o}})^{presc}$ (Monitors)
TRIGGER 4	Scalers (1 per second)

Table 4.7: List of triggers used during the experiment. See text for more details.

For the analysis of the data coming from the silicon detectors, the selection in the trigger 2 must be done between the prescaled event and the noprescaled event.
For noprescaled events the selection used is:
$(S1B \wedge S2A) \vee (S3A \wedge S2B)$;
and for prescaled events:
$\left(\overline{(S1B \wedge S2A) \vee (S3A \wedge S2B)}\right) \wedge \left((S1A \wedge S2A) \vee (S2A \wedge S3A)\right)$
For the visualization and the analysis the ROOT framework was used and are described in more details in the paper [82].

Chapter 5

Analysis of experimental data

5.1 Calibration of the ΔE-E spectra

The calibration of the ΔE-E spectra for each pair of detectors has been done by the determination of the "punch through" points (see A.2) for each particle identified on the ΔE-E spectra.
With the program SPAR (see section A.1), one can calculate with good precision the energy loss of the particle in the matter. The SPAR program was used to calculate the energy loss of the particle at the "punch through"point. This energy loss is shown in the table 5.1, the column S1S2 describes the energy loss ΔES1 in the first silicon detector S1 and the energy loss ΔES2 in the second silicon detector S2 of the particle which passes through the first and the second detectors and enters in the third detector. In the next column S2S3, the particles are crossing 3 detectors and the maximum energy loss in the second and the third detector is described by ΔES2 and ΔES3 respectively. Note that ΔES2 in the column S1S2 is not the same as in column S2S3, because in the column S1S2 the particle is crossing only 2 detectors and in the column S2S3 the particle is crossing 3 detectors. The minimum energy required for a particle to cross silicon matter determined by the SPAR program and used to calculate the energy loss of the particle on the "punch through" is shown in the table 5.2. In the third column is shown the minimum energy required for a particle to cross the first silicon detector (with material length 50 μm) and the second silicon detector (with material length 400 μm) and still to enter the next silicon detector. In the same way, the last column shows the minimum energy required for the respective particle to cross the second silicon detector (with material length 400 μm) and the third silicon detector (with material length for detection angle 35^{o} and 65^{o} respectively 6000 and 5000 μm) and enter to the phoswich detector.

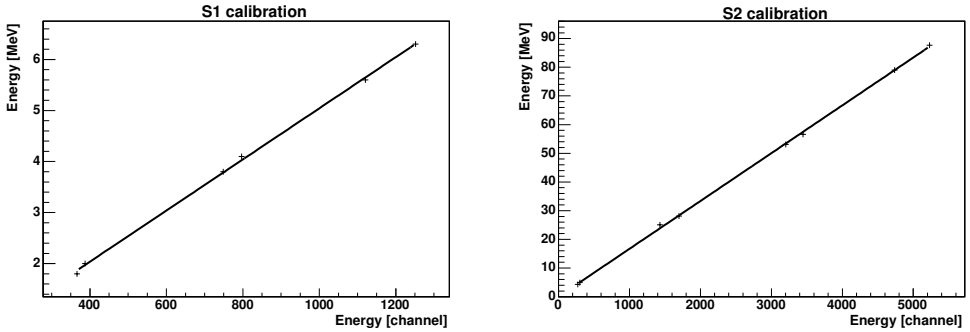

Figure 5.1: Linear fit for the energy calibration of silicon detector S1 (50 μm) and silicon detector S2 (400 μm).

Particle Type	Arm Number	S1S2 ΔES1 ΔES2 [MeV]	S2S3 ΔES2 ΔES3 [MeV]	S3S4 ΔES3 ΔES4 [MeV]
^{3}He	01	4.7 28.2	6.1 98.7	
^{4}He	01	5.3 32.1	6.9 112.7	
^{6}Li	01	10.0 60.7	13.0 212.4	
^{7}Li	01	10.7 64.6	14.0 227.7	
^{7}Be	01	14.8 89.8	19.3 315.0	
^{9}Be	01	16.5 99.4	21.5 350.9	
^{10}Be	01	17.4 104.2	22.6 368.2	
^{10}B	01	22.3 134.7	29.0 472.4	
^{11}B	01	23.3 140.1	30.2 493.3	
^{3}He	03 and 04	1.8 25.1	4.3 117.3	
^{4}He	03 and 04	2.0 28.1	4.9 133.0	
^{6}Li	03 and 04	3.8 53.1	9.3 249.8	
^{7}Li	03 and 04	4.1 56.6	9.9 267.5	
^{7}Be	03 and 04	5.6 79.0	13.7 370.6	
^{9}Be	03 and 04	6.3 87.7	15.3 413.4	
^{10}Be	03 and 04	6.6 91.1	16.0 432.7	
^{10}B	03 and 04	8.5 117.8	20.6 556.7	
^{11}B	03 and 04	8.9 122.7	21.5 580.3	
^{3}He	05	1.8 25.1	4.7 106.1	
^{4}He	05	2.0 28.1	5.3 118.9	
^{6}Li	05	3.8 53.1	10.0 226.3	
^{7}Li	05	4.1 56.6	10.7 241.3	
^{7}Be	05	5.6 79.0	14.8 333.1	
^{9}Be	05	6.3 87.7	16.6 372.5	
^{10}Be	05	6.6 91.1	17.3 390.6	
^{10}B	05	8.5 117.8	22.3 502.3	
^{11}B	05	8.9 122.7	23.2 523.4	
^{3}He	07	1.8 25.1	9.0 42.6	16.3 62.6
^{4}He	07	2.0 28.1	10.2 47.7	18.5 70.7
^{6}Li	07	3.8 53.1	19.3 90.8	
^{7}Li	07	4.1 56.6	20.6 97.0	
^{7}Be	07	5.6 79.0		
^{9}Be	07	6.3 87.7		
^{10}Be	07	6.6 91.1		
^{10}B	07	8.5 117.8		
^{11}B	07	8.9 122.7		
^{3}He	08	4.7 28.2	6.8 85.1	
^{4}He	08	5.3 32.1	7.7 97.6	
^{6}Li	08	10.0 60.7	14.5 184.8	
^{7}Li	08	10.7 64.6	15.5 197.2	
^{7}Be	08	14.8 89.8	21.4 272.3	
^{9}Be	08	16.5 99.4	23.9 304.2	
^{10}Be	08	17.4 104.2	25.0 319.5	
^{10}B	08	22.3 134.7	32.2 410.0	
^{11}B	08	23.3 140.1	33.5 428.1	

Table 5.1: Energy loss of the particle on the “punch through” points calculated with the SPAR program. For description see text.

The first step consists to read the values of the “punch through” from the row experimental ΔE-E spectrum.

The second step is to plot an histogram with “punch through” energy values determined by the simulation versus the uncalibrated values determined from the row data. A line is fitted and this linear function obtained scales the channel to the energy unit (see Fig. 5.1).

Detection angle	Particle type	$E1_{min}$ [MeV]	$E2_{min}$ [MeV]	$E3_{min}$ [MeV]
35 and 50^o	^{3}He	26.9	122.3	
35 and 50^o	^{4}He	30.4	138.7	
35 and 50^o	^{6}Li	57.3	261.3	
35 and 50^o	^{7}Li	61.1	279.5	
35 and 50^o	^{7}Be	84.8	386.2	
35 and 50^o	^{9}Be	94.1	431.0	
35 and 50^o	^{10}Be	98.4	451.3	
65^o	^{3}He	26.9	111.2	
65^o	^{4}He	30.4	126.2	
65^o	^{6}Li	57.3	237.6	
65^o	^{7}Li	61.1	254.2	
65^o	^{7}Be	84.8	351.3	
65^o	^{9}Be	94.1	392	
65^o	^{10}Be	98.4	410.4	
100^o	^{3}He	26.9	52.6	86.0
100^o	^{4}He	30.4	58.4	97.4
100^o	^{6}Li	57.3	112.4	183.6
100^o	^{7}Li	61.1	120.1	196.4
100^o	^{7}Be	84.8	166.2	271.4
100^o	^{9}Be	94.1	185.1	302.9
100^o	^{10}Be	98.4	193.8	317.0

Table 5.2: Minimum energy for a particle needed to cross 2 silicon detectors and enter to the next one. See explanation in the text.

5.2 Solid angle of detectors

Detectors used in PISA experiment cover various solid angle (see table 5.3). The solid angle of each detector is taken into account and proper normalization of data is applied.

Detection Angle [deg]	Detector Name	Distance from Target [mm]	Active Area [mm^2]	Solid Angle [msr]
15	MCP START	394	254.5	1.639
	MCP STOP	910	254.5	0.307
	BCD Diaphragm	1212	452.4	0.308
	Si1	1475	900	0.414
	Si2	1485	900	0.408
	Si3	1494	706.9	0.317
	Phoswich	1579	541.5	0.217
35	Si1 cooled	667.4	150	0.337
	Si2 cooled	686.4	150	0.318
	Si3 cooled	701.9	200	0.406
50	Si1 cooled	631.5	150	0.376
	Si2 cooled	650.5	150	0.354
	Si3 cooled	666	200	0.451
65	Si1 cooled	572.56	150	0.457
	Si2 cooled	588.56	150	0.433
	Si3 cooled	607.56	200	0.542
100	Si1 cooled	487.08	150	0.632
	Si2 cooled	502.58	150	0.594
	Si3 cooled	525.58	150	0.543
	Si4 cooled	536.58	150	0.521
120	MCP START	126	254.5	16.030
	MCP STOP	642	254.5	0.617
	BCD Diaphragm	944	415.5	0.466
	Si1	1207	900	0.618
	Si2	1217	900	0.608
	Si3	1227	706.9	0.470
	Phoswich	1311	541.5	0.315

Table 5.3: General informations about the PISA experimental setup.

5.3 Particle Identification Method

In order to identify the particular isotopes and to prepare the energy spectra for each of them, the following identification procedure is applied to the ΔE-E spectra.
The spectra analysis was performed with the use of ROOT software [83]. This graphical software has the possibility to make a two dimensional graphical cut on the spectra and then take for the analysis only the event included in this cut.
With this tool, the first step is to isolate the hyperbola of the particle of interest putting a cut surrounding the interesting events, as it is shown in the Fig. 5.2. In the first pair of silicon detectors the bottom part of the hyperbola is not taken in the cut, because this part shown in the Fig. 5.3 (left picture) as the part between B and D corresponds to the particle crossing silicon detectors S1, S2 and S3. Between B and D the particle has the choice to be stopped between B and C or between C and D. In order to have more precise information about the particle crossing each detector in the interval between B and D, the spectrum corresponding to the second pair of silicon detectors is analyzed (see right picture in the Fig. 5.3). Again like for the first pair of silicon detectors the

cut is put on the top part of the hyperbole as the part between B and C. This interval corresponds to the case when the particle is crossing the detector S1, S2 and is stopped in the detector S3. Unfortunately, as shown in the Fig. 5.3 in the right picture, the last part it means between C and D is not possible to separate the particle due to the superposition of 2 kinds of particles and of the lack of a next detector. However only light particles like ^{3}He and ^{4}He are the most penetrative and are not stopped in the last silicon detector.For heavier particles an unambiguous identification is possible since they are stopped in the last Si-detector (as has been shown in table 5.2).

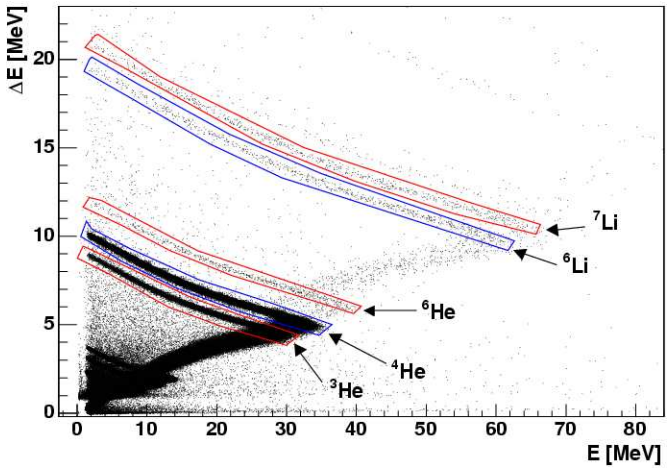

Figure 5.2: Picture showing representatively the method used to separate the isotopes from the typical ΔE-E spectrum in the second pair of detectors.

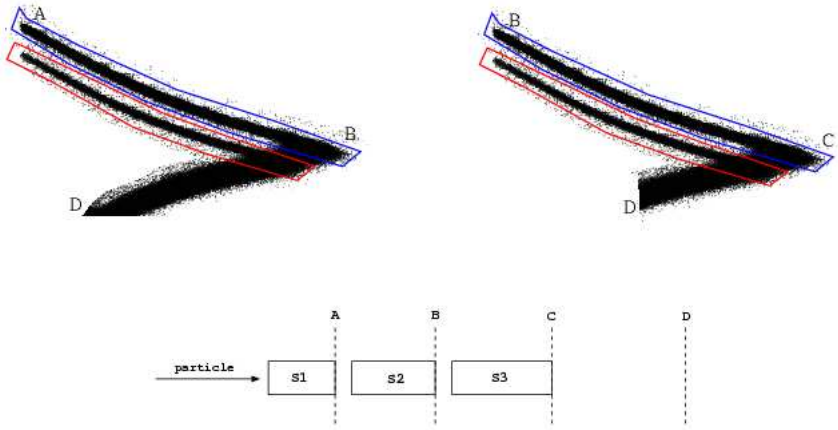

Figure 5.3: Schematic explanation of the identification method with ΔE-E spectrum from silicon detectors.

The method described above is applied for the first and second pair of silicon detectors in each

arm. In this way a good particle identification is obtained.
In the following the method used to select the particles and to see the mass distribution is called center of gravity method. This method is based on fitting a function to the hyperbola obtained in the ΔE-E plot of a pair of silicon detectors. This function will be the center of gravity for the neighboring hyperbola. It means that for each points around the center of gravity, the shortest distance from this point to the center of gravity will be calculated and plotted. For example, if the ^{6}He is taken as the center of gravity then the maximum of the peak will be close to zero and the peak corresponding to ^{3}He and ^{4}He at the negative side of the plot (on the left). For easy see which peak corresponds to which particles, the scale was linearly modified to obtain the x-axis in atomic mass units.
The mass distributions obtained by this method are shown in the Fig. 5.4 for the helium, lithium, beryllium isotopes. A mass resolution of $\Delta A/A \approx 10\%$ is obtained for the isotopes shown in Fig. 5.4. For elements up to Z=5, this is sufficient to allow for the correct identification of different isotopes up to A=12. The upper right panel of Fig. 5.4 shows the mass resolution of Z=2 isotopes on a logarithmic scale in order to visualize the existence of ^{6}He. Note also in the lower panel of Fig. 5.4 for Z=4 the lack of ^{8}Be due to its rather short lifetime of $0.7 \cdot 10^{-16}$ sec.

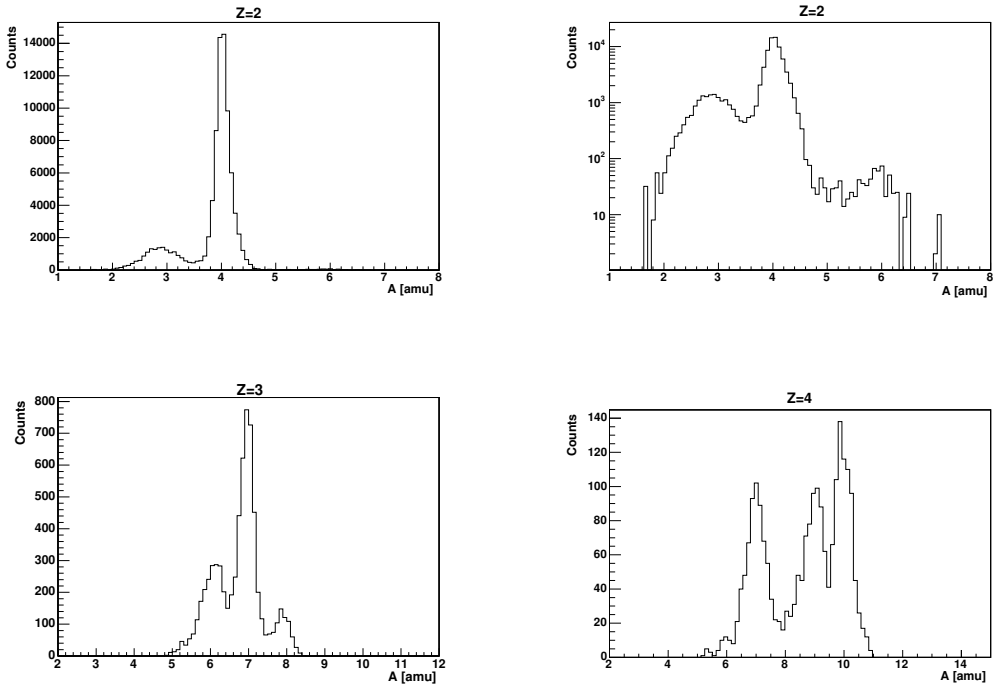

Figure 5.4: Mass distributions of He (Z=2), Li (Z=3) and Be (Z=4) in the reaction p(2.5 GeV)+Au measured by the silicon detector telescope at the detection angle of 35°. The thickness of the 2 silicon detectors are 50 μm and 400 μm.

Chapter 6

Experimental results

The main goal of the present experiment was to measure the energy spectra of particles emitted in the reaction p+^{197}Au at 2.5 GeV proton energy. As it was discussed earlier, the application of telescopes consisted of silicon detectors allows for charge and mass identification of the detected particles. The cooled silicon telescopes placed at 35^{o}, 50^{o} and 100^{o} enabled us to measure energy spectra with good identification of ^{3}He, ^{4}He, ^{6}He, ^{6}Li, ^{7}Li, ^{8}Li, ^{7}Be, ^{9}Be, ^{10}Be, ^{10}B, ^{11}B, ^{12}B isotopes as well as to distinguish the carbon, nitrogen and oxygen particles (without mass separation). Heavier particles were not observed due to the small cross sections for their emission and thus, the low statistics of events. The thickness of the silicon telescopes was large enough to stop lithium and heavier ions emitted in the reaction, however the helium ions could pass through the telescopes leaving only part of their energy. Information on the energy range of the particles registered by the telescopes is summarized in the Table 6.1. For each detected particle depicted in the first column, the detection angle is listed in the second column whereas the observed energy range of the particles is presented in the third column, respectively.
The experimental spectra measured at 35^{o} , 50^{o} and 100^{o} are shown in figs.6.1-6.5. The presented data were measured with the same luminosity for all particles thus the relative cross sections are well defined. Two separate components can be clearly distinguished in the ^{4}He and ^{6,7}Li spectra. The cross section and shape of the low energy component does not change in principle with the emission angle. On the contrary, the slope of the high energy component increases with the scattering angle i.e. the cross sections at large angles decrease faster with energy than those at small angles. Such decomposition of spectra into two components is less obvious for ^{3}He and ^{7}Be whereas for other particles there are no indications for presence of two components.
The low energy component can be interpreted as a contribution from the compound nucleus emission. Then the higher energy component should correspond to faster, pre-equilibrium processes. The qualitative behavior of the spectra of heavier ejectiles does not give unambiguous indication what kind of the reaction mechanism is responsible for the emission processes. As can be seen in table 6.1 and figs. 6.1-6.5 the lower energy threshold determined by the thickness of the Si detector S1 is of the order of 2-3 MeV/A.

Particle type	Detection angle	Energy Range [MeV]
^{3}He	35^{o}	8-119
^{3}He	50^{o}	8-113
^{3}He	100^{o}	8-77
^{4}He	35^{o}	8-143
^{4}He	50^{o}	8-137
^{4}He	100^{o}	8-95
^{6}He	35^{o}	11-135
^{6}He	50^{o}	11-131
^{6}He	100^{o}	11-95
^{6}Li	35^{o}	15-163
^{6}Li	50^{o}	15-163
^{6}Li	100^{o}	15-111
^{7}Li	35^{o}	19-159
^{7}Li	50^{o}	19-159
^{7}Li	100^{o}	19-119
^{8}Li	35^{o}	19-59
^{8}Li	50^{o}	19-63
^{8}Li	100^{o}	19-67
^{7}Be	35^{o}	23-111
^{7}Be	50^{o}	23-111
^{7}Be	100^{o}	23-83
^{9}Be	35^{o}	27-79
^{9}Be	50^{o}	27-87
^{9}Be	100^{o}	27-79
^{10}Be	35^{o}	27-79
^{10}Be	50^{o}	27-87
^{10}Be	100^{o}	27-83
^{10}B	35^{o}	35-79
^{10}B	50^{o}	39-87
^{10}B	100^{o}	35-83
^{11}B	35^{o}	35-83
^{11}B	50^{o}	39-87
^{11}B	100^{o}	39-91
^{12}B	35^{o}	35-67
^{12}B	50^{o}	39-75
^{12}B	100^{o}	39-71
C	35^{o}	43-111
C	50^{o}	43-127
C	100^{o}	43-99
N	35^{o}	55-123
N	50^{o}	55-119
N	100^{o}	55-103
O	35^{o}	67-119
O	50^{o}	63-123
O	100^{o}	71-115

Table 6.1: Measured energy interval for particles detected at 35^{o}, 50^{o}, and 100^{o}.

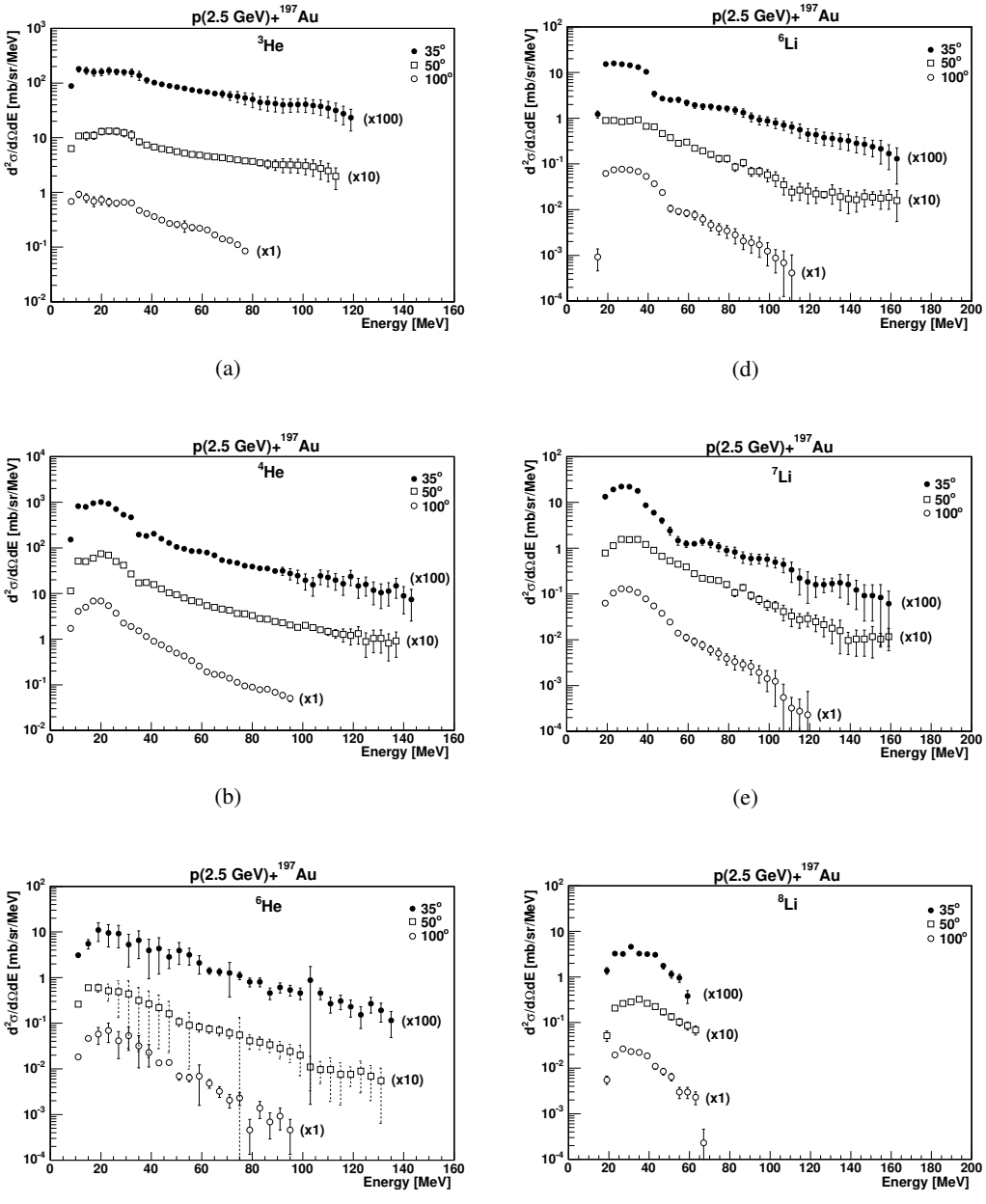

Figure 6.1: Energy spectra of ^{3,4,6}He and ^{6,7,8}Li as measured by the telescope at 35^{o} (closed circles), 50^{o} (squares) and 100^{o} (open circles). The errors shown in the figure are only the statistical ones. The errors which are not depicted in the figure are smaller than the size of the symbols.

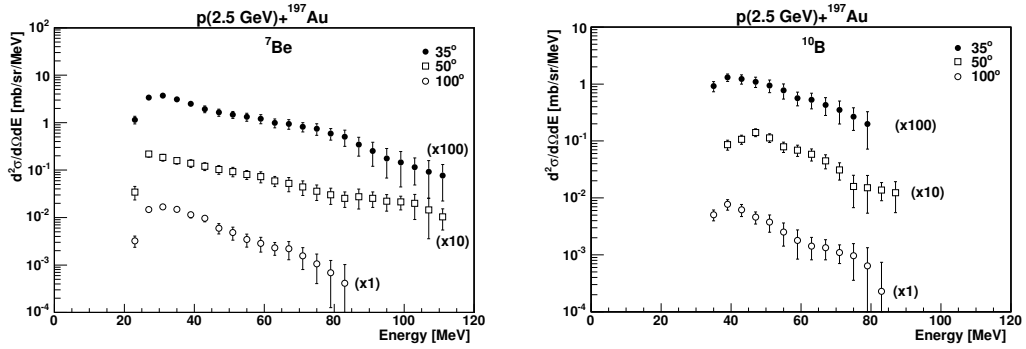

(a)

(d)

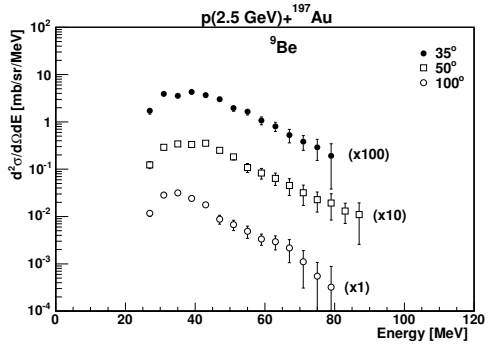

(b)

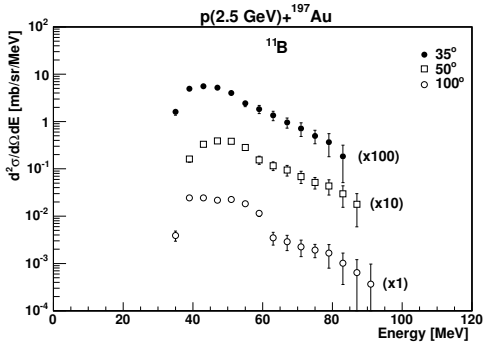

(e)

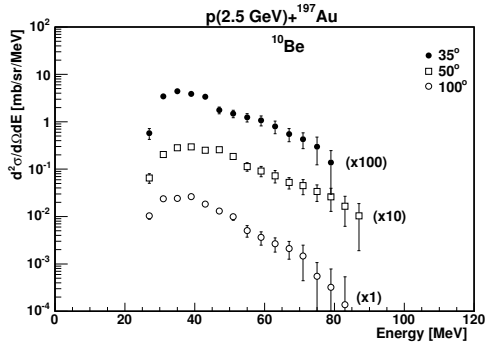

(c)

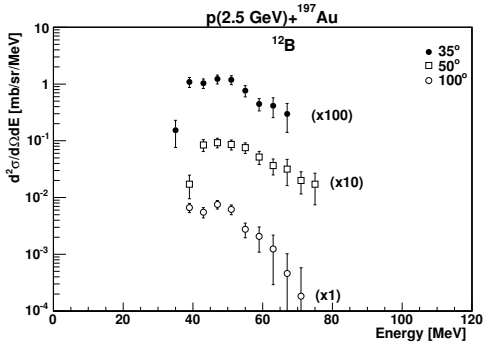

(f)

Figure 6.2: Same as Fig. 6.1 but for ^{7,9,10}Be and ^{10,11,12}B.

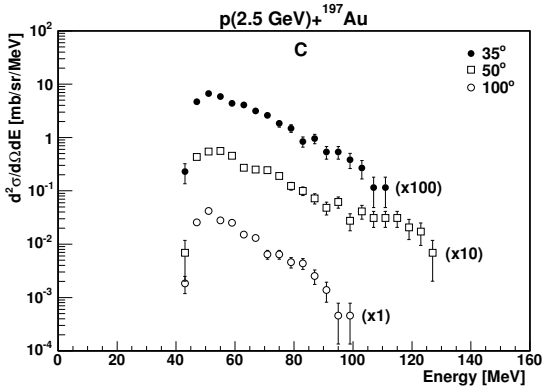

Figure 6.3: Same as Fig. 6.1 but for carbon.

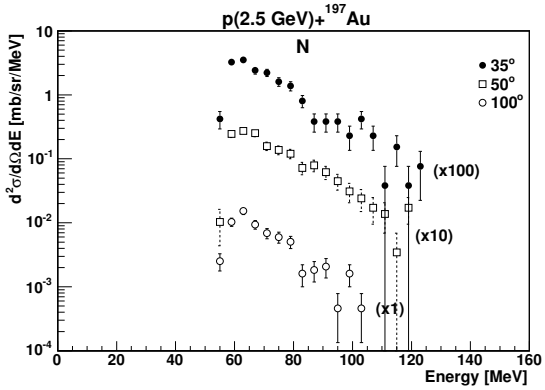

Figure 6.4: Same as Fig. 6.1 but for nitrogen.

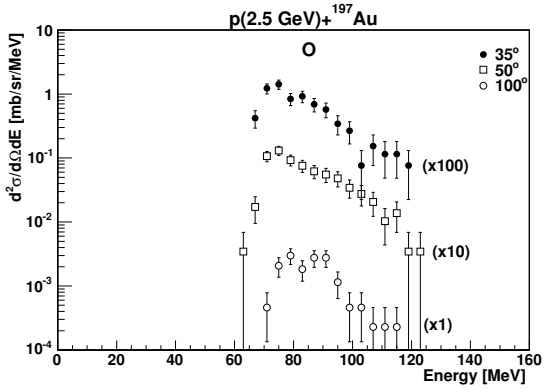

Figure 6.5: Same as Fig. 6.1 but for oxygen.

The absolute value of the cross sections was achieved by comparison of our ^{4}He spectrum measured at 35^o to the data of NESSI collaboration obtained for the same reaction, i.e. p(2.5 GeV)+^{197}Au$\rightarrow^4$He+X at 30^o [29]. The normalization factor was found by comparing energy integrated yield from our experiment with energy integrated spectrum from NESSI. The low energy component of the both spectra gives dominating contribution to the energy integrated cross section and thus the normalization factor is mainly determined by this component. However, it should be emphasized that the shape of our spectrum of ^{4}He agrees well with the shape of spectrum mea-

sured by NESSI collaboration [29] and therefore both the normalized spectra, presented in Fig. 6.6 overlap in the limits of statistical errors for the full observed energy range. The comparison of ^{4}He spectra measured at 100^o (our data) and 105^o (NESSI data) depicted in the Fig. 6.7 shows also a good agreement. Of course, the same normalization factor – found at 30^o – was used for 100^o. Spectra for all other isotopes have been normalized with the same normalization factor (see Fig. 6.7).

The double differential cross sections for IMF's emission from the p+Au reactions are rather scarce. For the reaction under consideration, i.e. p(2.5 GeV)+^{197}Au, our data could be compared only with 2 experiments; with the data from Letourneau et al. (NESSI experiment) [29] for the ^{3}He, ^{4}He and ^{6}Li, ^{7}Li particles and from Katcoff [28] as concerns ^{8}Li ejectiles.

Comparison of our data for ^{3}He, ^{4}He, ^{6}Li and ^{7}Li measured at angle 35^o and 100^o with those measured by Letourneau et al. [29] at 30^o and 105^o is presented in Fig.6.7. As can be seen in this figure, our data for ^{3}He emission differ significantly from the data of Letourneau et al. . The difference is largest at 30^o , where ratio of our data to NESSI data is equal to 3 – 3.5, and slightly smaller at 100^o where this ratio is approximately equal to 2. The ^{6}Li spectra agree well in the limit of the statistical errors, however, the agreement of ^{7}Li spectra is poorer. Our data are systematically larger by a factor of about 2.

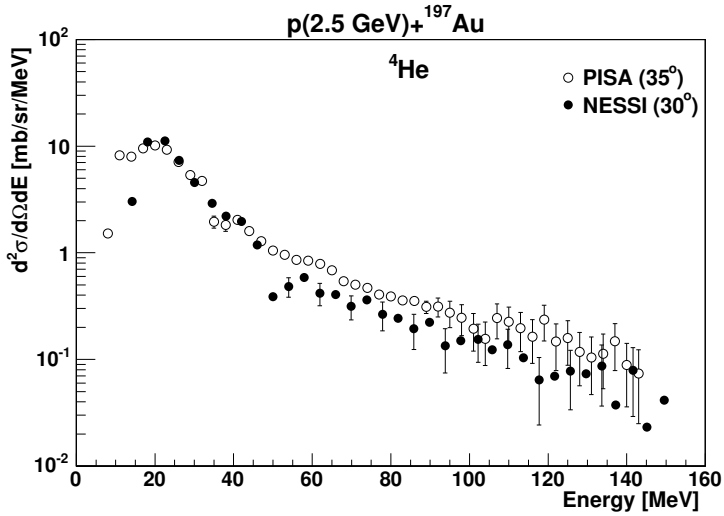

Figure 6.6: ^{4}He energy spectra normalization between our data and NESSI experiment. Filled symbols show the energy spectra from NESSI [29] for detection angle 30^o and not filled symbols show our experimental data for respectively detection angle 35^o.

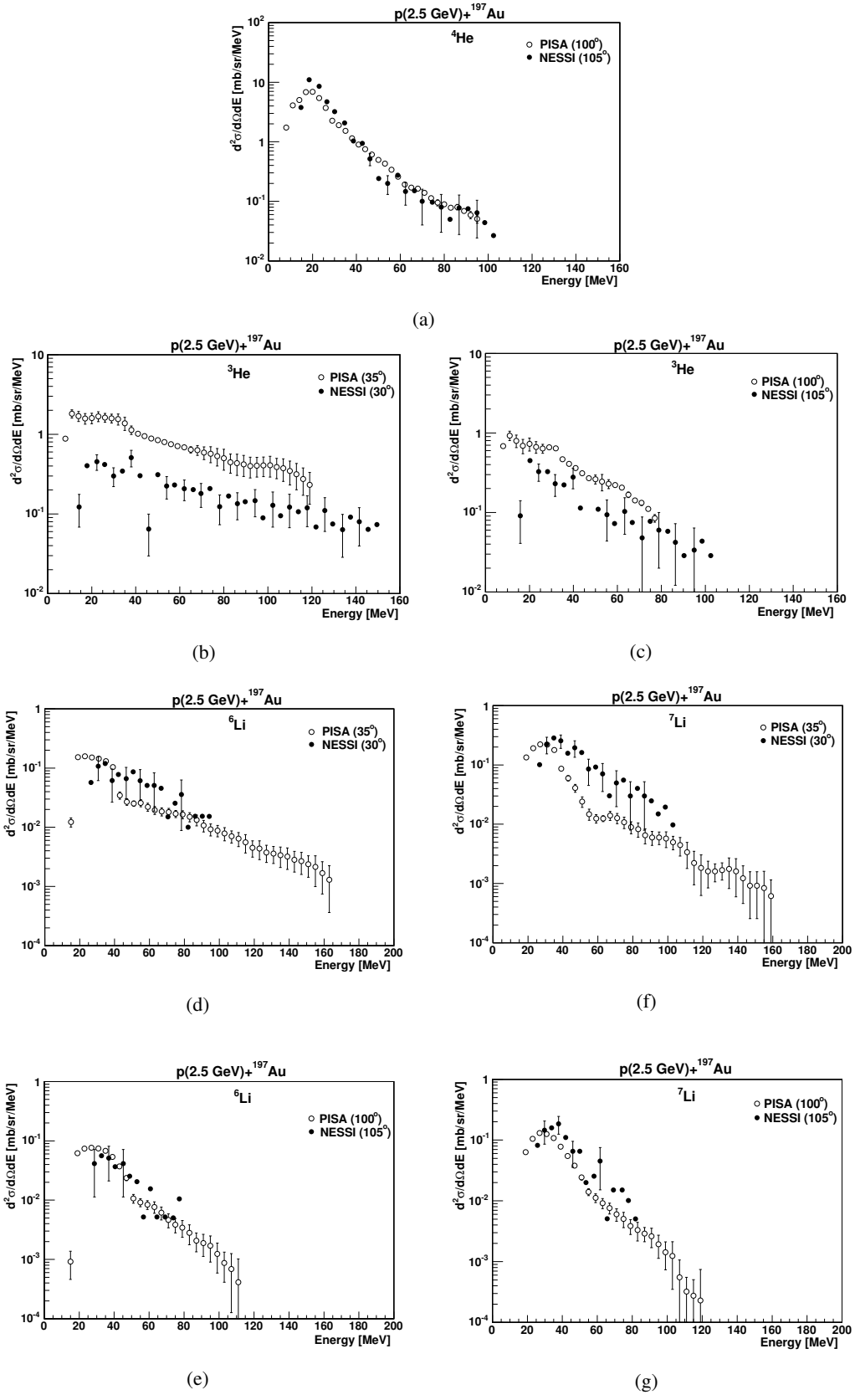

Figure 6.7: Comparison of the energy spectra from the present experiment and data of the NESSI collaboration [29]. Filled symbols show the energy spectra from NESSI for detection angle 30° and 105° whereas not filled symbols show our experimental data for detection angle 35° and 100°, respectively.

In the case of ^{8}Li ejectiles, our data were compared with the data from Katcoff [28] which were measured in the reaction p+^{197}Au at slightly smaller energy than the ours (2.2 GeV instead 2.5 GeV).
In Fig. 6.8, our ^{8}Li spectra for detection angles of 35^{o} and 50^{o} are compared to Katcoff data at 35^{o} and 55^{o} . The data from Katcoff experiment, which are given in arbitrary units, were normalized to our ^{8}Li data. The normalization has been achieved by comparing the present data at 35^{o} integrated over energy interval between 19 MeV and 59 MeV to the data of Katcoff integrated over the same energy range. A good agreement is visible between both spectra. The data have been also compared at 50^{o} (55^{o} for Katcoff). In this case the shape of both spactra is also very similar but the absolute values of the Katcoff data are larger – slightly over the limits of statistical errors.

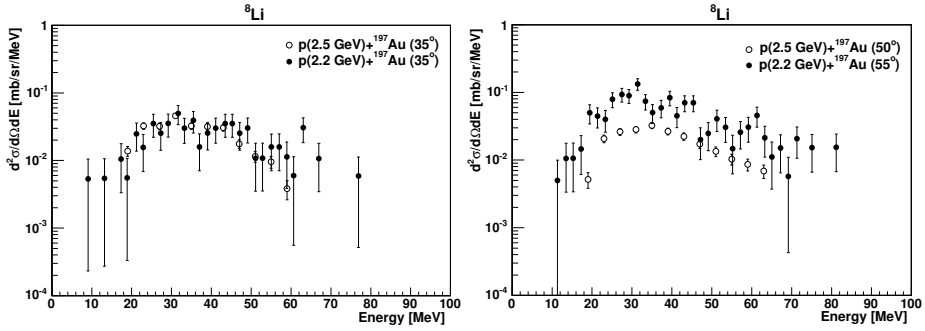

Figure 6.8: Comparison of the ^{8}Li energy spectra. Filled circles show the energy spectra from Katcoff [28] measured at 35^{o} and 55^{o}, respectively, and not filled circles show our experimental data measured at 35^{o} and 50^{o} in respect to the proton beam.

In summary, we measured the double differential cross sections $d\sigma/d\Omega dE$ for ^{3,4,6}He, ^{6,7,8}Li, ^{7,9,10}Be, ^{10,11,12}B, carbon, nitrogen, and oxygen ejectiles in a large energy range (up to 150 MeV). The energy distributions for He and Li ejectiles obtained in the present experiment were compared with the data from two other experiments [29], [28]. The agreement of the ^{4}He and ^{6}Li data is very good, the ^{8}Li data agrees also reasonably well but in the case of ^{3}He the data show a discrepancy. The cross sections from present experiment are approximately 3 times larger than those measured by NESSI. It seems also that our ^{7}Li cross sections are systematically larger than NESSI data, however, large statistical errors of NESSI data do not allow to claim that the significant discrepancy exists. Due to better statistics achieved in our experiment than that obtained in previous experiments we were able to measure data not available previously in the literature. There are spectra of ^{6}He , ^{7,9,10}Be, ^{10,11,12}B, as well as spectra of carbon, nitrogen, and oxygen ejectiles (without mass separation). In the next section the analysis will be presented of our data using the INCL+GEM model and the phenomenological model of isotropically emitting sources.

Chapter 7

Model analysis

The reaction mechanism attributed to nucleon - nucleus collisions at nucleon energies of few GeV is not well known up to now. This should be considered as a serious drawback because knowledge of mechanism of such reactions is interesting by itself and, moreover, it can help to understand the mechanism of high energy reactions induced by heavy ions. Whereas emission of low energy particles can be reasonably well described by the compound nucleus mechanism, the existing models are not able to explain the emission process of high energy intermediate mass fragments (IMFs). In this chapter, the analysis of the reaction products from the reaction p(2.5 GeV)+^{197}Au will be presented, which has been done experimentally taking into consideration the low energy as well as high energy ejectiles with a hope to obtain new information on the reaction mechanism.
As it was discussed in the previous chapter, we observed in the present experiment the light and intermediate mass fragments from ^{3}He up to oxygen within the energy range from below the Coulomb barrier up to 150 MeV. From the qualitative analysis of the spectra two processes seem to be dominant in the reaction under consideration: the evaporation process at low energies of the emitted fragments and the non-equilibrium process which manifest itself by the presence of high energy tails of the spectra. In the first section, we describe the former process using the generalized evaporation model GEM (see section 3.2) whereas the latter contribution is analyzed by means of the phenomenological model called moving source model as discussed in section (7.2). In the third section the charge and mass dependence of the abundance of the reaction products is presented as extracted from the GEM and phenomenological model of the moving source. This dependence is compared with predictions of the Fisher's droplet model.

7.1 Comparison between model predictions and experiment

The GEM (Generalized Evaporation Model) model described in the chapter (3.2) may be applied for analysis of the composite particle emission up to $Z = 12$, thus it was used for description of our experimental data. The information (E^*, A, Z) on the population of the excited states of the remnant at the end of the fast, non-equilibrium stage of the reaction is the necessary input to the GEM model. The INCL4.2 (Intra Nuclear Cascade) code of Cugnon [56] has been used for this purpose. For all comparisons the standard parameter set of the INCL4.2 and GEM have been applied respectively and no adjustment of any model parameter has been performed. The models allow the determination of absolute cross sections.
Figs. 7.1-7.4 show for the reaction under consideration double differential cross sections for various isotopes as measured by PISA in comparison to the predictions as calculated by INCL4.2

coupled to GEM. As already described, composite particles can not be produced during the fast pre-equilibrium phase modeled by the INCL4.2. It should be pointed out that the INCL program takes into account only non equilibrium processes of the first step of the reaction which are accompanied by emission of protons, neutrons and pions. Therefore it is obvious that the comparison for composite particles will be restricted to the evaporation part which manifests essentially in the emission of ejectiles in the lower kinetic energy regime. The evaporation of ejectiles modeled by GEM for the equilibrium phase is expected to be isotropic in the *center of mass system* of the emitting compound nucleus. A momentum transfer to the remnants calculated by the INCL4.2 caused by the impinging high energy incident proton has been taken into account and the anisotropy predicted by GEM *in laboratory system* is explained exclusively by this kinematical boost. In the figures 7.1-7.3 this effect is reflected by the small shift towards higher kinetic energies of ejectiles for more forward angles. In other words e.g. evaporated ^{3}He particles calculated by GEM exhibit on the average 3-5 MeV higher energies for emission angles at 35 ^{o} compared to backward angles of 100^o as can be seen in the left panel of Fig. 7.1. The small forward velocity[1] of this "moving source" will in section 7.2 be shown to be of the order of $\beta_z \approx 0.0036$ on the average. The *integrated* production cross section calculated for the elements does not depend on the emission angle and only the position of the distributions $\frac{d^2\sigma}{dEd\Omega}$ is slightly varying with laboratory angle.

When looking at the low energy domain of the kinetic energy distributions generally a reasonable agreement with the experimental values is observed in particular for backward direction (100^o). As expected all *measured* spectra exhibit a tail of high kinetic energies ranging far further than the GEM calculations allow. The slope of the high energy part of the *measured* spectra is increasing with the detection angle which might indicate a decreasing non-equilibrium component for larger angles.

As shown in the right panel of Fig. 7.1 for ^{4}He and detection angles 35^o, 50^o and 100^o the position of the maxima of experimental spectra is in agreement with position of the maxima of the spectra evaluated with the code with exception of the data measured at 100^o where the experimental maximum is shifted to slightly smaller energy. Since the ^{4}He shows a pronounced evaporation peak (in contrast to ^{3}He), the agreement between measured spectra below 35 MeV and evaporation contribution as calculated is therefore more obvious than for other isotopes. The relative ratios of the respective evaporation and pre-equilibrium contributions will be discussed in detail later. The ^{6}Li spectra measured as represented in Fig. 7.2 show a little pathological behaviour and are the only ones being clearly lower than the calculated cross sections $\frac{d^2\sigma}{dEd\Omega}$ throughout all angles under consideration. Foresure all predictions given by GEM calculations also underly some systematical error. As input parameters to the statistical evaporation code GEM there is for example the dependence on the mass and charge of the highly excited hot nucleus and the thermal excitation energy E^* as provided by the INCL code right before reaching equilibrium.

The calculations were done also for heavier particles. The comparison of the data and the model results leads to similar picture for all studied ejectiles.

The contribution of the evaporation mechanism dominates at low energies of the detected particles but disagreement of the theoretical and experimental high energy tails of the spectra shows that the non-equilibrium mechanism gives a contribution to spectra of all observed particles. This is illustrated by Fig. 7.3, where the energy spectra of ^{7}Li, ^{9}Be and ^{11}B measured at 50^o are shown. In the case of ^{7}Li and ^{9}Be, the evaporative part is well reproduced. In contrast, the cross section for ^{11}B is slightly underestimated by the code.

[1] in respect to the beam direction

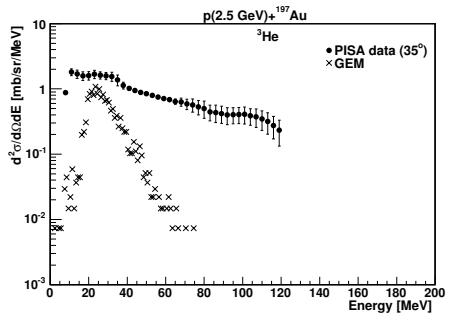

(a)

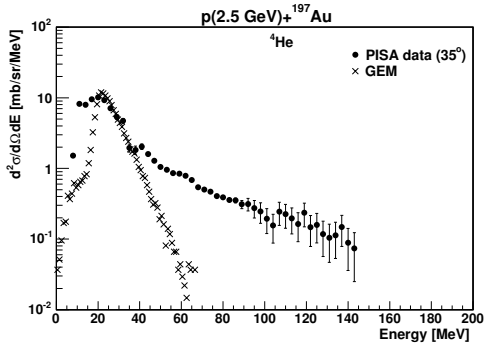

(d)

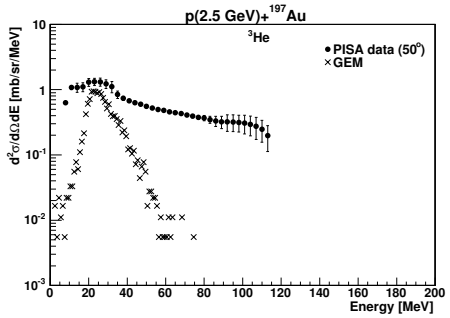

(b)

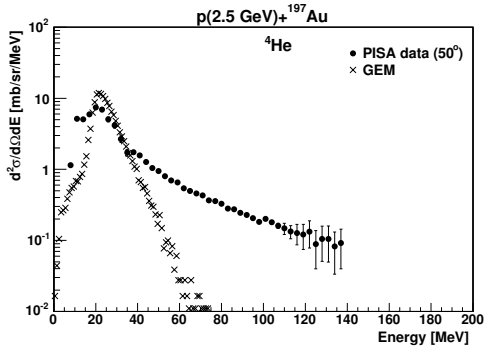

(e)

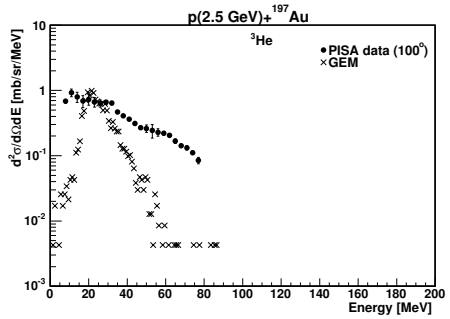

(c)

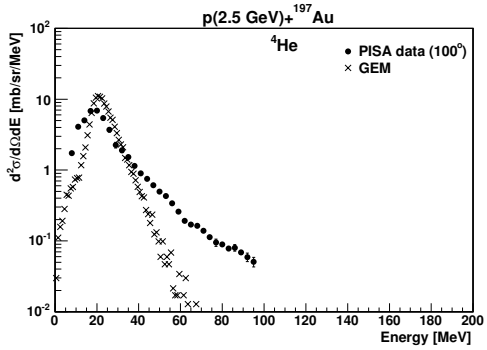

(f)

Figure 7.1: The comparison between energy spectra of ^{3}He and ^{4}He measured at 35^o, 50^o and 100^o by PISA collaboration (full dots) and model calculations performed within GEM (crosses).

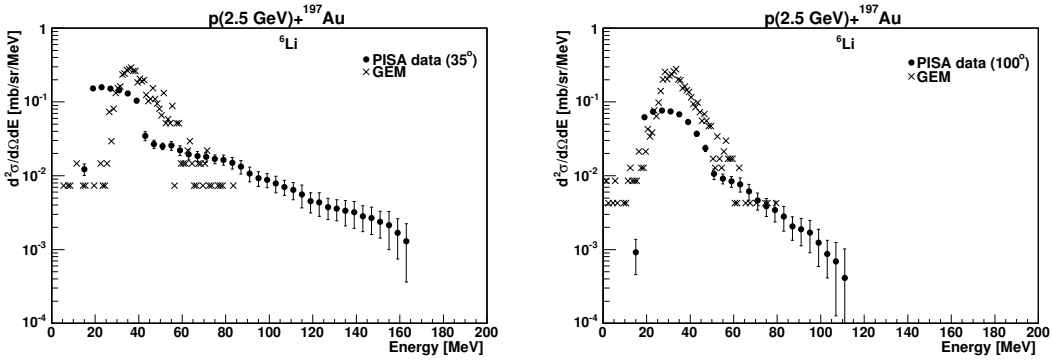

Figure 7.2: The comparison between energy spectra of ^{6}Li, measured at 35^{o} and 100^{o} by PISA collaboration (full dots) and model calculations by means of GEM (crosses).

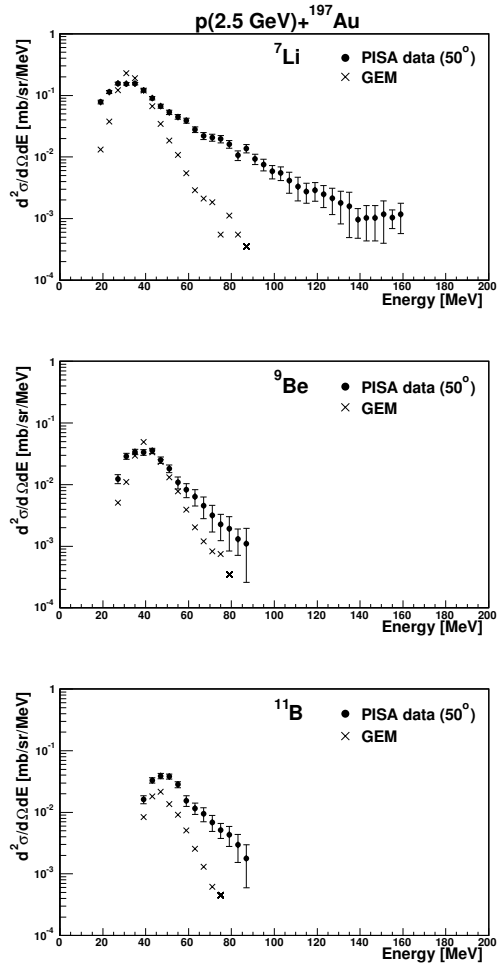

Figure 7.3: The comparison between energy spectra of ^{7}Li, ^{9}Be and ^{11}B measured at 50^{o} by PISA collaboration (full squares) and model calculations by means of GEM (crosses).

For C, N and O (see Fig. 7.4) in the calculation an integration over the full azimuthal angle $0^{o} \leq$

$\theta \leq 180^{o}$ has been performed in order to increase the statistics of the calculation. This is to some first order justified, since the spectra of C, N and O do not depend much on the emission angle. The agreement with the spectra is best for the emission at 100 ^{o} (i.e. most measured backward direction) for all three elements. The somewhat surprising fact that this agreement gets worse the smaller the observed emission angle is might be an indication, that even in this low kinetic energy domain a contribution of particles resulting from pre-equilibrium processes accounts. Most astonishing being the fact that this tendency is observed even for elements as heavy as C, N and O. This again would be an effect which couldn't be reflected in the evaporation spectra as calculated by the statistical model GEM.

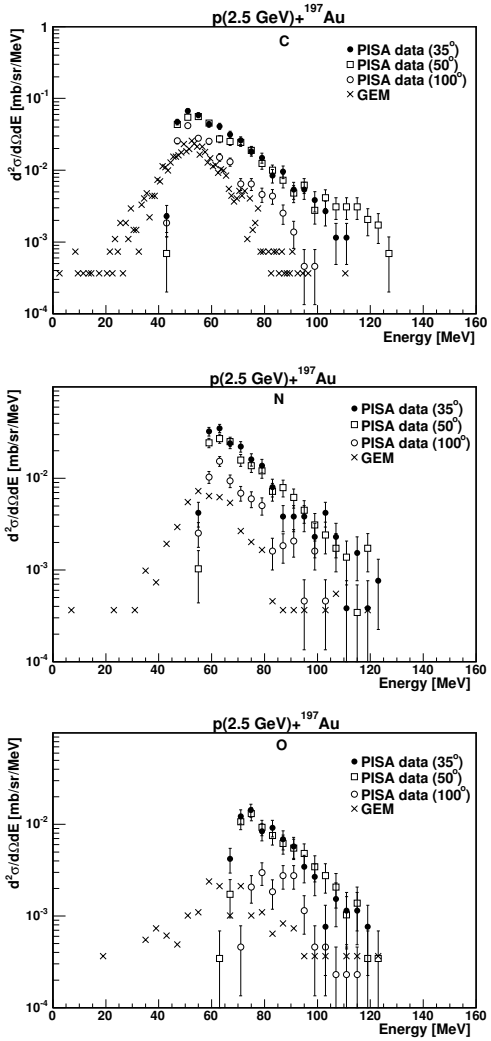

Figure 7.4: The comparison between energy spectra of C, N and O measured at 35^{o}, 50^{o} and 100^{o} by PISA collaboration (full dots, open squares and open dots respectively) and model calculations by means of GEM (crosses). Note that in the GEM calculation an integration over the full azimuthal angle $0^{o} \leq \theta \leq 180^{o}$ has been performed.

As mentioned above, the comparison is done on an absolute scale and therefore please note the remarkably good agreement for the domain of kinetic energies closes to the lower detection threshold and maximum of the kinetic energy distributions even for the heavy elements massive as C, N

and O.
Note that the lack of experimental data for the lower energy (most obvious in particular for heavier ejectiles) is avowed by the experimental detection energy threshold (ejectiles being stuck in target and 1st detector).
The deficiency to describe composite high energy particles emitted prior to equilibrium of the system is certainly the lynchpin of further investigations as concerns the development of codes.

7.2 Moving source fits

There are no models which can quantitatively describe the emission of composite, energetic particles. Therefore we have used the phenomenological model of 2 moving sources with the aim to obtain information on both, the evaporation process as well as the fast emission from the non-equilibrium stage of the reaction. The eventual agreement of the phenomenological analysis of the evaporation process with results obtained in the frame of the GEM would enable us to anticipate that the successful phenomenological analysis of high energy part of the spectra gives equally good results. Such a phenomenological treatment of both processes on the equal footing allows to extract information on energy and angle integrated cross sections for both mechanisms of the reaction and thus allows to compare relative contributions of both processes.
The experimental data were described by equation (3.14) discussed in the section (3.4). The parameters were chosen according to the following prescription: The velocity of the compound nucleus was fixed at value $\beta_1 = 0.0036$ and other parameters were fitted to reproduce the experimental data (with exception of the temperature of the slow source for beryllium and boron ejectiles, which was fixed at value 8 MeV). The above value of the velocity β_1 of the compound nucleus was calculated using the equation (3.14) and multiplying the result by a factor of $\frac{1}{4}$ [84] to take into account the momentum of the nucleons and pions emitted in the first, fast stage of the reaction.
The search for appropriate values of other parameters of two emitting sources, i.e. fraction of the nominal Coulomb barrier k, temperature of the compound nucleus T_1, temperature T_2 and velocity β_2 of the fast source as well as the cross section of evaporation σ_1 and non-equilibrium process σ_2, was performed with request to minimize sum of squares given in equation (7.1).

$$Sum\ of\ squares \equiv \sum_i log(Y_i^{exp}/0.0001) \cdot \left[log\left(\frac{Y_i^{exp}}{Y_i^{theor}}\right)\right]^2 \tag{7.1}$$

As it seen this sum corresponds to the difference of the theoretical and experimental yields $Y(E_i)$ in the logarithmic scale and the weights are proportional to reciprocal of the square of the relative statistical error of the data (the single event in the energy bin of our data corresponds approximately to the cross section of 0.0001 mb). In the above sum of squares the data measured for all angles were included, thus the obtained parameters give the best fit for both, energy and angular dependence of the cross sections.
Instead of using a single value of the k parameter we introduced an averaging over distribution of this parameter in the following way: the energy spectrum $Y(E,k)$ was weighted by the Gaussian function:

$$\langle Y(E)\rangle \equiv \int_{-\infty}^{+\infty} dk\, Y(E,k) \frac{1}{(2\pi)^{1/2}\sigma(k)} e^{-\frac{(k-k_0)^2}{2\sigma^2(k)}} \tag{7.2}$$

where k_0 and $\sigma(k)$ are the mean value and the standard deviation of the Gauss function. The standard deviation $\sigma(k)$ was fixed at value $0.2k_0$.

There are evidently visible two components in the experimental spectra of ^{4}He (Fig. 7.6) and ^{6,7}Li (figs. 7.8 and 7.9); the low energy part with a dominant peak in the neighborhood of 20 - 30 MeV – almost independent of the scattering angle, and the high energy component which manifests itself by presence of the exponential tail with the slope increasing with the angle. The most likely interpretation of the low and high energy components is the evaporation and pre-equilibrium contribution, respectively. For other particles, like e.g. ^{3}He or IMF's heavier than Li the presence of two components is not so evident in the experimental spectra. Especially the spectra for carbon, nitrogen and oxygen could not be fitted with two source formula because the low energy part of the spectra is cut by the detection system. However, the analysis in the frame of the GEM model showed, that the high energy component is not negligible for all studied IMF's. From these reason we tried to fit parameters of two emitting sources wherever it was possible.

Table 7.1: Parameters determined by the moving source fits for energy spectra of different particles emitted in the reaction p+^{197}Au at 2.5 GeV.

Particle type	k_0	T_1 [MeV]	σ_1 [mb]	β_1	T_2 [MeV]	σ_2 [mb]	β_2	σ_{GEM} [mb]
^{3}He	0.25	8.3	240	0.0036	26.9	510	0.064	166.72
^{4}He	0.45	8.6±0.3	1830±80	0.0036	26.7±1.2	350±30	0.059±0.004	1725.36
^{6}He	0.23	-	-	-	15.8±0.6	30.2±1.8	0.028±0.002	29.59
^{6}Li	0.60	9.6±0.7	32.4±2.3	0.0036	29.5±1.8	9.9±1.4	0.048±0.006	54.67
^{7}Li	0.65	9.6±0.6	48.5±3.0	0.0036	27.3±2.0	10.7±2.0	0.029±0.005	43.86
^{8}Li	0.74	11.3±0.8	10.7±0.6	0.0036	-	-	-	13.58
^{7}Be	0.5	8.0	2.9	0.0036	18.6	8.3	0.023	5.69
^{9}Be	0.53	8.0	4.2	0.0036	15.6	9.4	0.0175	9.37
^{10}Be	0.53	8.0	2.2	0.0036	15.0	9.5	0.017	10.57
^{10}B	0.53	8.0	1.5	0.0036	16.5	4.2	0.018	5.78
^{11}B	0.65	8.0	4.5	0.0036	12.8	11.2	0.016	4.48
^{12}B	0.72	-	-	-	12.8	3.5	0.010	2.64
C	0.71	-	-	-	13.1±0.8	16.2±1.3	0.012±0.002	4.6
N	0.76	-	-	-	12.6±0.9	8.2±0.8	0.012±0.002	1.95
O	0.84	-	-	-	11.8±1	3.8±0.4	0.012±0.002	0.84
total			2187			957		2080

These fits are shown for helium (Fig.7.5-7.7), lithium (Fig.7.8-7.10), beryllium (Fig.7.11-7.13) and boron isotopes (Fig.7.14-7.15) respectively, and for carbon, nitrogen and oxygen without mass separation in Fig.7.17-7.19. The obtained values of the parameters are listed in the table 7.1.

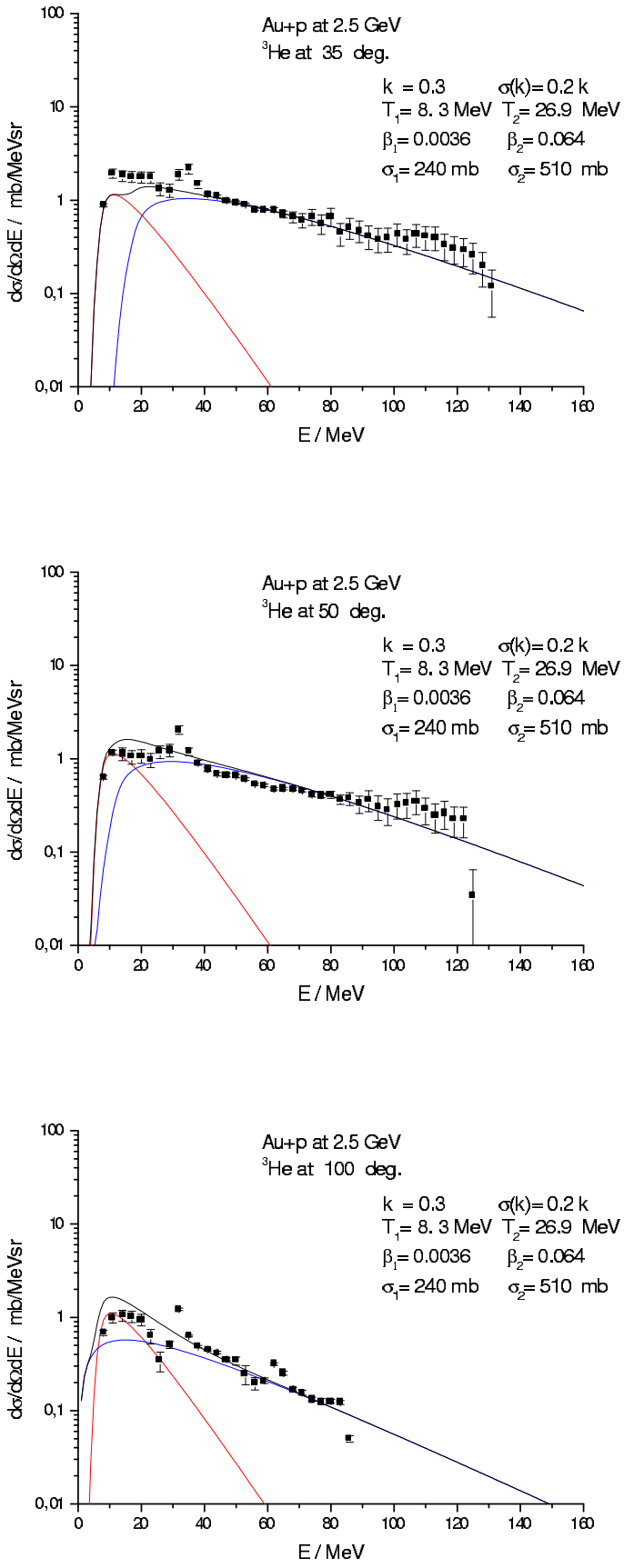

Figure 7.5: Energy spectra of ^{3}He fitted with the sum of two Maxwell functions.

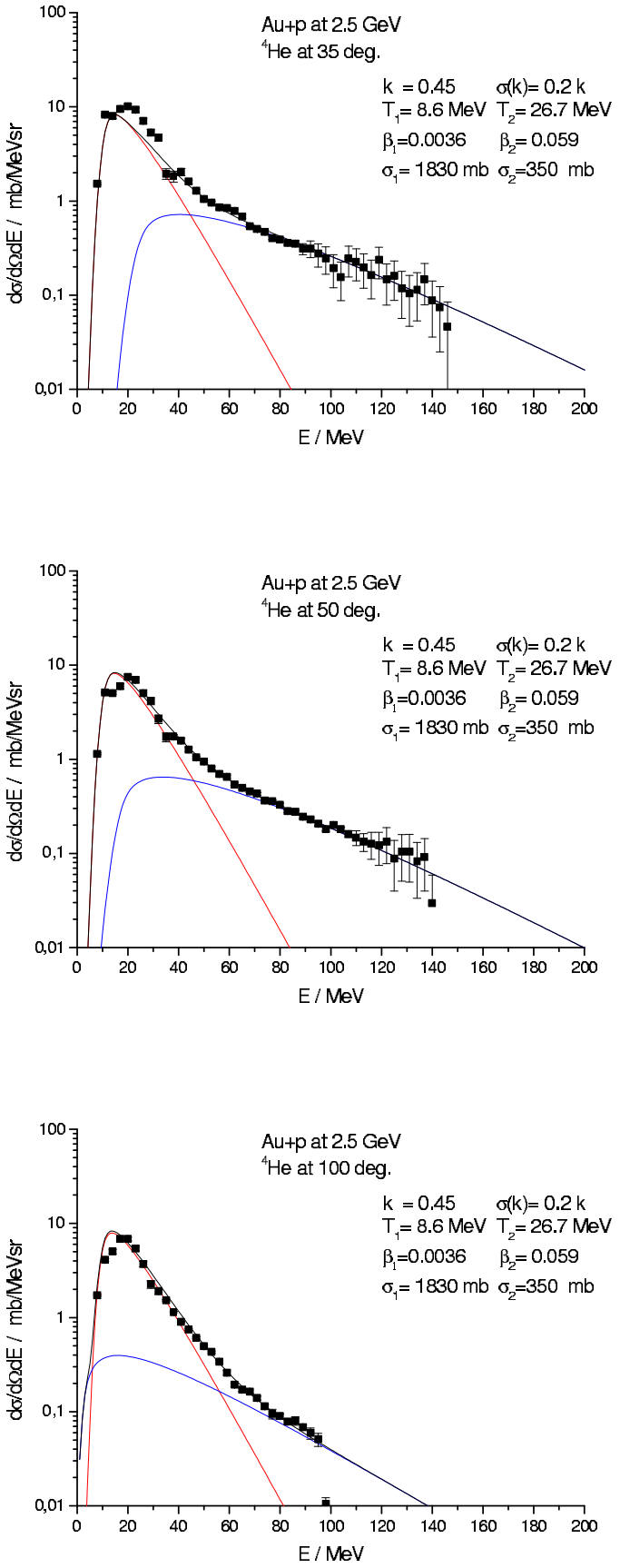

Figure 7.6: Same as Fig. 7.5 but for ^{4}He.

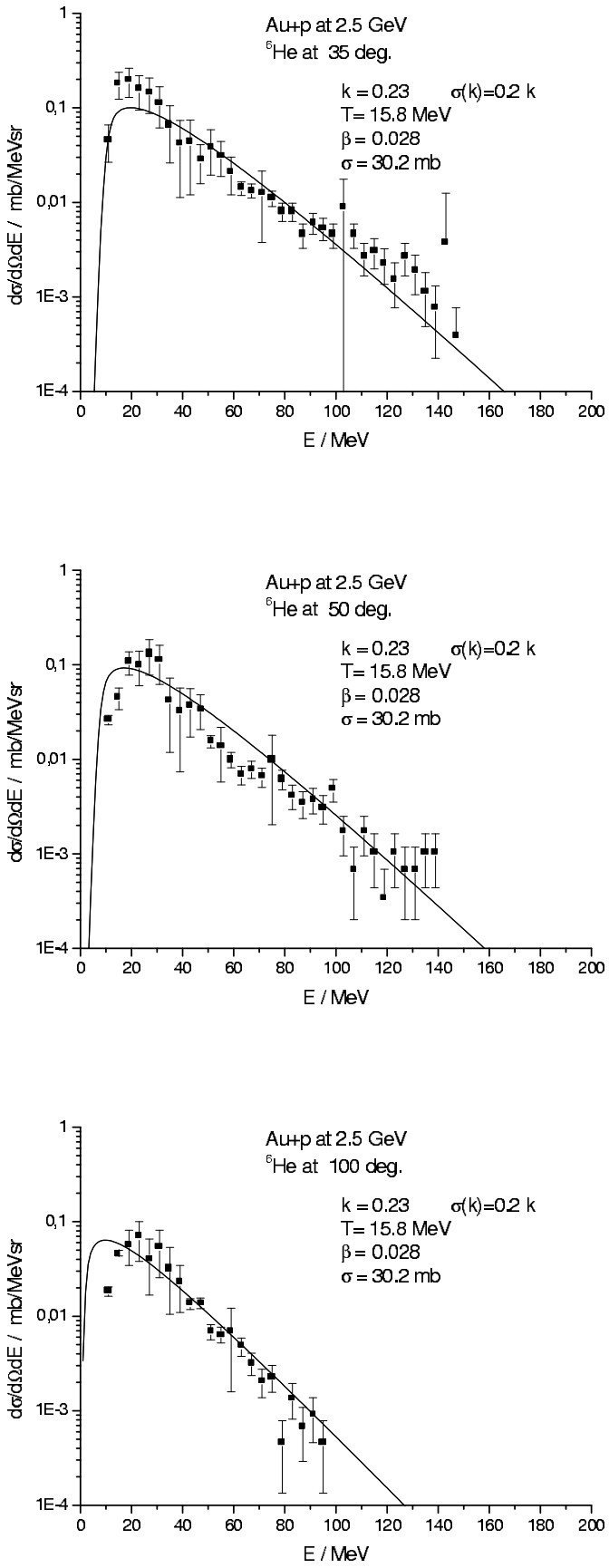

Figure 7.7: Energy spectra of ^{6}He fitted with only one Maxwell function

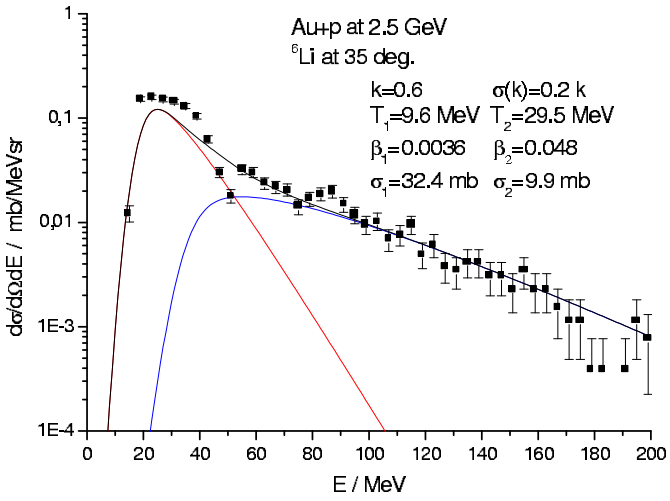

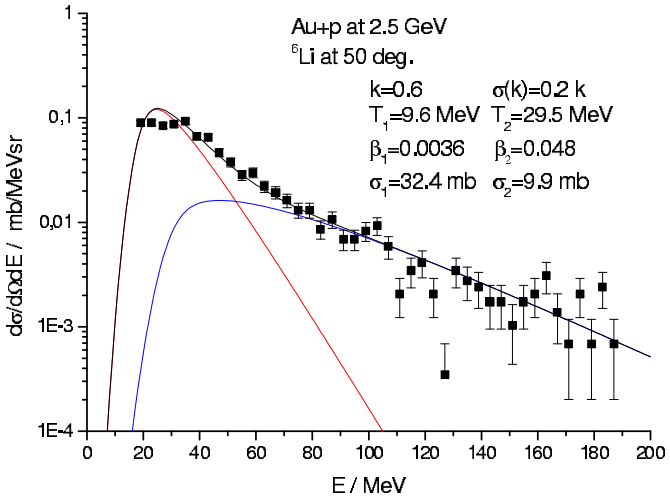

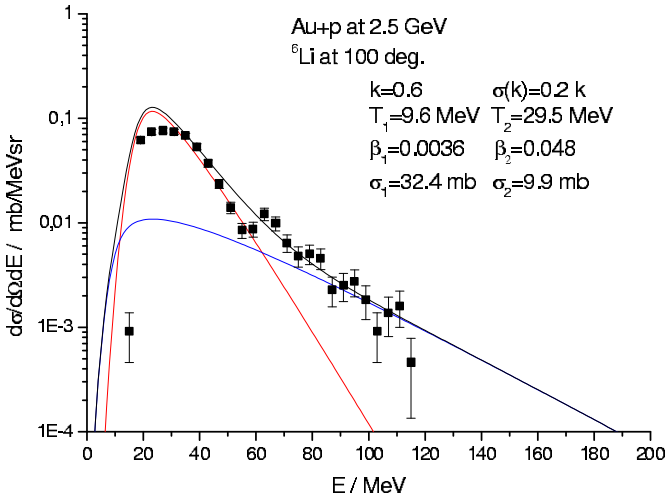

Figure 7.8: Same as Fig.7.5 but for ^{6}Li.

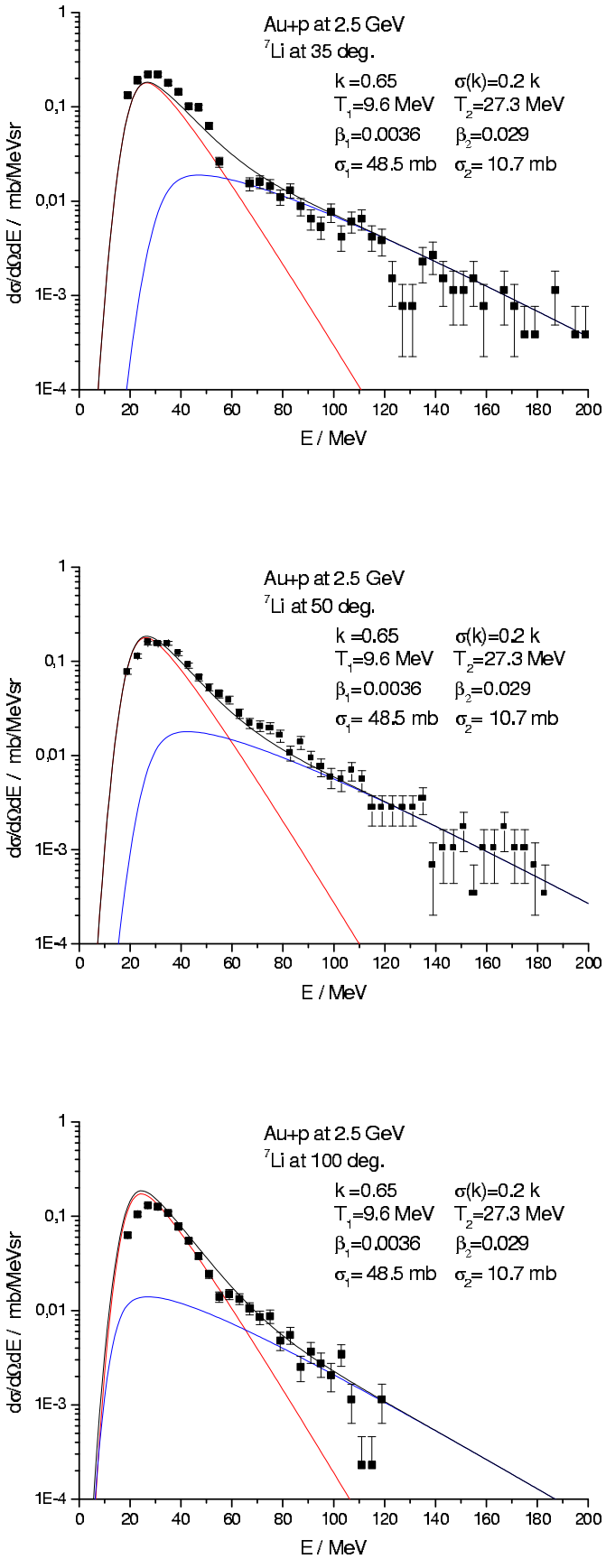

Figure 7.9: Same as Fig.7.5 but for ^{7}Li.

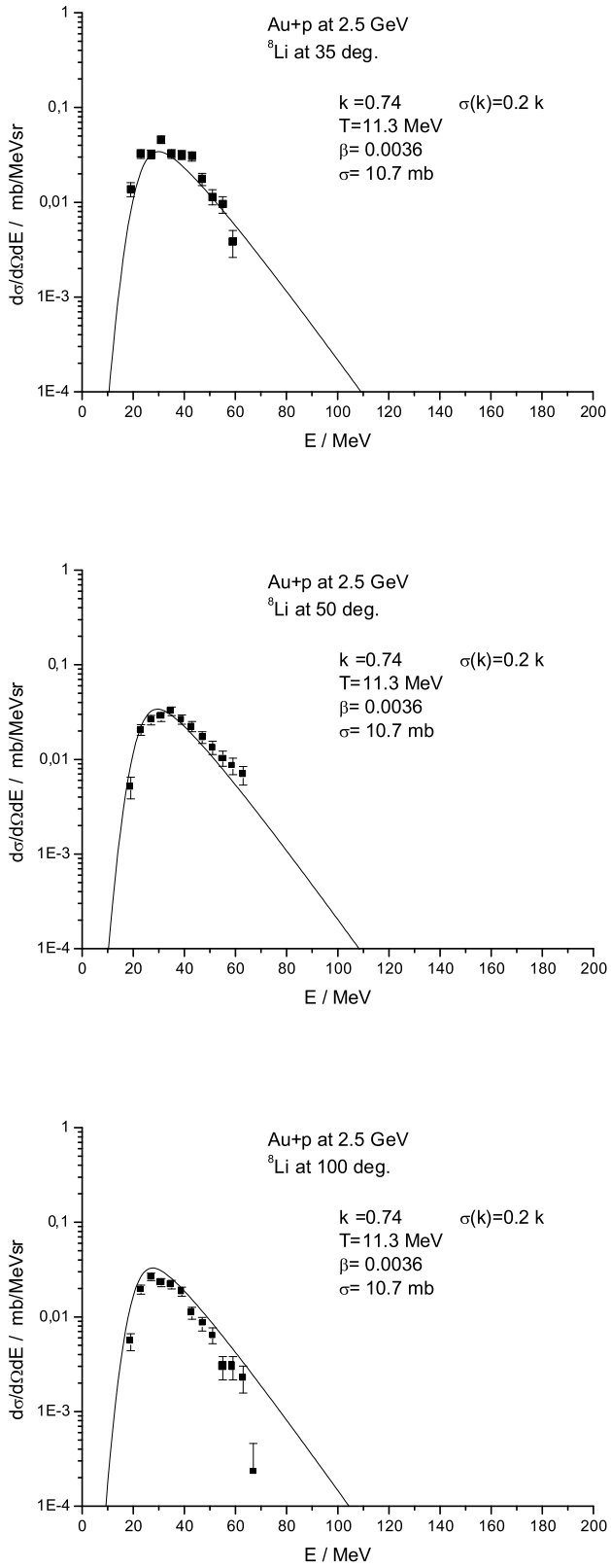

Figure 7.10: Energy spectra of ^{8}Li fitted with only one Maxwell function for temperature analysis.

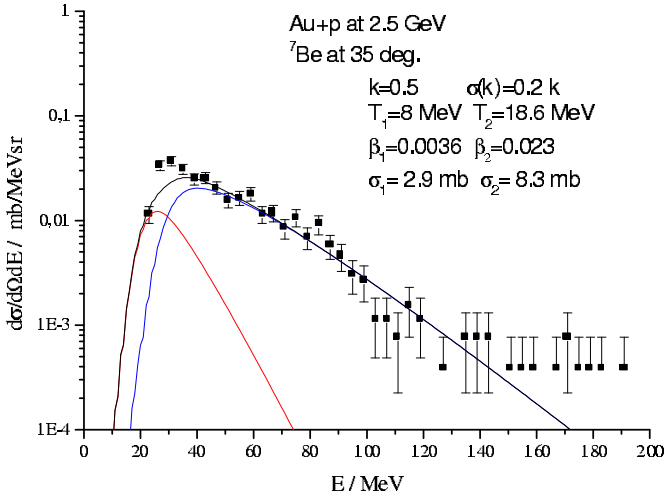

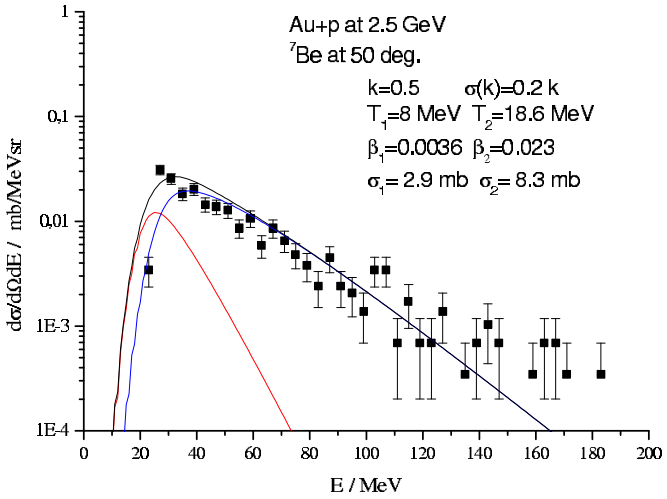

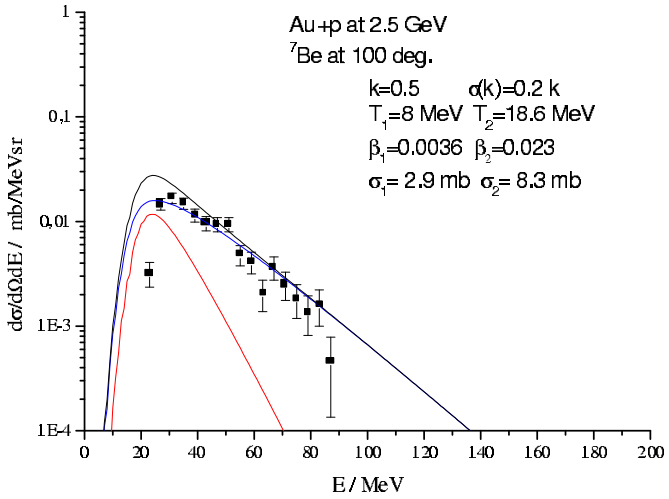

Figure 7.11: Same as Fig.7.5 but for ^{7}Be.

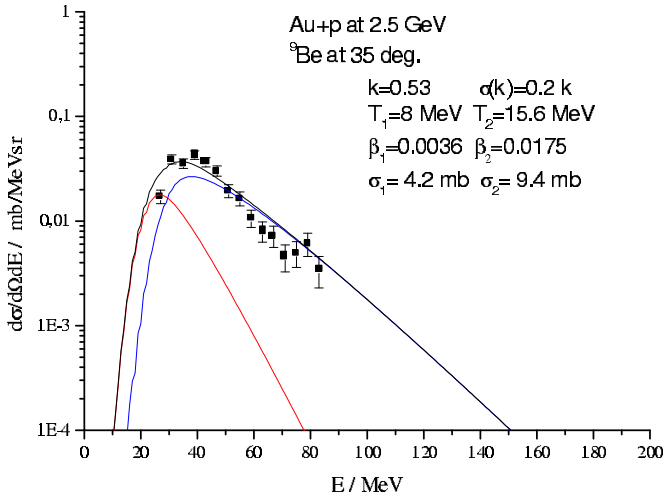

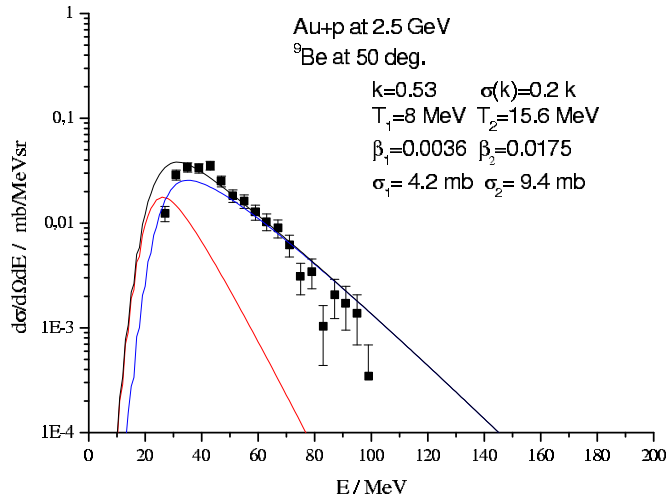

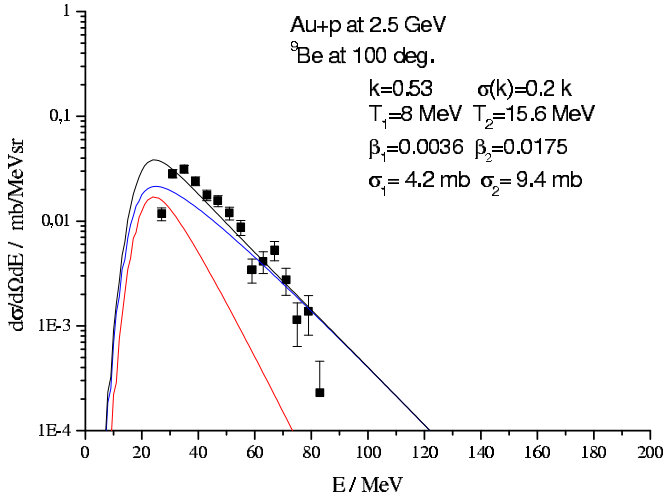

Figure 7.12: Same as Fig.7.5 but for ^{9}Be.

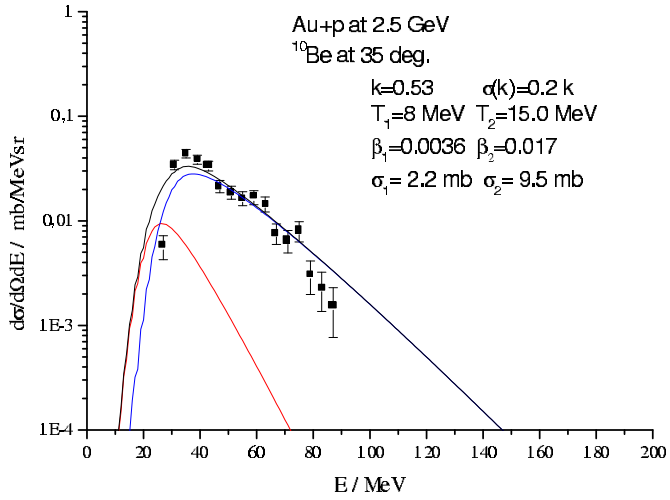

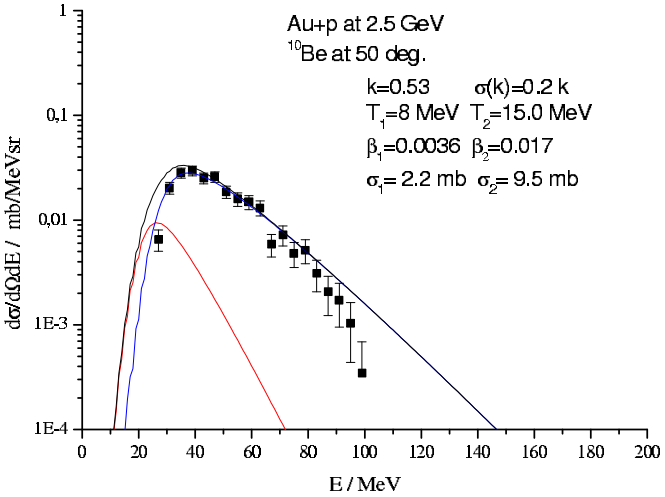

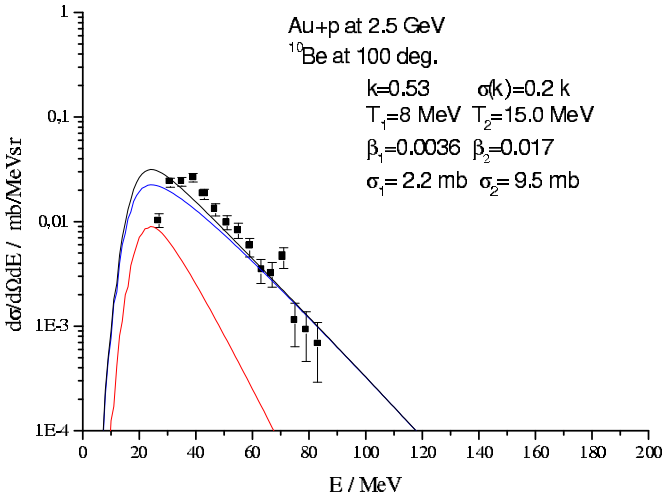

Figure 7.13: Same as Fig.7.5 but for ^{10}Be.

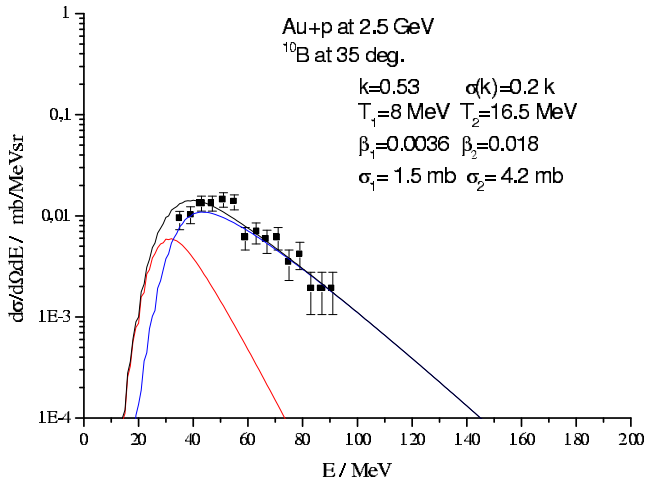

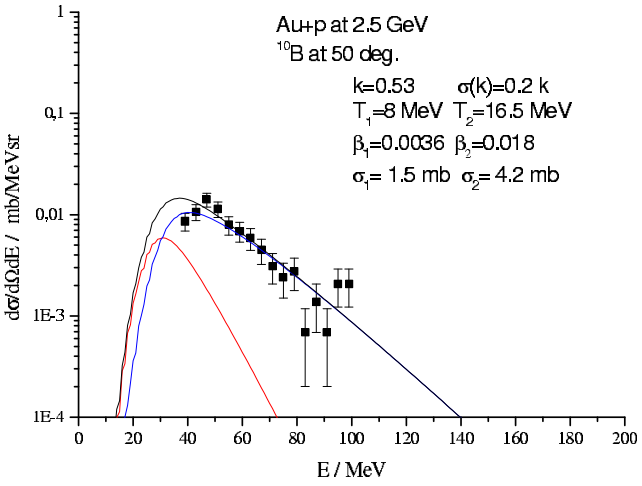

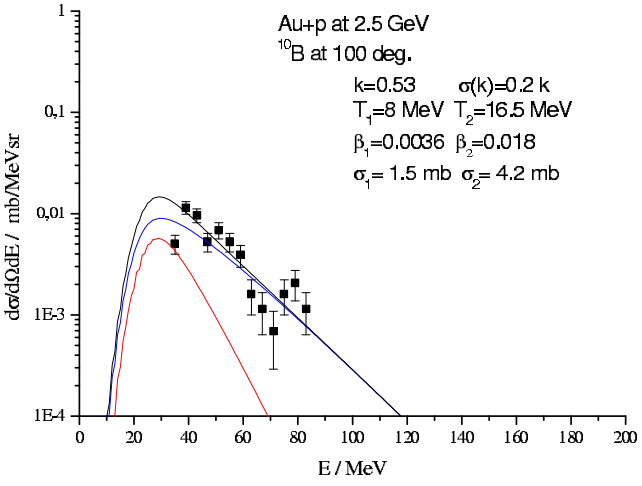

Figure 7.14: Same as Fig.7.5 but for ^{10}B.

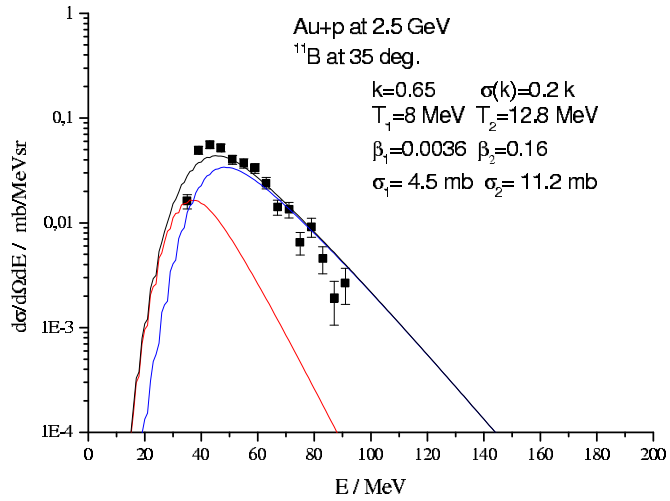

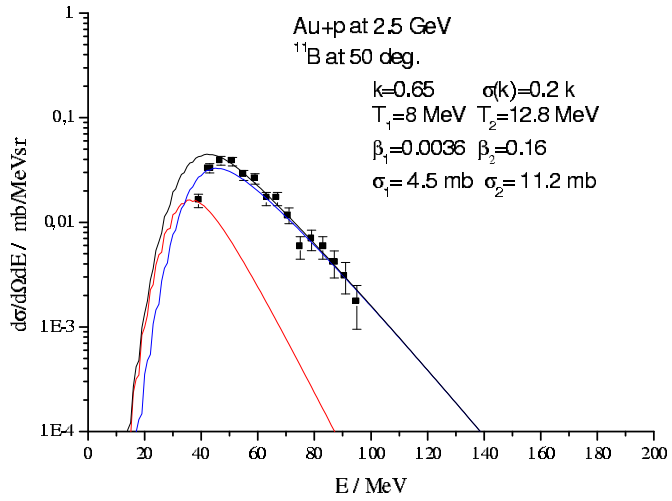

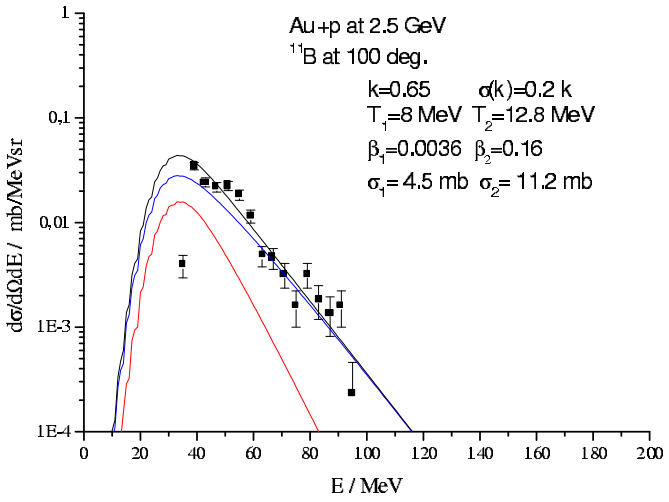

Figure 7.15: Same as Fig.7.5 but for ^{11}B.

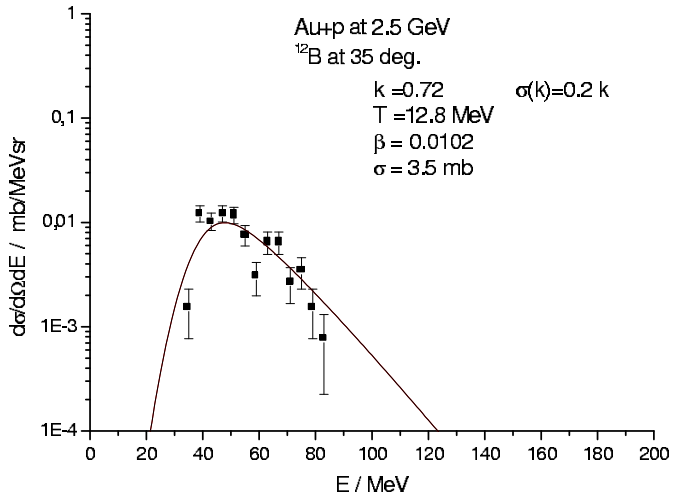

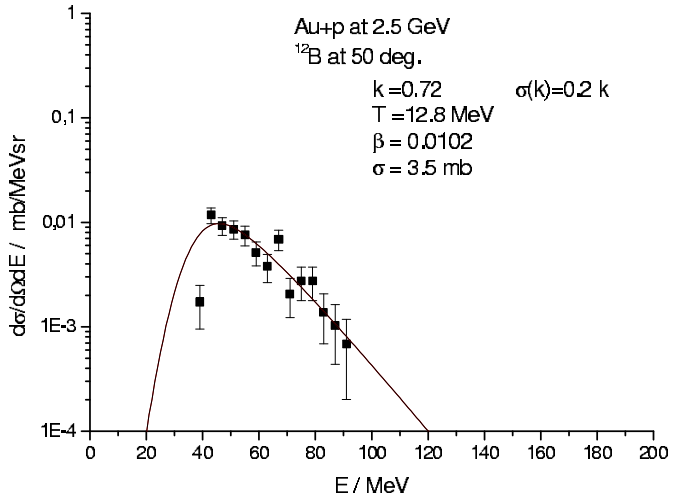

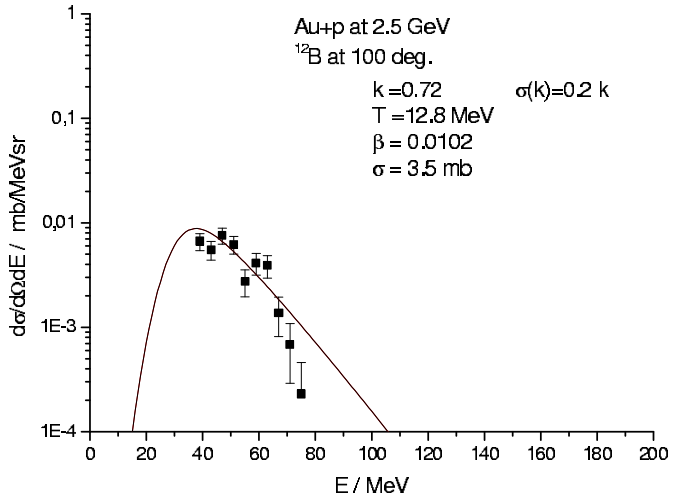

Figure 7.16: Same as Fig.7.5 but for ^{12}B.

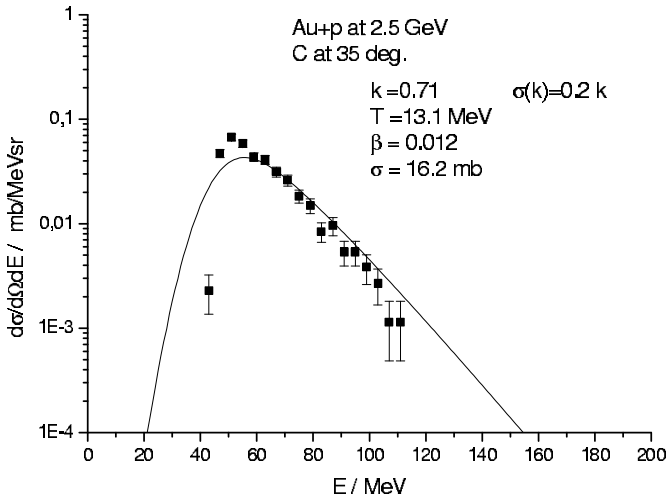

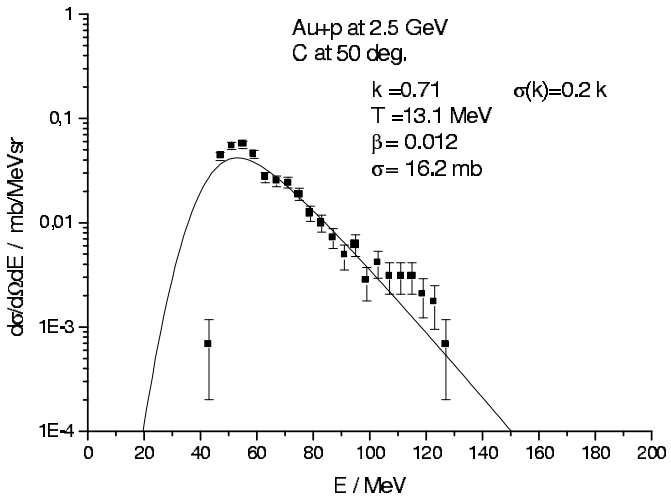

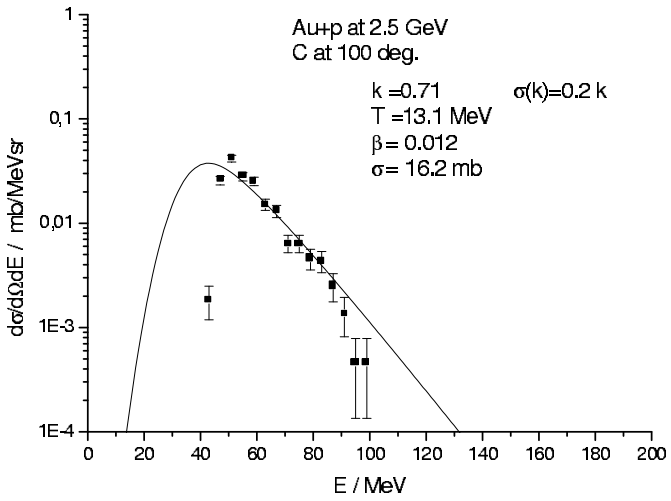

Figure 7.17: Same as Fig.7.5 but for carbon.

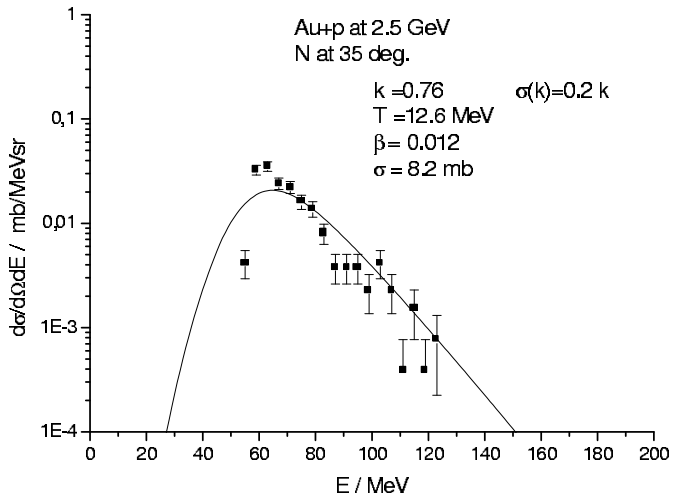

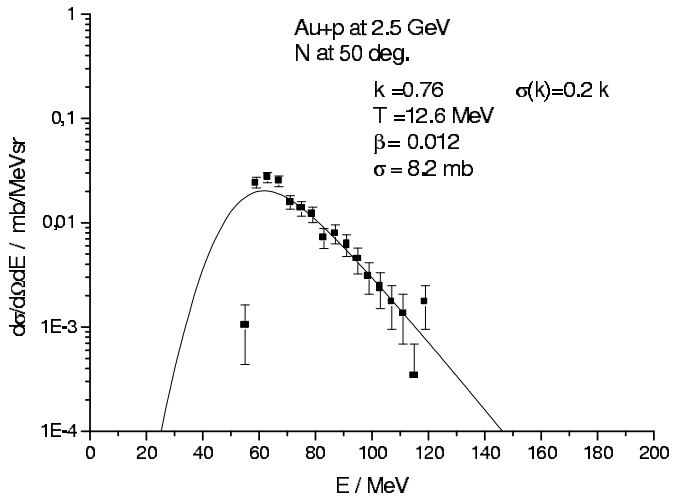

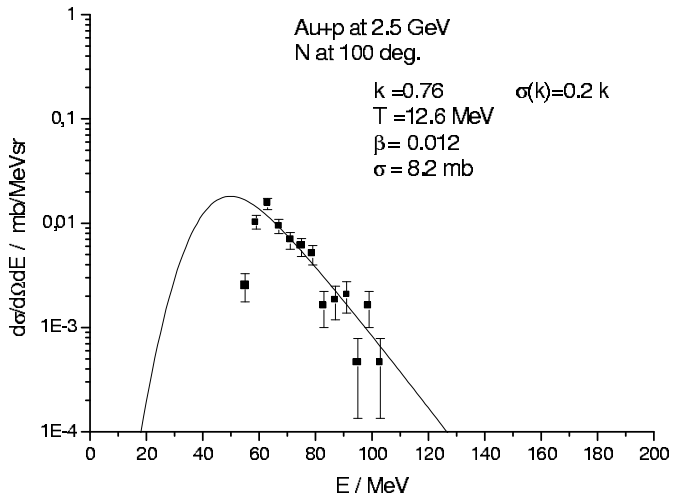

Figure 7.18: Same as Fig.7.5 but for nitrogen.

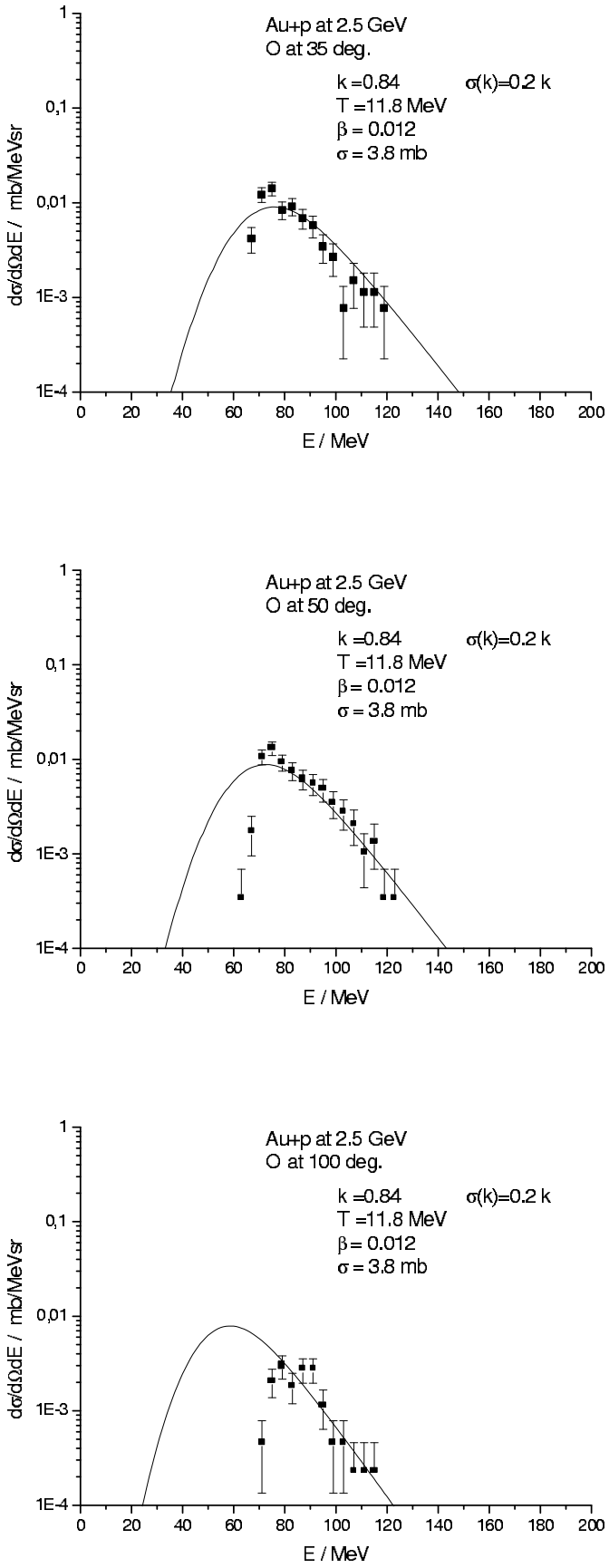

Figure 7.19: Same as Fig.7.5 but for oxygen.

It turned out that the evaporation cross section σ_1 deduced from the phenomenological method and the cross section σ_{GEM} extracted from the GEM model for ^{4}He, ^{7}Li, and ^{11}B agree almost perfectly. In the case of ^{3}He, ^{6}Li, and ^{8}Li the σ_1 is approximately 30 % smaller than σ_{GEM} whereas the difference increases for other Be and B isotopes (σ_1 is 2 - 4 times smaller than σ_{GEM}). Therefore, we can conclude that the contribution of the evaporation may be obtained with comparable accuracy – at least for the most abundant particles (He and Li) – by the GEM calculations or by application of the phenomenological formula to the experimental data . This is confirmed by comparison of sum of evaporation cross sections for all observed particles deduced from the phenomenological method and the sum of evaporation cross section calculated with the GEM model. Both sums are nearly the same; 2187 mb and 2080 mb, respectively.

The sum of the total cross section $\sigma_{tot} = \sum\sigma_1 + \sum\sigma_2$ of both, low and high energy contributions listed in the table 7.1 is equal 3144 mb and thus it allows to conclude that in average about 70% ($\sum\sigma_1/\sigma_{tot}$) of particles are evaporated from the compound nucleus and 30% ($\sum\sigma_2/\sigma_{tot}$) are due to other reaction mechanism. For ^{4}He and lithium isotopes, the contribution of the fast source is rather small ($\sigma_2/(\sigma_1+\sigma_2)$ is 16 %, 23 % and 18 % for ^{4}He, ^{6}Li and ^{7}Li, respectively) thus the contribution of the slow source is dominant. For ^{8}Li, the slow source fit is good enough to reproduce the all energy spectra of the fragments. In contrast, for beryllium and boron isotopes, which are less abundant than He and Li, the contribution of the fast source is dominant (75% for beryllium and 72% for boron). The low energy cut in C, N, and O spectra prohibits application of two sources in the phenomenological analysis and thus parameters of only one ”effective” source could be extracted.

It is interesting to note that mechanism of emission of ^{3}He and ^{4}He particles differs significantly. This may be concluded from the large difference in the relative contribution of the evaporation to the reaction cross section (32 % for ^{3}He and 84 % for ^{4}He) as well as from the fact that the cross section σ_1 corresponding to the contribution of the compound nucleus mechanism is seven times larger in the absolute scale for the ^{4}He than for the ^{3}He.

The temperatures corresponding to low energy component of the spectra differ strongly from temperatures attributed to the high energy component. For example, T_1 is of order of 8 - 9 MeV for He and Li ejectiles whereas the temperature T_2 is of order of 27 MeV. The estimation of the temperature of the compound nucleus made by Goldhaber [85] and Gelbke [86], which assumed that the temperature is related to the Fermi momentum p_f of the decaying nucleus shows that the temperature may be extracted from the equation

$$T = p_f^2/(5m_o) \tag{7.3}$$

where m_o is the nucleon mass. Using a Fermi momentum of 200 MeV/c the calculated temperature appears to be equal T=8.6 MeV, which is very close to the value of the temperature T_1 found in our analysis for He and Li particles.

The temperature T_2 of the fast source shows a decrease with increasing A_f of the detected fragment. This decrease is presented in the Fig. 7.20 in which also the linear trend of the temperature variation is depicted (solid line). It can be seen that the linear trend is a reasonably good approximation of the temperature dependence on the mass number of the fragment (correlation coefficient $R = -0.8$).

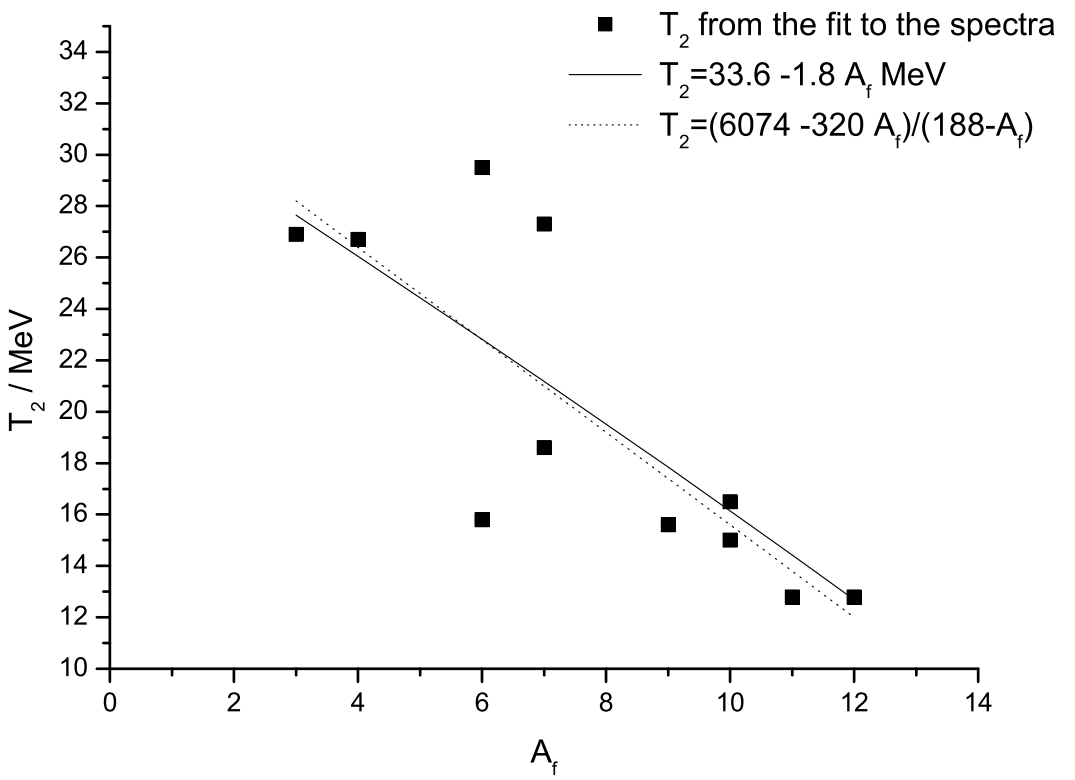

Figure 7.20: Dependence of the temperature T_2 of the fast emitting source on the mass number of the fragment A_f. The full squares are results obtained from the fit to the spectra, the solid line is the linear trend according to equation (7.4) whereas the dotted line is the quasi-linear trend evaluated with the equation (7.5) and the $T_0 = 32.3$ MeV, $A_R = 19$.

Such a variation of the temperature was observed earlier by Hirsch et al. [65] for p+Kr and p+Xe collisions and was interpreted as indication of necessity to introduce the recoil correction $\nu \equiv A_R/(A_R - A_f)$ to the energy of the ejectile (A_R is the mass number of the remnant nucleus emitting the fragment of the mass number A_f). Since this correction influences the formula mainly by multiplication of the energy in the argument of the exponential function $exp\{-(E \cdot \nu - kB)/T\}$ it manifests itself as dividing the fitted value of the temperature by ν and thus it introduces the observed linear trend of the $T(A_f)$ dependence:

$$T(A_f) = T_0 \left(1 - \frac{A_f}{A_R}\right), \tag{7.4}$$

where T_0 is the recoil corrected temperature of the remnant nucleus. The knowledge of the parameters of the line $T(A_f) = T_0 - (T_0/A_R)A_f$ allows to extract the corrected temperature T_0 and the mass of the decaying remnant A_R. In the case of investigations of p+Xe and p+Kr systems the T_0 was equal to 15 MeV and 14 MeV, and remnant mass number A_R was equal to 110 and 75 for Xe and Kr targets, respectively [65].

In our analysis the recoil correction has been inserted into the formula describing the energy spectra and their angular dependence $\frac{d\sigma}{dEd\Omega}(E,\theta)$ before performing the fits, thus the above explanation cannot be automatically accepted. However, the recoil correction was evaluated with the remnant mass number equal to 188 as derived from BUU calculations of the fast stage of the reaction. Therefore, it may happen that using the proper remnant mass will explain the observed linear dependence of the temperature on the mass of the fragment A_f. To check it we should write the observed temperature, which we denote by T in the following way:

$$T = \frac{\nu}{\nu_0} T_0$$

where

$$\nu = \frac{188}{188 - A_f}$$
$$\nu_0 = \frac{A_R}{A_R - A_f}$$

and T_0 is the recoil corrected temperature. Then we obtain the following dependence of the fitted temperature T on the mass number of the fragment A_f:

$$T = \left(\frac{188 T_0}{188 - A_f}\right) - \left(\frac{188 T_0}{188 - A_f}\right)\frac{A_f}{A_R} \tag{7.5}$$

This formula gives an approximate linear dependence if A_R is a constant and $A_R \ll 188$ because then the coefficients containing starting value of the remnant, i.e. 188, change only about 7% when we change the fragment mass in the studied range. Thus they are approximately constant whereas the factor $1 - \frac{A_f}{A_R}$ can vary much stronger (if $A_R \ll 188$).

Taking values of the parameters of the linear trend in the figure 7.20 we obtain that the remnant mass A_R should be approximately equal to 19. Using this value and the formula (7.5) listed above we obtain the approximately linear dependence of $T(A_f)$ presented as dotted line in the Fig. 7.20. Thus, the observed dependence of the temperature on the mass of the fragments does not contradict the assumption of the same remnant nucleus of the mass $A_R \approx 19$ and recoil corrected temperature $T_0 \approx 32.3$ MeV for all IMF's with masses up to $A_f = 12$.

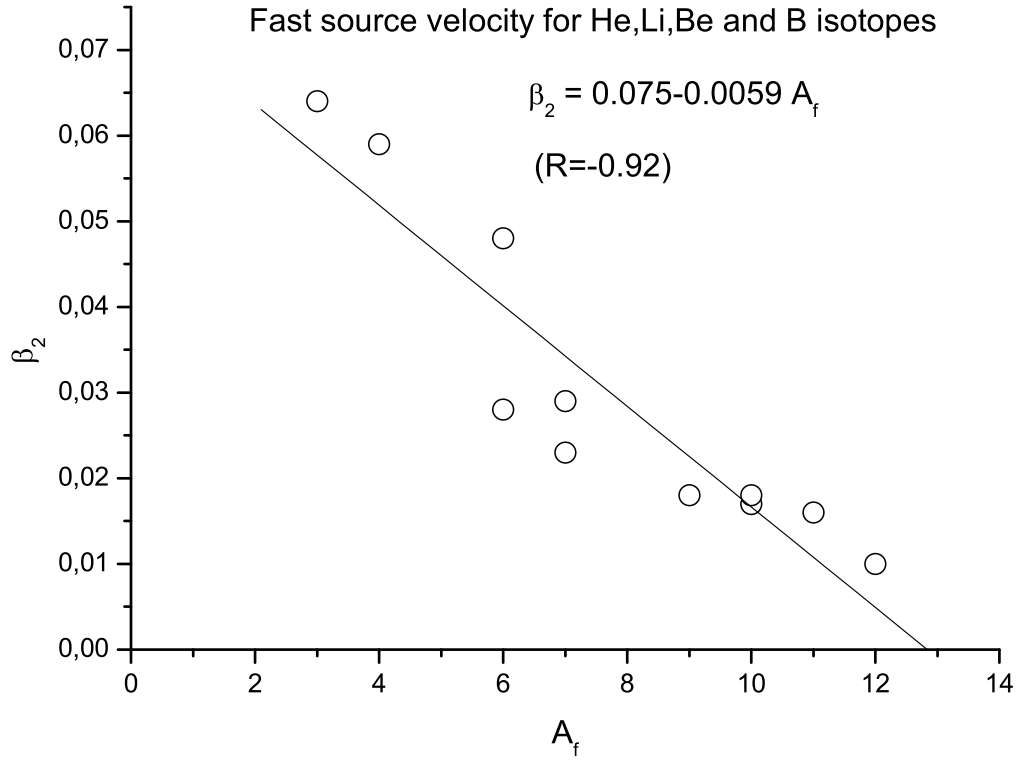

Figure 7.21: Dependence of the velocity β_2 of the fast emitting source on the mass number of the fragment A_f. The dots are results obtained from the fit to the spectra, the solid line is the linear trend. The correlation coefficient for this fit is equal to -0.92 showing that linear approximation is reasonable.

Comparing this with results of Hirsch et al. for Xe+p and Kr+p we see two distinct differences: (i) the mass 19 of the remnant nucleus in our case, i.e. for Au+p, is several times smaller than those for Kr (75) and Xe (110), (ii) the recoil corrected temperature is two times larger in our case (32.3 MeV) than for Kr (14 MeV) and Xe (15 MeV).

The other effect which was not observed for Kr and Xe is much larger velocity of the fast source ($\beta_2 = 0.03 - 0.06$) for Au+p than for Kr+p ($\beta = 0.007$) and Xe+p ($\beta = 0.002$). Furthermore, we observe a monotonic decrease of the β_2 with the mass number of the fragment A_f as it is shown in the Fig. 7.21, whereas the velocity of the source was independent of the fragment mass for Kr+p and Xe+p. It should be noted, that the momentum conservation puts constraints on velocity of the emitting source. For example, if we assume that the proton impinging on the target nucleus transfers the full its momentum to the nucleus than – in our case of Au+p – the source velocity cannot be larger than $\beta_2 \approx 0.018$. Since we observe much larger velocities as e.g. 0.064 for ^{3}He or 0.059 for ^{4}He the source emitting these particles must be much lighter than the target nucleus. Of course, higher velocity corresponds to lighter source. The explicit dependence of the source velocity β_2 on the fragment mass A_f shown in the Fig. 7.21 seems to indicate that different fragments are emitted from sources of the different mass.

This conclusion contradicts the earlier conclusion extracted from quasi-linear variation of the fast source temperature T_2 with the mass of the fragment A_f. However, the large spread of the temperature values around the linear trend indicates that there is a room for the spread of the mass of the remnant nucleus around value of 19. Furthermore, it should be taken into consideration that the results of Hirsch et al. for Kr+p and Xe+p were obtained for heavier fragments than these which we analyze in the present work, i.e. our consideration are limited to He – B fragments, whereas those of Hirsch et al. concern fragments of mass $A_f = 8 - 28$. We see for carbon, nitrogen and oxygen fragments (which were not mass identified) that velocity of the source emitting these fragments is practically the same ($\beta = 0.012$) and the temperature is also very similar ($T = 12 - 13$ MeV) for all the fragments and these values are much closer to observation of Hirsch et al. than values obtained for lighter fragments He – B.

The success of the fits performed within the phenomenological model of two emitting sources and reasonable values for the fitted parameters support the assumption of isotropic fragment emission from a moving sources. This suggests that for the fast emitting source the memory of the entrance channel is lost to large extend (with exception of the kinematic constraints) similarly as it is the case for the compound nucleus mechanism contributing to the slow source emission. The good reproduction of the data enables to describe quantitatively the high energy part of the energy spectra of particle with Z$\geq$2, what was not possible with the GEM model.

Finally, the equation 3.14 gives the total fragment production cross section for each measured particle. This enables us to study dependence of the cross section on the mass and charge of the detected fragments as it will be discussed in the following section.

7.3 Fisher's droplet model

The observation of a power law dependence (see section 3.3), $Y(Z_f) \sim Z_f^{-\tau}$ or $Y(A_f) \sim A_f^{-\tau}$ for the produced fragments in proton induced collisions leads to the idea of a liquid-gas phase transition in nuclear matter. The particular value of $\tau \sim 2.3 - 2.6$ is treated as a signature for the presence of the phase transition.

To check, whether our data confirm the power low dependence of the cross sections and to find value of the exponent τ we prepared the following figures: (i) the $\sigma(Z_f)$ dependence for all fragments from He to O summing the contributions from slow (σ_1) and fast (σ_2) sources , (ii) the same for $\sigma(A_f)$ dependence, (iii) $\sigma(A_f)$ dependence for fragments emitted by the slow source, and (iv) $\sigma(A_f)$ dependence for fragments emitted by the fast source.

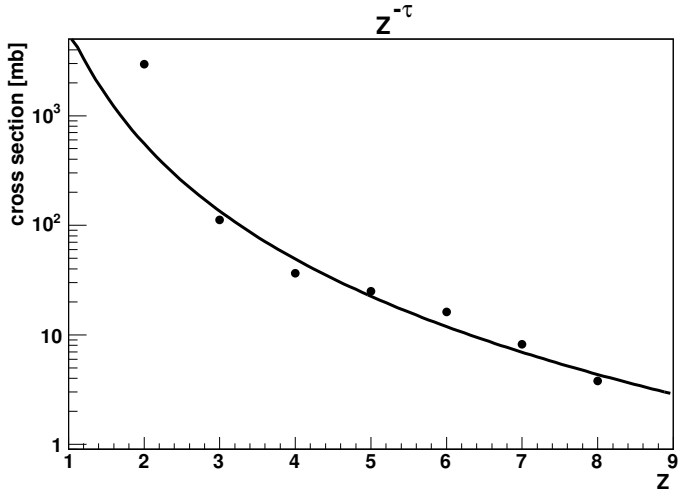

Figure 7.22: The cross section for emission of fragment of charge Z_f (sum of contributions from the slow and the fast emitting sources) as a function of the fragment charge Z_f (dots). The line presents fit of the power function $\sigma(Z_f) \sim Z_f^{-\tau}$. The exponent $\tau = 3.5 \pm 0.7$.

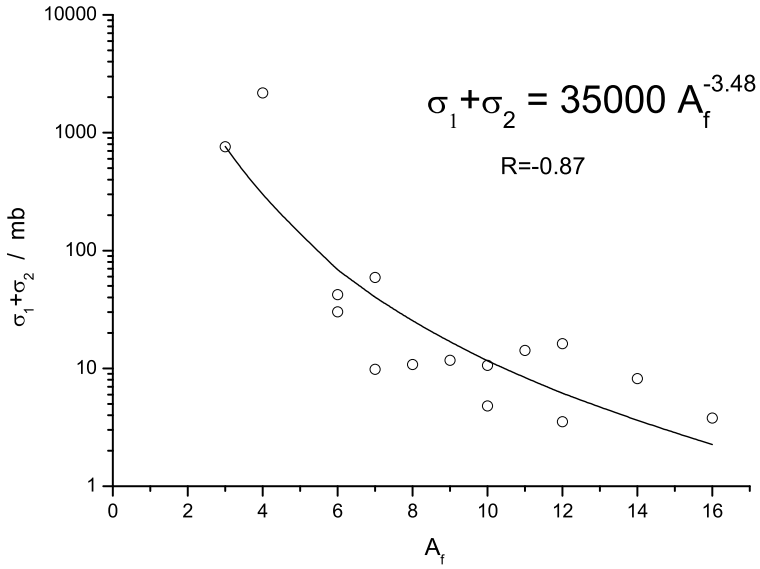

Figure 7.23: Same as Fig. 7.22 but concerning the dependence of the cross section on the mass of the fragments $\sigma(A_f) \sim A_f^{-\tau}$ (dots). The line presents fit of the power function with the exponent $\tau = 3.5 \pm 0.5$.

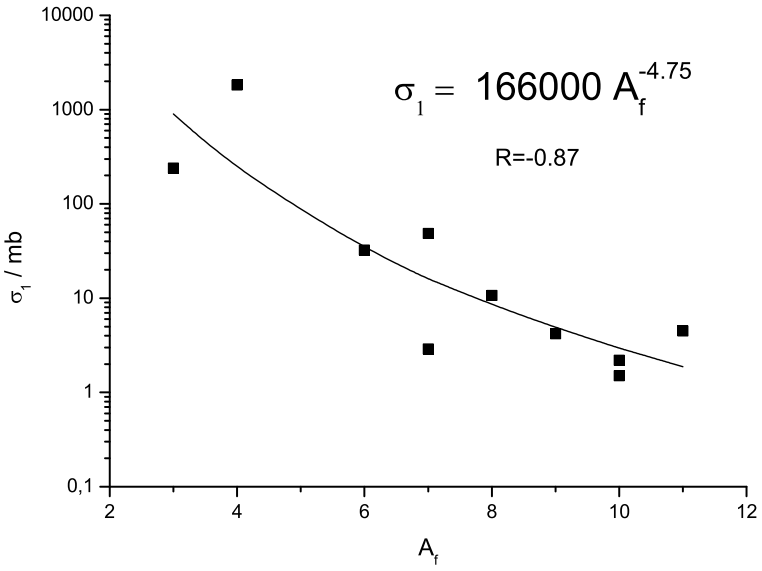

Figure 7.24: Same as Fig. 7.22 but concerning the dependence of the cross section on the mass of the fragments $\sigma(A_f) \sim A_f^{-\tau}$ for slow emitting source (full squares). The line presents fit of the power function with the exponent $\tau = 4.8 \pm 1.0$.

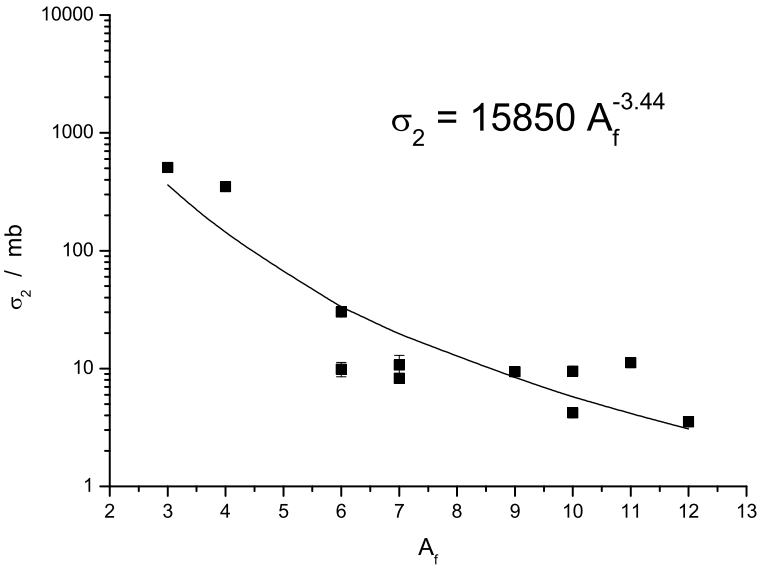

Figure 7.25: Same as 7.22 but concerning the dependence of the cross section on the mass of the fragments $\sigma(A_f) \sim A_f^{-\tau}$ for fast emitting source (full squares). The line presents fit of the power function with the exponent $\tau = 3.4 \pm 0.5$.

As it was expected, the τ exponent found from the $\sigma(Z_f)$ dependence is the same as found from the $\sigma(A_f)$ dependence, i.e. it is equal to 3.5, what is larger than the critical value of 2.3 - 2.6. This means that our data do not show presence of the nuclear phase transition in the Au+p system at $T_p = 2.5$ GeV.
To compare our exponent with the literature results it is useful to present it on the plot showing dependence of the exponent on the temperature. It should be pointed out, that our results indicate two different temperatures for the slow and the fast emitting source. Therefore it is not clear which of the temperatures should be taken for presentation of the exponent as a function of the nuclear temperature. From the Figs. 7.24 and 7.25 it is evident that the extracted exponents are different for the slow source ($\tau = 4.8 \pm 1.0$) and for the fast source ($\tau = 3.4 \pm 0.5$). However, the value obtained for the fast source is almost exactly equal to the exponent extracted from the sum of both contributions.

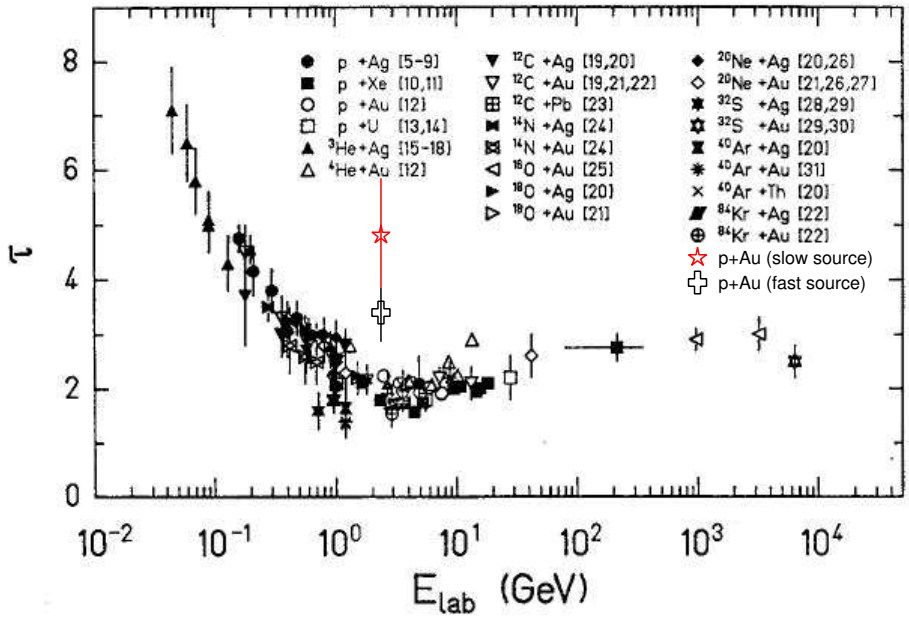

Figure 7.26: The apparent exponent τ of the power law fit to the fragment distributions as a function of the beam energy for a variety of reactions. The reactions and the references are indicated in [87]. Fig. adapted from [87].

In Fig. 7.26 the dependence of the apparent exponent τ with the beam energy of the projectile is shown. This figure shows the decrease of τ with the increasing beam energy up to 2-5 GeV where the value of τ remains constant and is close to 2. This saturation reflects the idea of limiting fragmentation. The most surprising is that this dependence is similar for all target (from C to U). If we take the τ=4.8 as found for the slow emitting source, then our τ exponent is clearly larger than these shown in the figure 7.26 at energy 2.5 GeV. In the Fig. 7.26 the data points for the reaction p+^{197}Au are visible in the energy range between 2.5 and 7.5 GeV obtained by [88]. Looking only on the figure 7.27 showing the value of τ (open circles) for the p+^{197}Au the value are decreasing from 2.2 to 1.9. The value corresponding to the proton energy 2.5 GeV (τ=2.2$\pm$0.1) is lower in

comparison to our value τ for the slow source or for the fast source. Note that the parameter τ from Avdeichikov data [88] is extracted taking into account the particles with $3 \leq Z \leq 12$ while in our case the Z distribution takes lighter particles starting from helium up to oxygen. The choice of the Z-range can also modify the τ value. Looking more in details in Fig.7.27 it seems that at proton energy 5 GeV on the reaction p+^{197}Au the nuclear phase transition may be observed. We can conclude that in proton induced reaction on gold target at proton energy 2.5 GeV, the nuclear phase transition is still not visible.

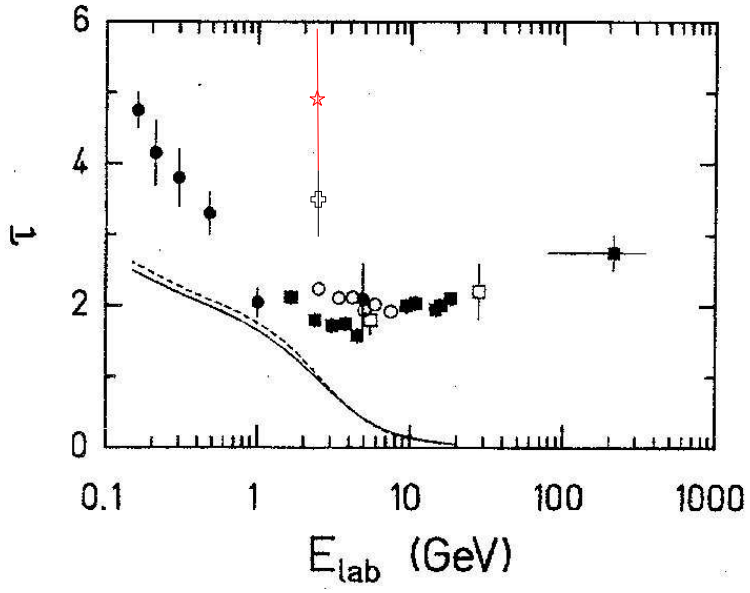

Figure 7.27: The apparent exponent τ for proton induced reactions on Ag (closed circles), Xe (full squares), Au (open circles) and U targets (open squares). Our data are shown for the slow source (red star) and the fast source (open cross). Fig. adapted from [89].

In the ref. [34], for proton induced reaction on gold target with proton energy equal 8.1 GeV, a critical temperature of T_c=20±3 MeV was found by data analysis with a statistical multifragmentation model (SMM). Avdeyev et al. [90] have shown the fragment charge distributions for proton induced reaction on gold target with proton energy 2.16, 3.6 and 8.1 GeV respectively and deduced from these distributions the values of τ equal 2.17±0.08, 1.90±0.06 and 1.93±0.06, respectively. The comparison between the apparent exponent τ obtained from our data (τ=3.5±0.7) and this from the Avdeyev data obtained at proton energy 2.16 GeV (τ=2.17±0.08) is almost compatible within the error bars indicated.

Chapter 8

Summary and discussion

The experiment was performed at the internal beam of the COSY synchrotron in order to measure the double differential cross section $d^2\sigma/dEd\Omega$ for light charged particles (^{3}He, ^{4}He and ^{6}He) and intermediate mass fragments (Li, Be, B, C, N and O) emitted from p+^{197}Au collisions at 2.5 GeV. The light particles and IMFs with $Z \leq 5$ were Z and A identified whereas heavier IMFs with $6 \leq Z \leq 8$ only Z-identified.

The spectra of ^{3,4,6}He, ^{6,7,8}Li, ^{7,9,10}Be, ^{10,11,12}B as well as C, N, and O were measured at three scattering angles (35^o, 50^o and 100^o in the laboratory system) in the broad energy range (from $\sim$ 20 MeV to $\sim$ 200 MeV).

The shape of the spectra of He and Li isotopes gives evidence for existence of two components of the Maxwell-Boltzmann shape. The low energy component which slopes steeply and the high energy component with the smaller slope. It is commonly believed (see e.g. review articles [91, 92]), that the low energy part of the spectra for light and intermediate mass fragments is associated with the evaporation of the particles and the high energy part corresponds to some other, non-equilibrium reaction mechanism.

The spectra of heavier ejectiles do not exhibit such a pronounced character. They seem – on the first view – to be consistent with the presence of the single component of the Maxwell-Boltzmann shape. However, the slope of these spectra is intermediate between slopes of the low energy and high energy components of the He and Li spectra. This might indicate that the emission of IMF's heavier than Li is due to mixture of evaporation and pre-equilibrium processes. Moreover, the shape of the high energy tails of the spectra is angle dependent (the slope increases with the angle) whereas the shape of evaporation spectra is expected to be almost angle independent. This suggests that the high energy tails of the spectra for heavier IMF's are mainly populated by the emission from the excited nucleus moving distinctly faster than the compound nucleus.

The analysis of the data with the Generalized Evaporation Model (GEM) of S. Furihata [47] coupled to intranuclear cascade model (INCL4 program [56]) confirmed that the low energy component of the He and Li spectra can be well reproduced by the evaporation, however, a significant contribution of non-evaporative mechanism is present in the high energy part of the spectra. Furthermore, the GEM contribution to the spectra of heavier ions (Be, B, C, N, and O) leaves room for presence of high energy component, which could not be identified easily without comparison with these calculations.

Since the generalized evaporation model was not able to describe the high energy part of the experimental spectra a phenomenological analysis has been performed in which parameters of two isotropically emitting sources, moving with different
velocities along the beam direction were fitted to reproduce the experimental data. It turned out that low energy component of the He and Li spectra, which could be well distinguished in the

experimental data, is reproduced by contribution from slowly moving source with the angle and energy integrated cross section consistent with that predicted by GEM. Also compatible with the velocity of this slowly moving source is the momentum transfer caused by incident protons as calculated by INCL4.2. For the reaction under consideration the mean velocity of the target-like source, parallel to the beam direction has been found to be $\beta = 0.0036$.

It was not possible to fit two source contributions to the spectra of heavier ejectiles without putting some constraints to the parameters of the slowly moving source. Therefore, the velocity and the slope parameter of the slowly moving source have been fixed at values found for He and Li ions. Then the automatic search of the relative contribution of this source could be made together with fit of the parameters of the fast moving source. Comparison of results from GEM and from the phenomenological fit of two moving sources showed that both models lead to consistent results for the evaporative contribution in the limits of errors. Furthermore, this analysis enabled us to extract contributions of both mechanisms to the investigated reaction.

For ^{4}He and lithium isotopes, the contribution of the fast source is rather small (σ_1/σ_{tot} varies in the range of 16% – 23%), however, for ^{3}He, for beryllium and boron isotopes, the contribution of the fast source is dominant (68% – 75%). The low energy cut in C, N, and O spectra prohibited application of two sources in the phenomenological analysis and thus parameters of only one "effective" source could be extracted.

The dependence of the temperature (slope) parameter of the fast moving source on the mass of the fragments points to necessity of introducing the recoil correction to the spectra and allows to extract the mass of the source. It turned out that this mass is small (around 19 nucleons) whereas the recoil corrected value of the temperature parameter is large (32.3 MeV). Such a small mass of the source is consistent with the observation that the velocity of the fast source for He, Li and ^{7}Be ejectiles is larger than that allowed by the momentum conservation for the heavy (compound nucleus like) source. The recoil correction for slow source is not important because mass of the compound nucleus is at least one order of magnitude larger than the mass of observed ejectiles. It should be emphasized that these conclusions are model independent since they are based only on kinematical considerations.

The fact that the observed spectra can be described by presence of two isotropically emitting sources might suggest a statistical origin for the nonevaporative component. However, this interpretation should be taken with a caution especially that some behavior of the parameters has no clear explanation. This e.g. concerns the striking dependence of the velocity of the fast source on the mass of the emitted fragment (see β_2—A_f anticorrelation in Fig. 7.21).

The dependence of the energy and angle integrated cross sections extracted from the analysis on the mass of the fragments can be described by the power law ($A^{-\tau}$ dependence), however, the obtained value of the exponent $\tau \approx 3.5$ is to large to be treated as indication of the nuclear phase transition at the actual proton energy. Thus, the appropriate microscopic description of the reaction mechanism observed in our experiment is still lacking.

Results of the present experiment agree well with previously published investigations. For example presence of two mechanisms of IMF's production (evaporation and non-equilibrium process) was observed in investigations of proton induced reactions on silver at energies 210, 300, 480 MeV [93, 94], at 5.0 GeV [95], and 5.5 GeV [66], as well as on U at 5.0 GeV [95].

The mass of the emitting source derived from the temperature dependence on the mass of the emitted fragment gives in our case rather small value of about 19 nucleons. The heavier sources were observed in other investigations i.e. the mass of the source was equal to 43 nucleons for p+Ag at E_p=0.48 GeV [93], 77 nucleons for Kr ([65]) and about 110 nucleons for Xe [65] at $80 \leq E_p \leq 350$ GeV. It should be, however, pointed out that these conclusions were based on investigation of spectra for fragments with mass larger than 7 for Kr and Xe and for fragments heavier than B for

Ag. If the investigation of the temperature dependence on the mass of the fragments is limited to the lightest IMF's (Li, Be, B) for p+Ag [93] than the mass of the source at E_p=0.48 GeV is 23 nucleons – very close to our value obtained also for light ejectiles (He-O).

The contribution of the non-evaporative processes to the spectra observed for the p+Ag reactions at 0.48 GeV [93] is very similar to ours. The authors claim that for fragments heavier than ^{4}He the contribution of the non-evaporative mechanism increases with the mass of the fragments and achieves for IMF's with mass in vicinity of 20 the value larger than 90 %. Our results for Au+p at 2.5 GeV lead to very similar conclusions, i.e. the contribution of the non-evaporative mechanism become dominant for heavier fragments (Li - B).

The clarification of details of the mechanism responsible for the observed reactions needs further investigations. These may be illustrated on the example of the ^{3}He and ^{4}He production for which the spectra exhibit very distinct qualitative difference observed in our experiment and also quoted by other authors. The observation of different contributions of evaporation mechanism to ^{3}He and ^{4}He spectra leads to conclusion that the reaction mechanism is different for these two particles. Barlow et al. [96] suggest that ^{3}He and ^{4}He are emitted in different instants of the reaction. Some similarity found between high energy parts of the proton, deuteron, triton and ^{3}He spectra suggests that the ^{3}He particles are produced by pick-up. The simple pick-up model (coalescence model) assumes that a proton picks up a neutron forming a deuteron and deuteron subsequently picks up another proton forming ^{3}He particle. One more pickup process produces ^{4}He particles. This mechanism can explain high energy part of the spectra of light particles [29], e.g. it was observed [91] that for large targets more ^{4}He particles are formed because it is more probable for ^{3}He to pick up a neutron. However, this mechanism is not able to reproduce low energy part of the spectra, where the evaporation dominates. In this case the evaporation mechanism clearly favors the low energy alpha - particles in comparison to ^{3}He which are much more weakly bound than ^{4}He, thus their evaporation is less probable.

Extension of the pick up model to intermediate mass fragments was not successful up to now to reproduce the observed properties of the spectra, therefore some other reaction mechanism has to be involved. Furthermore, the mechanism which is able to reproduce the specific nuclear reactions may be not efficient in description of other reactions. For example, the droplet model and postulated nuclear phase transition, which was successfully applied for explanation of high energy (1 –19 GeV) proton interaction with Xe [97], [98] and Kr [65] cannot reproduce our data where we do not see evidence for the nuclear phase transition. Thus the further investigations, involving the energy as well as the target dependence of the proton induced reactions seem to be very important for understanding of the reaction mechanism of the high energy proton – nucleus collisions.

In the present thesis new experimental data of double differential cross sections $d\sigma/d\Omega dE$ were analyzed in the frame of the Generalized Evaporation Model [47] and with the phenomenological model of two moving sources which emit isotropically the observed particles in their rest frame. It turned out that both methods gave equivalent, consistent results for description of the evaporative contribution to the cross sections. This is interesting to point out that it was the cross check of both models, not only for total cross sections but for the first time also for the energy spectra. The evaporation of heavy IMF's is usually not taken into account but here it was very fruitful because it helped to separate the non-evaporative contribution. The contribution of the non-evaporative mechanism has been determined for all the emitted particles and it was found to increase with the mass of the ejectile achieving value up to 75% for Be and B particles. The mechanism of this process was described in phenomenological way assuming that the particles are emitted from a light ($A \sim 20$) , hot ($T \sim 32$ MeV) source moving with surprisingly high velocity (order of magnitude faster than the compound nucleus). It is striking that very good description of the energy and angular dependence of the differential cross sections was obtained based on the assumption of

an isotropic emission of the particles from this source. Moreover, the information on the properties of the fast source has been obtained from model independent – kinematical considerations.
To get the final goal of creation of a model for the reaction mechanism it would be desirable to obtain more experimental information on both, the inclusive and coincidence cross sections involving the intermediate mass fragments emitted from the fast source.

Appendix A

Interaction of particles with matter and methods of particle identification

A.1 Bethe-Bloch formula

Charged particles passing through matter lose energy by ionization. The energy loss can be divided into two components: nuclear stopping (energy loss caused by the medium's nuclei) and electronic stopping (energy loss caused by the medium's light electrons).
The stopping power is given by the Bethe-Bloch [100] equation:

$$\frac{dE}{dx} = \frac{4\pi e^4 Z_2}{m_e v^2} Z_1^2 \Big[ln\frac{2m_e v^2}{I} - ln(1-\beta^2) - \beta^2 - \frac{C}{Z_2} - \frac{\delta}{2} \Big] \tag{A.1}$$

Z_1	particle atomic number	Z_2	target atomic number
v	particle velocity	β	relative particle velocity
e	charge of an electron	m_e	mass of an electron
$\frac{C}{Z_2}$	shell correction term	$\frac{\delta}{2}$	density effect correction term
I	average excitation potential per electron		

The shell correction term $\frac{C}{Z_2}$ corrects the assumption that the ion velocity is much larger than the target electron velocity (up to a 6% correction to stopping powers [74]) and the density effect term $\frac{\delta}{2}$ corrects for polarization effects in the target.
At lower energies $\frac{C}{Z_2}$ corrections for tightly-bound atomic electrons and other effects must be made, and at higher energies radiative effects begin to be important.
At very high energies $\frac{\delta}{2}$ density effect corrections can be defined by:

$$\frac{\delta}{2} \rightarrow ln(\hbar\omega_p / I) + ln\beta\gamma - 1/2 \tag{A.2}$$

where $\hbar\omega_p$ is the plasma energy [101].
For the silicon telescope calibration we used the program SPAR [73] to reproduce exactly the characteristic hyperbola which is formed when ΔE is plotted versus E and the punch through given by the ΔE-E spectrum for each particle passing through the silicon detector.
Different approximation of electronic stopping (see Table A.1) which covers all energies is treated by SPAR.
For fast particles with velocities higher then the orbital velocities of electron, the Bethe-Bloch formula is to be used [102]. At lower velocities, inner electrons have velocities greater than particle

β region	Stopping Power	Remarks
$\beta > 0.04\ z^{2/3}$	$S_e(E) = \frac{4\pi e^4}{m_e c^2}\frac{z_p^{*2}}{\beta^2}\left(ln\left(\frac{2m_e c^2\beta^2\gamma^2}{I}\right) - \beta^2 - \frac{\delta}{2}\right)$	only electronic stopping
$0.0046\ z^{1/3} < \beta < 0.04\ z^{2/3}$	$S_e(E)$ with $z_i^* = z_i(1 - e^{(-125\beta z_i^{-2/3})})$	effective charge of the ions reduced
$\beta < 0.0046\ z^{1/3}$ =	$S_{ij}^n = \sum_j \frac{A_j N_j}{N_a}\frac{(d\varepsilon/d\rho)_{ij}}{G_{ij}}$	Lindhard's theory

Table A.1: Formulas used in SPAR. Where $\gamma = \frac{1}{\sqrt{1-\beta^2}}$, z_i^* is the particle atomic number , z_i^* is the effective charge of the ions reduced and z_i charge of the ions.

velocity, and therefore do not contribute to the energy loss. This regime was modeled by Lindhard and Scharff [103].
The orbital velocity of electron is defined as:

$$v = \frac{Ze^2}{2nh\varepsilon_0} \tag{A.3}$$

where Z is the number of protons circled by a single electron, e is electron charge, n is the principal quantum number which characterizes the size and the energy of the considered orbital, h is the Planck constant and ε_0 is the permittivity of free space equal to $8.854{\cdot}10^{-12}$ Fm^{-1}. For an hydrogen atom, the orbital velocity of its electron in its ground state (n=1) according to the equ. (A.3) is $2.188{\cdot}10^6$ m/sec.

A.2 ΔE-E techniques for charged particle identification

In a silicon telescope described in section 4.2.2, one of the quantities available to identify particles penetrating such telescope is the energy deposited in the various silicon detectors (of known thicknesses) in the stack at least if the particle is stopped inside the stack following.
The description gives a general idea of the method. Using for example two silicons detectors of known thicknesses, a particle crossing detector 1 and being stopped in detector 2 will deposit energy ΔE (energy loss per unit pathlength) in the detector1 and energy E in the detector 2. The total particle energy is approximated by E, the energy deposited in the detector 2 because the charged particles tend to lose most of their energy near the end of their range. When the two quantities are multiplied together, the result is approximately proportional to Z^2*M, where Z and M are the particle charge and mass. The two quantities can be presented like a histogram ΔE versus E (see Fig. 4.12).
Each charged particle of special kind detected in a first and a second silicon detector is characterized by an hyperbola. At the end of the hyperbola is the so called "punch through", this means that the particle is not stopped in this pair of detectors and had enough energy to leave the second detector.
Each hyperbola defines the kind of particles not only from the mass but also from the charge.
On the other hand, such effect like the existence of "dead layers" in some silicon detectors can degrade the mass resolution because the energy ΔE signal does not include the energy deposited in the dead layer. If the dead layer thickness is known the error can be corrected. Two others effects

called pulse height defect (PHD) [104] and plasma delay [105] may cause fluctuations in the E signal as well as causing the signal to be non-linear [106].
The PHD effect is defined as the difference between the detector response to a heavy ion and to an alpha particle of the same energy.
The factors contributing to the PHD effect are:

- loss of free electrons by recombination of ion pairs
- loss of energy in low-energy non-ionizing collisions with lattice atoms
- loss of energy in the Au entrance window and underlying surface dead layer
- loss of free electrons at "trapping sites" such as lattice defects or impurities

The PHD of a surface barrier detector for fission fragments was estimated by Kobayashi [107]. The pulse height loss versus the fission fragment energy spectrum in the measurement of ^{235}U target irradiated by a thermal neutron and measured by a silicon surface barrier detector is shown in the Fig. A.1. This reaction has the typical behaviour of asymmetric fission. These plot shows that the PHD of the heavy fragment group is generally larger than for the lighter fission fragments except of the light fragment group at highest kinetic energies. This fact suggests that the PHD depends on the mass and velocity of the respective fragments.

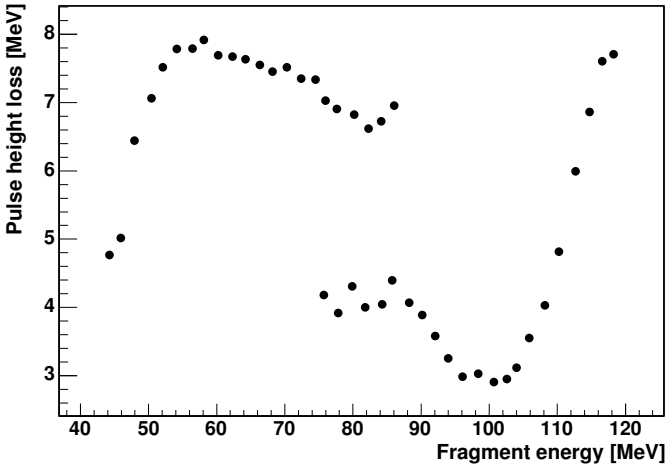

Figure A.1: Pulse height loss as a function of fragment energy for ^{235}U irradiated by a thermal neutron beam (Fig. adapted from [107]).

When the timing signal obtained from a silicon detector does not represent the correct time of arrival of an ion in the detector but it is too late, the effect is called plasma delay. The factor which contributes to this effect is the creation of a high conductivity plasma along the particle trajectory. This plasma disturbs for some time the internal electric field and therefore retard the charge collection. During this process there is a long time for electrons to recombine. Therefore the PHD is caused by the reduced number of electrons.

Acknowledgements

This work relies on the help of several persons to whom I would like to express my gratitude in the following lines.
First of all, I would like to thank Prof. D. Filges for giving me the opportunity to make my PhD thesis in the Institute of Nuclear Physics of Juelich Research Center.
I would like to express my deepest appreciation to my doctor father, Dr. F. Goldenbaum for his advice and encouragement. He gives me the chance to work on the PISA experiment and provides me to the understanding of the physical processes involved in the spallation reaction.
I am especially grateful to Prof. L. Jarczyk and Prof. B. Kamys, my professors of the Jagellonian University in Cracow with whom I have learned experimental nuclear physics, for their continuous interest, numerous and fruitful discussions. I thank them for their enormous patience and for all the precious time they dedicated to me.
Nearly everyone in the PISA collaboration and in the Institute of Nuclear Physics has contributed one way or another in this dissertation. I am indebted to the whole collaboration group members, and especially Dr. P. Kulessa and B. Piskor-Ignatowicz, they have introduced me the tuning of the PISA data acquisition system and electronics, A. Bubak and M. Wojciechowski to introduced me in the interface of the computer for data taking, Dr. K. Pysz who provides me to the technical and experimental aspects of the PISA detectors setup and Mr. DP. D. Protic for interesting discussion about silicon detectors. I thank as well the technical staff for providing construction and correction in the PISA setup, especially DI. N. Paul and Mr. H. Hadamek, the COSY staff for giving us a good beam quality during the experiment and Mr. L. Conin, Dr. U. Bechstedt and Mr. N. Dolfus for their fruitful collaboration in preparing the vacuum control system for the PISA experiment.
I would also like to thank my german colleagues for their support and for providing a team atmosphere in which I felt very comfortable. I would not have the strength to accomplish this work without the encouragement of the polish colleagues, who took care of me during the last and most difficult months of this PhD.
Finally, I would like to thank (*"vi ringraziu"*) my corsican friends to encourage me and my family for enabling me the possibility to study.
I dedicate this thesis to my mother who gives me the taste to science. I thanks her for her encouragement in the most difficult period and the interest in my work.

Bibliography

[1] K. Niita et al., Phys. Rev. C 52 (1995) 2620

[2] B.V. Jacak, D. Fox, and D. G. Westfall, Phys. Rev. C 31 (1985) 704

[3] J. Aichelin, J. Hüfner, and R. Ibarra, Phys. Rev. C 30 (1984) 107

[4] W. Bauer, D.R. Dean, U. Mosel, and U. Post, Phys. Lett. B 150 (1985) 53

[5] X. Campi, J. Desbois, and E. Lipparini, Nucl. Phys. A 428 (1984) 327c

[6] S. G. Mashnik, A. J. Sierk, K. K. Gudima, arXiv:nucl-th/0208048 v1 23 Aug 2002

[7] R. Michel, R. Bodemann, H. Busemann, R. Daunke, M. Gloris, H.-J. Lange, B. Klug, A. Krins, I. Leya, M. Luepke, S. Neumann, H. Reinhardt, M. Schnatz-Buettgen, U. Herpers, Th. Schiekel, F. Sudbrock, B. Holmqvist, H. Conde, P. Malmborg, M. Suter, B. Dittrich-Hanne, P.-W. Kubik, H.-A. Synal, D. Filges, Nucl. Instr. Methods B 129 (1997) 153-193

[8] S. B. Kaufman, E. P. Steinberg, Phys. Rev. C 22 (1980) 167

[9] J. Hudis, S. Katcoff, Phys. Rev. 180 (1969) 1122

[10] J. Hudis, S. Katcoff, Phys. Rev. C 13 (1976) 1961

[11] S. B. Kaufman, M. W. Weisfield, E. P. Steinberg, B. D. Wilkins, D. Henderson, Phys. Rev. C 14 (1976) 1121

[12] J. R. Cummings, W. R. Binns, T. L. Garrard, M. H. Israe1, J. Klarmann, E. C. Stone, and C. J. Waddington, Phys. Rev. C 42 (1990) 2530

[13] W.-C. Hsi, K. Kwiatkowski, G. Wang, D. S. Bracken, E. Cornell, D. S. Ginger, V. E. Viola, N. R. Yoder, R. G. Korteling, F. Gimeno-Nogures, E. Ramakrishnan, D. Rowland, S. J. Yenello, M. J. Huang, W. G. Lynch, M. B. Tsang, H. Xi, Y. Y. Chu, S. Gushue, L. P. Remsberg, K. B. Morley, H. Breuer, Phys. Rev. Lett. 79 (1997) 818

[14] C. J. Waddington, J. R. Cummings, B. S. Nilsen, and T. L. Garrard, Phys. Rev. C 61 (2000) 024910

[15] S. B. Kaufman, M. W. Weisfield, Phys. Rev. C 11 (1975) 1258

[16] K. H. Tanaka, Y. Yamanoi, H. Ochiishi, H. Akiyoshi, S. Kouda, H. Nakamura, S. Morinobu, Y. Tanaka, K.Kimura, T. Shibata, Y. Sugaya, K. Yasuda, H. Ito, T. Murakami, Nucl. Phys. A 583 (1995) 581

[17] L. P. Remsberg, D. G. Perry, Phys. Rev. Lett. 35 (1975) 361

[18] J. Pochodzalla, T. Mohlenkamp, T. Rubehn, A. Schuettauf, A. Woerner, E. Zude, M. Begeman-Blaich, Th. Blaich, H. Emling, A. Ferrero, C. Gross, G. Imme, G. J. Kunde, W. D. Kunze, V. Lindenstruth, U. Lynen, A. Moroni, W. F. J. Mueller, B. Ocker, G. Raciti, H. Sann, C. Schwartz, W. Seidel, W. Serfling, J. Stroth, W. Trautmann, A. Trzcinski, A. Tucholski, G. Verde, and B. Zwieglinski, Phys. Rev. Lett. 75 (1995) 1040

[19] J. Vervier et al., NuPECC Report, Nuclear Physics in Europe: Highlights and Opportunities (1997)

[20] J. R. Cummings, W. R. Binns, T. L. Garrard, M. H. Israel, J. Klarmann, E. C. Stone, and C. J. Waddington, Phys. Rev. C 42 (1990) 2508

[21] J. Benlliure, P. Armbruster, M. Bernas, A. Boudard, J. P. Dufour, T. Enqvist, R. Legrain, S. Leray, B. Mustapha, F. Rejmund, K.-H. Schmidt, C. Stephan, L. Tassan-Got, C. Volant, Nucl. Phys. A 683 (2001) 513-539

[22] J. Benlliure, P. Armbruster, M. Bernas, A. Boudard, T. Enqvist, R. Legrain, S. Leray, F. Rejmund, K.-H. Schmidt, C. Stephan, L. Tassan-Got, C. Volant, Nucl. Phys. A 700 (2002) 469-491

[23] F. Rejmund, B. Mustapha, P. Armbruster, J. Benlliure, M. Bernas, A. Boudard, J. P. Dufour, T. Enqvist, R. Legrain, S. Leray, K.-H. Schmidt, C. Stephan, J. Taieb, L. Tassangot, C. Volant, Nucl. Phys. A 683 (2001) 540-565

[24] M. N. Andronenko, L. N. Andronenko, W. Neubert, D. M. Seliverstov, Eur. Phys. J. A 8 (2000) 9-13

[25] A. A. Kotov, L. N. Andronenko, M. N. Andronenko, Y. I. Gusey, K. V. Lukashin, W. Neubert, D. M. Seliverstov, I. I. Strakovsky, L. A. Vaishnene, Nucl. Phys. A 583 (1995) 575c

[26] M. Enke, C.-M. Herbach, D. Hilscher, U. Jahnke, O. Schapiro, A. Letourneau, J. Galin, F. Goldenbaum, B. Lott, A. Peghaire, D. Filges, R.-D. Neef, K. Nuenighoff, N. Paul, H. Schaal, G. Sterzenbach, A. Tietze, L. Pienkowski, Nucl. Phys. A 657 (1999) 317-339

[27] X. Ledoux, H.G. Bohlen, J. Cugnon, H. Fuchs, J. Galin, B. Gatty, B. Gebauer, D. Guerreau, D. Hilscher, D. Jacquet, U. Jahnke, M. Josset, S. Leray, B. Lott, M. Morjean, B. M. Quednau, G. Roeschert, H. Rossner, A. Peghaire, L. Pienkowski, R. M.Siemssen, C. Stephan, Phys. Rev. C 57 (1998) 2375

[28] S. Katcoff, Phys. Rev. 114 (1959) 905

[29] A. Letourneau et al., Nucl. Phys. A 712 (2002) 133-166

[30] E. Baker, G. Friedlander and J. Hudis, Phys. Rev. 112 (1958) 1319

[31] J. Hudis, Phys. Rev. 171 (1968) 1301

[32] G. D. Westfall, R. G. Sextro, A. M. Poskanzer, A. M. Zebelman, G. W. Butler, E. K. Hyde, Phys. Rev. C 17 (1978) 1368

[33] V. A. Karnaukhov, H. Oeschler, S. P. Avdeyev, E. V. Duginova, V. K. Rodionov, A. Budzanowski, W. Karcz, O. V. Bochkarev, E. A. Kuzmin, L. V. Chulkov, E. Norbeck, A. S. Botvina, arXiv:nucl-ex/0302006 v1 7 Feb 2003

[34] V. A. Karnaukhov et al., Phys. Rev. C 67 (2003) 011601(R)

[35] M. Kleine Berkenbusch, W. Bauer, K. Dillman, S. Pratt, L. Beaulieu, K. Kwiatkowski, T. Lefort, W.-C. Hsi, V. E. Viola, S. J. Yennello, R. G. Korteling, H. Breuer, Phys. Rev. Lett. 88 (2001) 022701

[36] L. Y. Geer, J. Klarmann, B. S. Nilsen, C. J. Waddington, W. R. Binns, J. R. Cummings and T. L. Garrard, Phys. Rev. C 52 (1995) 334

[37] Y. W. Yu and N. T. Porile, Phys. Rev. C 12 (1975) 938

[38] Y. Asano, H. Kariya, S. Mori, M. Okano, M. Sakano, Journ. of the Phys. Soc. of Japan 57 (1988) 2995-3002

[39] J. Hudis, T. Kirsten, R. W. Stoenner, O. A. Schaeffer, Phys. Rev. C 1 (1970) 2019

[40] G. Huentrup, T. Streibel, and W. Heinrich, Phys. Rev. C 63 (2002) 014605

[41] S. B. Kaufman, E. P. Steinberg, M. W. Weisfield, Phys. Rev. C 18 (1978) 1351

[42] M. Debeauvais, J. Tripier, S. Jokic, Z. Todorovic, R. Antansijevic, Phys. Rev. C 23 (1981) 1624

[43] A. D. Panagiotou et al., Phys. Rev. Lett. 52 (1984) 496

[44] R. W. Minich et al., Phys. Lett. 118 B (1982) 458

[45] A. I. Warwick, H. H. Wieman, H. H. Gutbrod, M. R. Maier, J. Peter, H. G. Ritter, H. Stelzer, F. Weik, M. Freedman, D. J. Henderson, S. B. Kaufman, E. P. Steinberg, B. D. Wilkins, Phys. Rev. C 27 (1983) 1083

[46] R. J. Charity et al., Nucl. Phys. A 483 (1988) 371

[47] S. Furihata, Nucl. Inst. Meth. in Phys. Res. B 171 (2000) 251

[48] D. H. E. Gross and K. Sneppen, Nucl. Phys. A 567 (1994) 317

[49] J. P. Bondorf et al., Nucl. Phys. A 387 (1982) 25c

[50] M. E. Fisher, Physics 3 (1967) 255 ; Rep. Prog. Phys. 30 (1967) 615

[51] R. Serber ”Nuclear Reactions at High Energies”, Phys. Rev. 72 (1947) 1113

[52] M. Goldberger, Phys. Rev. 74 (1948) 1269

[53] N. Metropolis, R. Bibins, M. Storm, Phys. Rev. 110 (1958) 185

[54] M. P. Guthrie, R. G. Alsmiller and H. W. Bertini, Nucl. Instr. Meth. 66 (1968) 29

[55] J. Cugnon, Nucl. Phys. A 462 (1987) 751

[56] J. Cugnon, C. Volant and S. Vuillier, Nucl. Phys. A 620 (1997) 475

[57] G.T. Bertsch and S. Das Gupta, Phys. Reports 160 (1988) 189

[58] E. Kozik, private information

[59] J. Aichelin et al., Phys. Rev. C 37 (1988) 2451

[60] V. F. Weisskopf et al., Phys. Rev. 52 (1937) 295

[61] V. F. Weisskopf and D. H. Ewing, Phys. Rev. 57 (1940) 472

[62] I. Dostrovsky et al., Phys. Rev. 116 (1959) 683

[63] T. Matsuse, A. Arima, S.M. Lee, Phys. Rev. C 26 (1982) 2338

[64] A. D. Panagiotou et al., Phys. Rev. C 31 (1985) 55

[65] A. S. Hirsch et al., Phys. Rev. C 29 (1984) 508

[66] E. K. Hyde et al., Phys. Rev. C 4 (1971) 1759

[67] J. A. Gaidos et al., Phys. Rev. Lett. 42 (1979) 82

[68] D. J. Fields et al., Phys. Rev. C 34 (1986) 536

[69] R. Maier et al., "Status of COSY", Fourth European Particle Conference EPAC94, London,England, 1994 ,p. 165 and "Commisioning of the Cooler Synchrotron COSY", Proc. of the 14th Int. Cyclotrons and Their Applications, Cape Town, South Africa,1995, p.338.

[70] R. Maier et al., Nucl. Phys. A 626 (1997) 395c

[71] R. Maier, Nucl. Inst. Meth. in Phys. Res. A 390 (1997) 1

[72] R. Barna et al., Nucl. Inst. Meth. in Phys. Res. A 519 (2004) 610

[73] SPAR, A Fortran program for computing stopping powers and ranges for muons, charged pions, protons and heavy ions. ORNL-4869 (May 1973)

[74] J. F. Ziegler, Rev. Appl. Phys. 85 (1999) 1249

[75] J. Bisplinghoff, F. Hinterberger, AIP Conf. Proc. 221 (1991) 312

[76] D. Hilscher et al., Nucl. Inst. Meth. in Phys. Res. A 414 (1998) 100

[77] A. Coche and G. Bertolini, Semiconductor Detectors (1968), North-Holland Publishing Company - Amsterdam

[78] F. J. Walter et al., Proc. Conf. Nuclear electronics Belgrade vol.1 (1962) 391

[79] R. N. Williams et al., Nucl. Inst. Meth. in Phys. Res. 120 (1974) 261

[80] Ch. Schiessl et al., Nucl. Inst. Meth. in Phys. Res. 192 (1982) 291

[81] C. R. Gruhn et al., Nucl. Inst. Meth. in Phys. Res. 196 (1982) 33

[82] A. Bubak, PhD Thesis, Katowice University (2004).

[83] ROOT Software: http:\\ root.cern.ch

[84] private communication Z. Rudy and A. Kowalczyk

[85] A. S. Goldhaber, Phys. Lett. 53 B (1974) 306

[86] C. K. Gelbke et al., Phys. Lett. 70 B (1977) 415

[87] L. G. Moretto and G. J. Wozniak, Annual Review of Nuclear and Particle Science 43 (1993) 379

[88] V. V. Avdeichikov et al., Sov. J. Nucl. Phys. 48 (1988) 1043

[89] W. Trautmann et al., Z. Phys. A 344 (1993) 447

[90] S. P. Avdeyev, et al., Eur. Phys. J. A 3 (1998) 75

[91] D. H. Boal, Adv. Nucl. Phys. 15 (1985) 85

[92] J. Huefner, Phys. Rep. 125 (1985) 129

[93] R. E. L. Green et al., Phys. Rev. C 29 (1984) 1806

[94] R. E. L. Green et al., Phys. Rev. C 35 (1987) 1341

[95] R. G. Korteling et al., Phys. Rev. C 7 (1973) 1611

[96] D. B. Barlow et al., Phys. Rev. C 45 (1992) 293

[97] M. Mahi et al., Phys. Rev. Lett. 60 (1988) 1937

[98] N. T. Porile et al., Phys. Rev. C 39 (1989) 1914

[99] A. Letourneau, PhD thesis GANIL T 00 06, Universit*é* de Caen (2000)

[100] H. A. Bethe, Ann. Phys. 5 (1930) 325

[101] D. E. Groom et al., The European Physical Journal C 15 (2000) 1

[102] C. Caso et al., Eur. J. Phys. C 3 (1998) 1

[103] J. Lindhard and M. Scharff, Phys. Rev. 124 (1961) 128

[104] S. B. Kaufman, Nucl. Inst. Meth. in Phys. Res. 115 (1974) 47

[105] H.-O. Neidel and H. Henschel, Nucl. Inst. Meth. in Phys. Res. 178 (1980) 137

[106] F. S. Coulding et al., Nucl. Inst. Meth. in Phys. Res. 162 (1979) 609-622

[107] H. Kobayashi, A. Nakamoto and M. Hosoe, Nucl. Inst. Meth. in Phys. Res. 34 (1985) 222

Versicherung

Ich versichere, daβ ich die Arbeit selbst*ä*ndig verfaβt habe und alle genutzen Quellen und Hilfsmittel angegeben sowie Zitate kenntlich gemacht habe. Ich bin damit einverstanden, daβ die Arbeit im Bereich des Fachgebiets Naturwissenchaften-Physik und der Bergischen Unviversit*ä*t Wuppertal benutzt wird und auβerhalb des Hochschulbereichs durch Dritte eingesehen und unter Verwendung urheberrechtlicher Grunds*ä*tze zitiert werden darf.